OPTIMAL SIZING AND CONTROL OF SUPERCAPACITORS FOR COST-EFFECTIVE HYBRIDIZATION OF BATTERY-ALONE ENERGY STORAGE SYSTEMS

by

Mukalu Sandro Masaki

Submitted in partial fulfillment of the requirements for the degree
Philosophiae Doctor (Electrical Engineering)

in the

Department of Electrical, Electronic and Computer Engineering
Faculty of Engineering, Built Environment and Information Technology

UNIVERSITY OF PRETORIA

December 2022

SUMMARY

OPTIMAL SIZING AND CONTROL OF SUPERCAPACITORS FOR COST-EFFECTIVE HYBRIDIZATION OF BATTERY-ALONE ENERGY STORAGE SYSTEMS

by

Mukalu Sandro Masaki

Promoter:	Prof. Xiaohua Xia
Co-promotor:	Prof. Lijun Zhang
Department:	Electrical, Electronic and Computer Engineering
University:	University of Pretoria
Degree:	Philosophiae Doctor (Electrical Engineering)
Keywords:	Battery, Supercapacitor, Hybrid Energy Storage System, Retrofit, Hybridization, Sizing, Life cycle cost, Optimal control, Optimization, Fuzzy logic, Receding horizon control.

With growing effects of global warming, batteries have a crucial role to play in supporting global effort to reach carbon neutrality. However, batteries remain prone to early failure. Operational causes of premature deterioration are high current intensity, abrupt current fluctuations, repetitive charge-discharge cycles, deep discharge, and thermal stress. An effective way to mitigate stress sustained by the battery, and therefore increase its service life, is association of batteries and supercapacitors (SC) into battery-SC hybrid energy storage systems (HESS). Despite considerable interest enjoyed among the research community, the adoption of battery-SC HESS is still marginal in practice due to the relatively high cost of SC. As a result, most batteries are still implemented as stand-alone energy storage systems, or battery-alone energy storage systems (BESS).

Given the continuous advancement in the manufacturing economics of SC, in one hand, and the market domination of BESS, in the other hand, close attention should be paid to the upgrade of BESS into battery-SC HESS. The study of contemporary literature shows that such a conversion has been scarcely investigated before. Most control strategies reported in the past were also found unsuitable for retrofit

applications, due to significant modifications required on the existing control infrastructures. In view of technical, economic, and environmental implications of such modifications, this may raise concerns for stakeholders.

Regarding sizing of battery-SC HESS, it was found that previous investigations focusing on their control used arbitrary SC size to test the performances of controllers. On the other hand, studies interested in the economic sizing of this HESS usually failed to fully assess the costs and benefits over the entire lifespan of the energy system. Moreover, other shortcomings such as a fixed service life for each ES equipment regardless of the operating conditions, overlooking of certain cost components and economic parameters (inflation and escalation rate of electricity price) were also found in some studies. This usually results in misleading assessments of costs and benefits associated with battery-SC HESS.

In an attempt to address the above gaps in the current literature, this thesis presents two control strategies aimed at achieving trouble-free retrofit of BESS with SC, a preliminary investigation on the impact of spatial arrangement on the thermal stress sustained by the battery and SC cells, and finally an SC sizing model for cost-effective hybridization of BESS.

Primarily designed for hybrid renewable systems (HRS) originally equipped with BESS and controlled by a receding horizon control (RHC), the first control scheme consists of a hierarchical RHC of the SC-retrofitted HRS. Depending on the characteristics of the power management unit (PMU) running the previous RHC scheme, no or little modifications are required to integrate the SC into the existing infrastructure. Besides the reduction in electrical stress sustained by the battery, the proposed control framework also increases the amount of energy supplied by intermittent renewable resources and the power stability at the point of common coupling (PCC).

The second control model is built around a fuzzy logic controller unit to assist in retrofitting any BESS with SC. Thermoelectric management of batteries is realized through sharing of low-frequency current components between the two ES devices, besides the SC's full supply of high-frequency current components. Improvement in battery service life is demonstrated. Compared to the previous controller, specially designed for retrofitting of BESS-equipped power plants controlled by RHC, this thermoelectric controller is intended for implementation on any existing BESS.

The preliminary study conducted on the influence of spatial arrangement of battery-SC HEES cells on the thermal management of batteries demonstrates that the proximity between a battery cell and an SC cell can effectively contribute to the cooling process of batteries, thanks to thermal interaction between them. Accordingly, adequate arrangement of ES cells can offer a passive assistance to the above controller in achieving thermoelectric management of batteries.

Finally, the thesis introduces a life cycle cost (LCC)-based optimization model that assists in properly sizing SC intended for retrofit in existing BESS. The possibility offered to stakeholders to take informed decisions about the economic opportunity of such an upgrade is also demonstrated.

DEDICATION

To

I AM, a.k.a. YHWH;

For the opportunity to experience His love, faithfulness, and mercy in a special way throughout my postgraduate studies (Deut. 29:5) ;

My wife, Gray-Doriane;

For her sacrifices, encouragement, and support during this journey.

ACKNOWLEDGEMENT

This research work has been conducted with the National Hub for Energy Efficiency and Demand Side Management (EEDSM), hosted in the Department of Electrical, Electronic and Computer Engineering, University of Pretoria. The financial and material support provided by the University of Pretoria and the National Hub for EEDSM are gratefully acknowledged.

I would like to express my heartfelt gratitude and appreciation to my promoter, Professor Xiaohua Xia, for initiating this study and for his trust and support. Having indelibly impacted my personal life and career, I just want to say “Thank you so much, prof”.

I am grateful to my co-promoter, Professor Lijun Zhang, for his guidance, help and availability have been of an inestimable value throughout the conducting of this research work.

I am indebted to my entire family who unfailingly help me climb the steps towards my fulfilment. In particular, to my parents, Professor Simon-Blaise Masaki Ngungu and Mrs Anne-Marie Tundu Makulongo, for your prayers, encouragement, and continual assistance. I express my gratitude to the Mudibus for their substantial support throughout my postgraduate studies. Many thanks to Herve , Gaelle, Regina, and Gloire Masaki for your precious assistance.

Last, but not least, I would like to show appreciation to my “small tribe.” My wife, Gray-Doriane, for being there for me at all times. To my kids, Oxana-Xenia, Alexia-Samantha, and Jayne-Simon, for putting a smile on my face every day.

LIST OF ABBREVIATIONS

AC	Alternative current
BESS	Battery-alone energy storage system
CAPEX	Capital expenditure
CB	Circuit breaker
DC	Direct current
ECM	Equivalent circuit model
EER	Energy efficiency ratio
EMS	Energy management system
EoL	End-of-life
ES	Energy storage
ESR	Equivalent series resistance
FIS	Fuzzy inference system
GA	Genetic algorithm
HESS	Hybrid energy storage system
HRS	Hybrid renewable system
HVAC	Heating ventilation and air conditioning
LCC	Life cycle cost
LPF	Low-pass Filter
MF	Membership function
MPC	Model predictive control
MPM	Model-plant mismatch
NLP	Nonlinear programming
NPV	Net present value
O&M	Operation and maintenance
p.u.	Per unit
PCC	Point of common coupling
PCM	Phase change material
PI	Proportional-integral
PMU	Power management unit
PV	Photovoltaic
PWM	Pulse width modulation

RHC	Receding horizon control
RMS	Root-mean-square
ROL	Rule output level
S.I.	International system
SC	Supercapacitor
SNR	Signal-to-noise ratio
SoC	State-of-charge
SS	State-space
SV	Salvage value
UDDS	Urban dynamometer driving cycle

LIST OF SYMBOLS

α	Constant coefficient for battery acceleration ageing
$\beta(k)$	Altitude angle (°)
ΔT	Sampling time (s)
η_1	Efficiency of the PV's DC-DC converter (%)
η_2	Battery's DC-DC converter efficiency (%)
η_3	Supercapacitor's DC-DC converter efficiency (%)
η_4	Efficiency of AC-DC inverter (%)
$\eta_{b,c}$	Battery charging efficiency (%)
$\eta_{b,d}$	Battery discharging efficiency (%)
$\eta_{sc,c}$	Supercapacitor charging efficiency (%)
$\eta_{sc,d}$	Supercapacitor discharging efficiency (%)
η_{pv}	PV conversion efficiency (%)
$\theta(k)$	Incident angle (°)
π	Average inflation rate (%)
ρ	Ground reflectance
τ	Time constant (sec.)
θ	Room temperature (K)
θ_{ref}	Reference room temperature (K)
$\phi_C(k)$	Azimuth angle of PV panels (°C)
$\phi_S(k)$	Solar azimuth angle (°C)
ψ	Tilt angle of PV panels (°C)
$\mathbf{A}_b$	State matrix of the battery SS model
A_c	Active area of panel (m^2)
A_h	Ampere-hour throughput (Ah)
$\mathbf{A}_{sc}$	State matrix of the SC SS model
b	Lower layer variables (subscript)
$\mathbf{B}_b$	Input matrix of the battery SS model
B_{cal}	Pre-exponential factor for battery calendar ageing ($Ah^{1-z_{cal}}$)
B_{cyc}	Pre-exponential factor for battery cycle ageing ($Ah^{1-z_{cyc}}$)
$\mathbf{B}_{sc}$	Input matrix of the SC SS model

C	Sky diffuse coefficient
C_1	Total battery transient capacitance (F)
$C_{1,u}$	Battery's transient capacitance per cell (F)
$\mathbf{C}_b$	Output matrix of the battery SS model
C_{bat}	Battery thermal capacity (J/°C)
C_{bulk}	Total battery's bulk inner part capacitance (F)
$C_{bulk,u}$	Battery's bulk inner part capacitance per cell (F)
C_f	Total SC's fast capacitance (F)
$C_{f,u}$	SC's fast capacitance per cell (F)
C_{fl}	Filter capacitance (F)
C_i	Internal thermal capacitance (J/K)
C_m	Total SC's medium capacitance (F)
$C_{m,u}$	SC's medium capacitance per cell (F)
C_{rate}	Battery's Charge/discharge rate
C_s	Total SC's slow capacitance (F)
$\mathbf{C}_{sc}$	Output matrix of the SC SS model
$C_{s,u}$	SC's slow capacitance per cell (F)
C_{sc}	Supercapacitor's capacitance (F)
C_{sh}	Shell thermal capacitance (J/K)
C_{surf}	Total battery's surface capacitance (F)
$C_{surf,u}$	Battery's surface capacitance per cell (F)
C_y	Number of operating cycles per day
CC_b	NPV of battery replacement cost (USD)
CC_{c2}	NPV of SC's DC-DC converter cost (USD)
CC_{sc}	NPV of SC replacement cost (USD)
d	Discount rate (%)
$\mathbf{D}_b$	Feedforward matrix of the battery SS model
$\mathbf{D}_{sc}$	Feedforward matrix of the SC SS model
e_0	Electricity price at year 0 (USD/kWh)
$E_{b,loss}$	Daily battery energy losses (Wh)
$E_{b,N}$	Rated energy of a battery (Wh)
$E_{c1,loss}$	Daily battery's DC-DC converter energy losses (Wh)
$E_{c2,loss}$	Daily SC's DC-DC converter energy losses (Wh)

E_{hvac}	Daily HVAC electricity consumption related to the HESS (Wh/day)
$E_{sc,loss}$	Daily SC energy losses (Wh)
$E_{sc,N}$	Rated energy of a SC cell (Wh)
Ea_{cal}	Activation energy for battery calendar ageing (J/mol)
Ea_{cyc}	Activation energy for battery cycle ageing (J/mol)
F_k	k-th Membership functions
$I_{b,1C}$	1C battery current (A)
$\overline{I_b}$	Maximum battery current (A)
$\underline{I_b}$	Minimum battery current (A)
$I_{b,rms}$	Root-mean-square battery current (A)
$I_{bat,nom}$	Battery nominal current (A)
$I_{BC}(k)$	Bear radiation (W/m^2)
i_{HESS}	Total current of HESS (p.u.)
i_{hf}	HESS' high-frequency current (p.u.)
i_{lf}	HESS' low-frequency current (p.u.)
I_{req}	Load current required from the HESS (A)
I_{sc}	SC current (A)
$i_{sc,lf}$	SC's low-frequency current (p.u.)
$\overline{I_{sc}}$	Maximum SC current (A)
$\underline{I_{sc}}$	Minimum SC current (A)
$I_{sc,req}$	Required SC current (A)
$i_{sc,req}$	Required SC current (p.u.)
I_b	Battery current (A)
$I_B(k)$	Direct-beam radiation (W/m^2)
J	Cost (fitness) function
k	Sample time (s)
k_b	Battery NPV-related exponent
k_{c2}	SC's DC-DC converter NPV-related exponent
k_i	Integral gain
k_p	Proportional gain
k_{sc}	SC NPV-related exponent
L	Low (fuzzy membership)
L	Inductance value (H)

$L_{b,new}$	Lifespan of new batteries (days)
$L_{b,old}$	Lifespan of existing batteries (days)
L_{c2}	Lifespan of SC's converter (days)
L_{fl}	Filter inductance (H)
L_{plant}	Plant's remaining lifespan (days)
L_{sc}	Actual SC's lifespan (days)
$L_{sc,N}$	Rated SC's lifespan (days)
m	Modulation index
M_b	Number of battery remplacement required
m_c	Converter capacity margin (%)
M_{c2}	Number of SC's DC-DC converters required
$MC_{c2,0}$	Converter's yearly maintenance cost at year 0 (USD/W)
$m_{conv,0}$	Converter's unit maintenance cost at year 0 (USD)
M_{sc}	Number of SC sets required
$m_{sc,0}$	SC's unit maintenance cost at year 0 (USD/Wh)
$MC_{sc,0}$	SC's yearly maintenance cost at year 0 (USD/Wh)
n	Day number in the year
N	Number of sample intervals
$N_{b,p}$	Number of battery strings in parallel
$N_{b,s}$	Number of batteries in series per string
N_g	Number of control steps
NH	Negative High (fuzzy membership)
NM	Negative Medium (fuzzy membership)
N_p	Prediction horizon
$N_{sc,p}$	Number of SC string in parallel
$N_{sc,s}$	Number of SCs in series per string
OCV	Battery's open circuit voltage (V)
p	Laplace variable
P_1	Net power injected by the PV solar system (W)
P_2	Battery power (W)
P_2^-	Discharging battery power (W)
P_2^+	Charging battery power (W)
P_3	Supercapacitor power (W)

P_3^-	Discharging supercapacitor power (W)
P_3^+	Charging supercapacitor power (W)
P_4	Power flow between the grid and the hybrid renewable system (W)
P_4^-	Power imported from the utility grid (W)
P_4^+	Power exported to the utility grid (W)
$p_{b,0}$	Battery price at year 0
$\overline{P_{b,ch}}$	Upper bound on battery charging power (W)
$\overline{P_{b,disch}}$	Upper bound on battery discharging power (W)
P_{bat}	Battery heat generation (W)
$P_{c1,N}$	Rated power of battery's converter
$P_{c1,out}$	Output power of battery's converter
$P_{c2,N}$	Rated power of SC's converter
$P_{c2,out}$	Output power of SC's converter
PH	Positive High (fuzzy membership)
P_L	Power demand (W)
PM	Positive Medium (fuzzy membership)
$P_{pv,BC}$	PV output power related to beam radiation (W)
$P_{pv,DC}$	PV output power related to diffused radiation (W)
P_{pv}	Maximum power available to the PV system (W)
$P_{pv,RC}$	PV output power related to reflected radiation (W)
$p_{sc,0}$	SC price at year 0
$\overline{P_{sc,ch}}$	Upper bound on supercapacitor charging power (W)
$\overline{P_{sc,disch}}$	Upper bound on battery discharging power (W)
$\overline{P_{tie}}$	Thermal capacity of electrical conductors between the grid and hybrid renewable system (W)
$Q_{b,EoL}$	Battery's end-of-life capacity (Ah)
$Q_{b,loss}$	Daily capacity loss of batteries (Ah/day)
$Q_{b,loss}^{cal}$	Daily calendar capacity loss of batteries (Ah/day)
$Q_{b,loss}^{cyc}$	Daily cycle capacity loss of batteries (Ah/day)
$Q_{b,N}$	Rated capacity of batteries (Ah)
Q_i	Heat generation by the energy storage (W)
Q_{ib}	Battery heat generation (W)
Q_{is}	Supercapacitor heat generation (W)
r	Annual escalation rate of electricity price (%)

R	Inductor resistance (Ω)
R_0	Battery's ohmic internal resistance (Ω)
R_1	Transient resistance per battery string (Ω)
$R_0{}'$	Combined electro and ohmic internal resistances per battery string (Ω)
$R_{0,u}{}'$	Combined electro and ohmic internal resistances per battery cell (Ω)
$R_{1,u}$	Transient resistance per battery cell (Ω)
R_{b2a}	Thermal resistance battery-air (°C)/W
R_{bat}	Battery Ohmic resistance (Ω)
R_{bs}	Thermal resistance between the battery and supercapacitor shells (K/W)
R_{bulk}	Electrode's bulk resistance per battery string (Ω)
$R_{bulk,u}$	Electrode's bulk resistance per battery cell (Ω)
R_{c-s}	Thermal resistance between the energy storage's core and shell (K/W)
R_f	Fast resistance per SC string (Ω)
$R_{f,u}$	Fast resistance per SC cell (Ω)
R_{fl}	Filter resistance
R_g	Ideal gas constant (J/(mol·K))
R_i	Battery's series resistance (Ω)
R_{lk}	Leakage resistance per SC string (Ω)
$R_{lk,u}$	Leakage resistance per SC cell (Ω)
R_m	Medium resistance per SC string (Ω)
$R_{m,u}$	Medium resistance per SC cell (Ω)
$R_{s,u}$	Slow resistance per SC cell (Ω)
R_{s-a}	Thermal resistance between the energy storage's shell and the ambience (K/W)
R_s	Slow resistance per SC string (Ω)
R_{ser}	Supercapacitor's series resistance (Ω)
R_x	Equivalent resistance of R_f,R_m,R_s,and R_{lk} in parallel (Ω)
SoC	State-of-charge (%)
SoC_b	Battery state-of-charge (%)
$\overline{SoC_b}$	Upper bound of battery state-of-charge (%)
$\underline{SoC_b}$	Lower bound of battery state-of-charge (%)
SoC_{ref}	Reference SC's SoC
SoC_{sc}	Supercapacitor state-of-charge (%)
$\overline{SoC_{sc}}$	Upper bound of supercapacitor state-of-charge (%)

$\underline{SoC_{sc}}$	Lower bound of superpacitor state-of-charge (%)
t	Time (s)
t	Upper layer variables (subscript)
T	Time constant of low-pass filter (s)
T_a	Ambient temperature (°C)
T_{bat}	Battery shell temperature (°C)
T_i	Energy storage's internal temperature (°C)
T_{max}	Maximum battery temperature (°C)
T_{ref}	Reference battery temperature (°C)
T_s	Sampling time (s)
T_{sh}	Energy storage's shell temperature (°C)
$\mathbf{u}_b$	Battery's input vector
U_c	Supercapacitor capacitance voltage (V)
$\mathbf{u}_{sc}$	SC's input vector
V_1	Voltage across battery's $R_1 - C_1$ component (V)
V_b	Battery terminal voltage (V)
$\overline{V_b}$	Maximum battery voltage (V)
$\underline{V_b}$	Minimum battery voltage (V)
V_{bulk}	Voltage across battery's bulk capacitance (F)
V_{cc}	Battery's open circuit voltage (V)
V_f	Voltage across SC's fast capacitance (F)
v_k	Weighting coefficients
V_L	Inductor voltage (V)
$V_{L,ref}$	Reference inductor voltage (V)
V_m	Voltage across SC's medium capacitance (F)
V_s	Voltage across SC's slow capacitance (F)
V_{sc}	SC terminal voltage (V)
$\overline{V_{sc}}$	Maximum SC voltage (V)
$\underline{V_{sc}}$	Minimum SC voltage (V)
V_{surf}	Voltage across battery's surface capacitance (F)
w_k	k-th rule firing strength
X	Array of optimized parameters
$\mathbf{x}_b$	Battery's state vector

x_k	k-th parameters optimized by GA
$\mathbf{x}_{sc}$	SC's state vector
$\mathbf{y}_b$	Battery's output vector
$\mathbf{y}_{sc}$	SC's output vector
z_{cal}	Exponential constant for battery calendar ageing
z_{cyc}	Exponential constant for battery cycle ageing
z_k	k-th rule output levels

TABLE OF CONTENTS

LIST OF FIGURES

LIST OF TABLES

CHAPTER 1 INTRODUCTION

1.1 PROBLEM STATEMENT

1.1.1 Context of the problem

Now more than ever, global warming represents the biggest threat facing mankind. Access to sustainable energy remains a key challenge in most developing countries. In this context, energy storage (ES) technologies are expected to play a central role in pursuing the global objective to reach carbon neutrality the soonest. Estimated around 550 GWh in 2018, the global stationary and transportation ES market is projected to exceed 2500 GWh by 2030, a nearly fivefold increase [1].

Due to their high energy density, flexibility and modularity [2, 3, 4], batteries are currently among the leading ES technologies worldwide. These characteristics resulted in a competitive advantage in various sectors, especially in transportation [5], off-grid and grid-connected renewable systems [6, 7], and utility-scale energy storage for ancillary services [8]. For example, the contribution by technology (pumped hydro excluded) in the 9 786 GW of grid-scale ES capacity installed worldwide is depicted in Figure 1.1. However, despite this relative success, batteries remain prone to early failure. Designed for a service life between 10 and 15 years [9], the operational causes of premature deterioration are high current intensity, abrupt current fluctuations, repetitive charge-discharge transition, deep discharge, and thermal stress [10, 11]. The relatively low current density of batteries is the key explaining factor of the current-related causes of failure.

One of the effective means to address this condition consists, therefore, combining the battery with at least one different ES technology with characteristics that complement those of the battery. Various

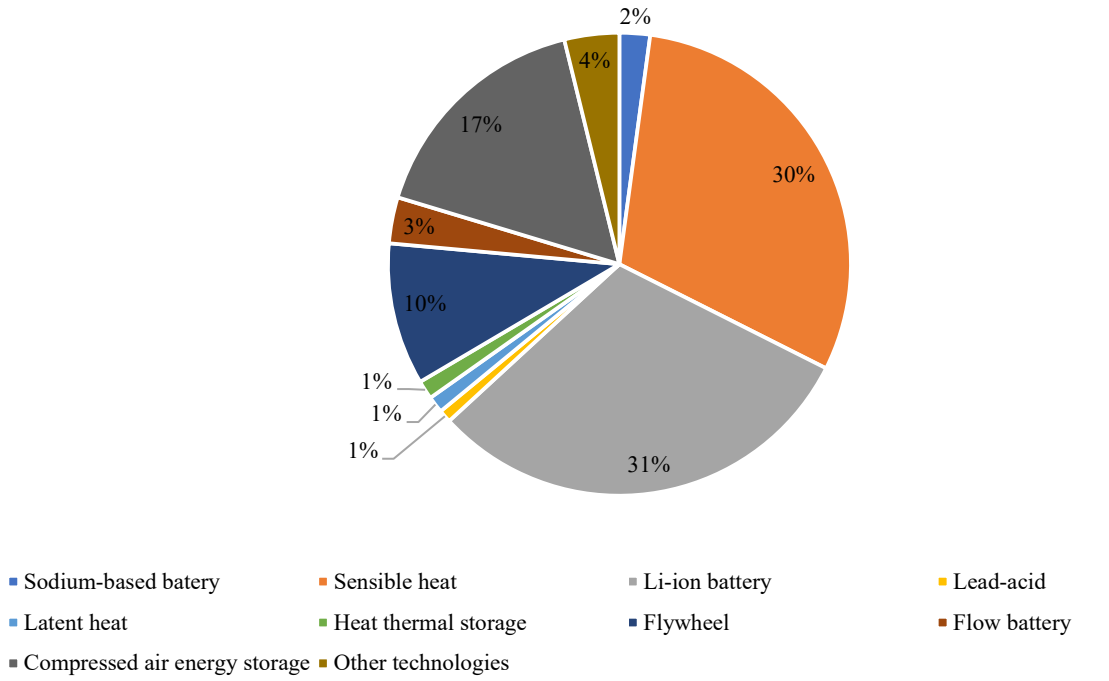

Figure 1.1. Share of various technologies within the global grid-scale energy storage infrastructure in 2021 [12] (No permission required)

battery-based hybrid energy storage systems (HESS) architectures have been envisaged in the past, including [13, 14]:

- Battery-Battery HESS
- Battery-Compressed Air Energy Storage (CAES) HESS
- Fuel Cell-Battery HESS
- Fuel Cell-Battery-Supercapacitor (SC) HESS
- Battery-Superconducting Magnetic Energy Storage (SMES) HESS
- Battery-Flywheel HESS
- Battery-SC HESS

Figure 1.2 presents a Ragone chart of the main types of batteries and other ES technologies likely to be paired with a battery into battery-based HESS. Combining a relatively high power density and low energy density, the SC shows to be highly complementary to batteries. Figure 1.3 provides further evidence about the complementarity between the SC and a few types of batteries. This includes technical, economical, safety and environmental criteria. On the technical side, given the typical

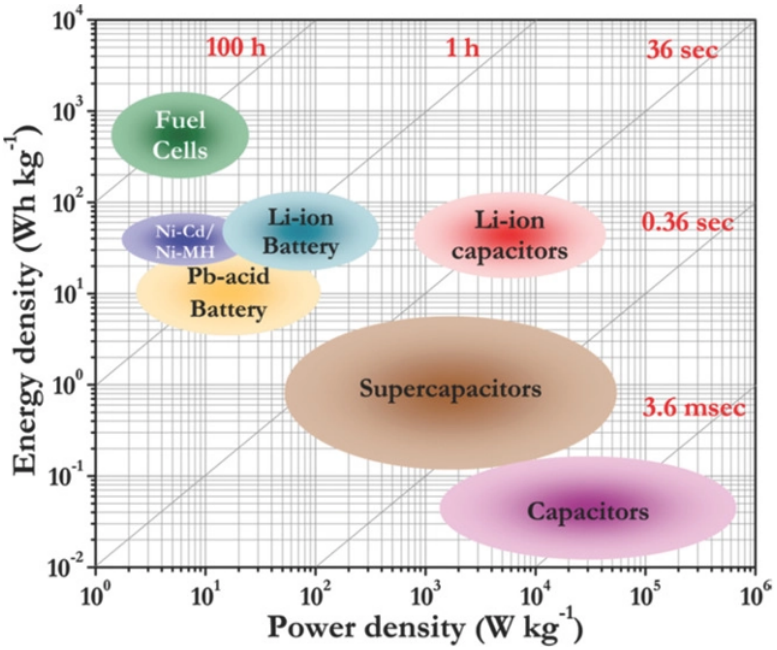

Figure 1.2. Ragone Plot of various batteries and other ES (Taken from [15] with permission.)

response time of batteries, of the order of one second, and that of SC, of the order of 0.016 second [16], pairing them in hybrids arrays offers also the possibility of delivering better dynamic responses in comparison to BESS alone.

In the past, significant research has been dedicated to achieving effective power allocation within battery-SC HESS. Various power management strategies have been developed to ensure that the high-frequency current components are directed towards the SC while the rest is supplied by the battery [18, 19, 20, 21, 22, 23]. While good performances are generally observed, it has been found that previous studies failed to accommodate the particular case of battery-alone energy storage systems (BESS). Indeed, although battery-SC HESS has enjoyed considerable interest among the research community, the adoption of this architecture is still marginal in practice. According to the International Energy Agency (IEA), the SC contributed 4% to the global deployment of ES in 2014. This contribution has now shrunk to less than 1% [24, 25]. The trend suggests that SC has difficulty penetrating the competitive ES market, mainly due to its relatively high price. The report also suggests that, so far, batteries are predominantly implemented as BESS [26]. To anticipate significant improvement in the economics of SC manufacturing, which will trigger the appetite of project funders and practitioners, researchers should prioritize the development of battery-SC HESS controllers with features for straightforward hybridization of BESS. This will help accelerate the adoption of battery-SC HESS by enabling the

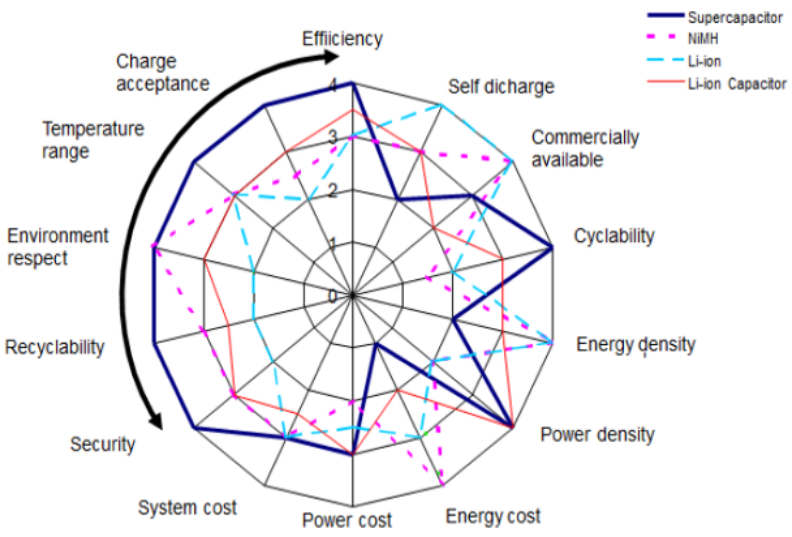

Figure 1.3. Comparison between characteristics of batteries and SC [17] (No permission required)

retrofit of many existing BESS with SC.

Besides the above-mentioned control concern, it has also been noted that previous studies have paid little attention to the sizing of SC. An arbitrary choice often results in oversized SC, further exacerbating the pace of battery-SC HESS implementation in practice. Apart from not being suitable for the case of retrofit projects, the earlier investigations about the cost-effective sizing of ES equipment in battery-SC HESS [27, 28, 29, 30, 31] usually suffer from one or many shortcomings. This includes focusing solely on the initial capital cost, overlooking certain cost components related to the operation and maintenance (O&M) of ES components, overlooking the variations of prices over time, and assuming fixed lifespans for the ES components regardless of the operating conditions. These models, therefore, inexorably result in suboptimal designs of battery-SC HESS.

1.1.2 Research gap

Considering the above, the research gap can be summarized as follows:

1) The lack of control strategies aimed at upgrading BESS into battery-SC HESS without requiring modifications to the existing control infrastructure.
2) The possibility of enhancing the technical performances of grid-tied intermittent renewable power plants through the retrofit of their BESS with SC has not been explored in previous

studies.

3) No comprehensive model aimed at supporting the thermoelectric management of batteries through adequate control of SC has been found in the literature.
4) The lack of a techno-economic model that informs on the opportunity to upgrade a BESS into battery-SC HESS.

1.2 RESEARCH OBJECTIVE AND QUESTIONS

With the above in mind, the prime objective of this research work is to investigate the possibility of retrofitting BESS into battery-SC HESS. To this end, at the operational level, this research seeks to develop controllers that deliver acceptable post-retrofit performances while requiring little or no modifications to the existing infrastructure. At the design level, this study investigates a life cycle cost (LCC) model that can be used to optimally size the SC so that the total cost incurred by the HESS during the rest of the power plant's lifespan is minimal. This model could also determine the LCC of the existing BESS to ensure sound decision-making in connection with the economic implications of upgrading an existing BESS into a cost-effective battery-SC HESS.

The research questions are therefore formulated as follows:

1) Can the BESS be upgraded to battery-SC HESS with little or no changes to the control infrastructure and without affecting the proper functioning of existing power systems?
2) How can such a retrofit positively impact the technical performance of a grid-tied renewable energy system equipped with intermittent sources and a BESS?
3) How can the SC be controlled to assist the thermoelectric management of batteries?
4) Can the SC and its converter be optimally sized to minimize the LCC of the resulting battery-SC HESS?
5) How can such a sizing approach be beneficial for decision-making on whether to upgrade a BESS to a battery-SC HESS?

1.3 APPROACH

To achieve the objectives introduced earlier, this research has been articulated around the approach described below.

1) Literature study – Previous research relevant to the control and sizing of battery-SC HESS has been reviewed.
2) Identification of the energy systems – Throughout the study, suitable energy systems have been considered to answer specific research questions.
3) System modelling – Given an energy system, appropriate models have been formulated for all its components.
4) Design of the controllers and SC sizing model – Control strategies and an SC sizing model intended to answer the above research questions have been formulated.
5) Laboratory experiment – In the particular case of the battery, a test-bed has been also set up to validate an equivalent circuit model (ECM) variant developed during this study.
6) Implementation of the simulation models – To test the effectiveness of the proposed controllers and SC sizing model, simulation models have been implemented in appropriate environment.
7) Simulation and analysis – Practical case studies have been set up and simulated in the above environment. The results obtained have been extensively analysed thereafter.
8) Discussion – Finally, the simulation results have been thoroughly discussed in line with the research objectives and questions identified earlier.

1.4 RESEARCH GOALS

In light of the above, the study reported in this thesis pursues the following goals:

1) To assess the suitability of existing battery-SC HESS energy management systems (EMS) for controlling BESS retrofitted with SC.
2) To ascertain the capability of existing models for SC sizing aimed at a cost-effective upgrade from BESS to battery-SC HESS.

3) To develop an SC controller that enhances the technical performances of grid-tied intermittent renewable power plants by upgrading the BESS with minimum or no changes required on the control infrastructure.
4) To develop an SC controller for modification-free retrofit of BESS to assist in thermoelectric management of batteries.
5) To come up with a sizing model for SC to achieve a cost-effective upgrade from BESS to battery-SC HESS.

Secondarily, the following goals are also pursued:

1) To propose an ECM battery model with better accuracy than the typical ECM models without excessive increase in computational load.
2) To study the relationship between the thermal stresses sustained by the battery and the physical arrangement of the cells in a battery-SC HESS.

1.5 RESEARCH CONTRIBUTION

In this thesis, the following contributions have been made:

1) A receding horizon control (RHC) framework is developed to retrofit SC to an existing BESS within a grid-tied renewable power system. Little or no modifications are required on the control infrastructure, depending on the capacity of the controller installed on site.
2) A fuzzy logic control (FLC) system is introduced to achieve thermoelectric management of batteries after upgrading to a battery-SC HESS. No modification is needed on the existing infrastructure. As a particularity, the controller is designed to slow down the overheating and overcooling of batteries when operated under extreme temperatures.
3) The influence on the battery temperature of the spatial arrangement of battery and SC cells within a HESS is investigated. A comparison is also made with the BESS scenario.
4) A comprehensive LCC model is proposed for the optimal sizing of SC in the context of an upgrade from BESS to battery-SC HESS.

5) Secondarily, a new variant of the equivalent circuit model (ECM) is introduced. This model is slightly more accurate than the conventional ECMs without an excessive increase in computation burden.

1.6 RESEARCH OUTPUTS

The following publications have resulted from the study reported in this thesis:

1) M. S. Masaki, L. Zhang, X. Xia, "A hierarchical predictive control for supercapacitor-retrofitted grid-connected hybrid renewable systems," *Applied Energy*, Vol. 242, 2019, pp. 393-402.
2) N. K. Antoinette, M. S. Masaki, F. Barzegar, X. Xia, "Thermal management of hybrid energy storage systems based on spatial arrangement," *Applied Energy Symposium 2019: Low carbon cities and urban energy systems*, 16-18 October, 2019, Xiamen, China. (Unpublished)
3) M. S. Masaki, L. Zhang, X. Xia, "Fuzzy logic control of plug-in supercapacitor storage for thermoelectric management of batteries," *Renewable Energy Focus*, Vol. 43, 2022, pp. 59-73.
4) M. S. Masaki, L. Zhang, X. Xia, "Optimal sizing of supercapacitors for cost-effective hybridization of battery-alone energy storage systems," *Applied Energy* (submitted).

1.7 OVERVIEW OF STUDY

This thesis is laid out as follows:

1) This chapter (Chapter 1) forms the introductory chapter of this thesis. The research background and motivation of this study, research contributions, and research outputs are given here.
2) Chapter 2 introduces the review of literature focusing on the control of battery-SC HES. Previous studies on the sizing of this category of HESS are also reported here. The relevance of these control and sizing models with respect to the retrofit of BESS with SC is also discussed in the same chapter.
3) The hierarchical RHC for supercapacitor-retrofitted grid-tied hybrid renewable systems is developed and discussed in Chapter 3.

4) The FLC proposed for thermoelectric management of batteries using power-sharing with SC is presented and discussed in Chapter 4.

5) Preliminary findings on the relationship between the thermal stress sustained by the battery temperature and the spatial arrangement of cells within a battery-SC HESS are presented in Chapter 5.

6) The LCC-based optimization model aimed to deliver a cost-effective sizing of SC for the hybridization of BESS is studied and discussed in Chapter 6.

7) The key findings of these studies and the perspective for future research are provided in Chapter 7.

CHAPTER 2 LITERATURE STUDY

2.1 CHAPTER OVERVIEW

This chapter presents the literature review for this thesis. Section 2.2 introduces the various topologies of battery-SC HESS. A discussion about their respective suitability with respect to the upgrade of BESS is also conducted. Various strategies have been previously used for effective power allocation within battery-SC HESS. These models are reviewed in Section 2.3. More than SC batteries are very sensitive to temperature variations, which affect their performance and lifespan. Earlier research on using SC to perform thermal or thermoelectric management of batteries is presented in Section 2.4. Concluding remarks are formulated in Section 2.6.

2.2 TOPOLOGIES OF BATTERY-SUPERCAPACITOR HYBRID ENERGY STORAGE SYSTEMS

In order to form HESS using battery cells/modules and SC cells/modules, various configurations can be envisaged, as shown in Figure 2.1. The passive configuration illustrated in Figure 2.1(a) consists of connecting the two ES technologies directly in parallel, and no converter is used to interface the HESS and the DC bus. While cheap and easy to implement, this architecture lacks control over the ES component. By forcing the voltages of ES components to be equal at all times, the HESS will inevitably deliver suboptimal performances.

The semi-active architectures depicted in Figs. 2.1(b) and (c) are obtained by intercalating a DC-DC converter between the ES devices. By controlling one of the two ES devices, the semi-active architectures can deliver better performances than the passive counterpart without reaching the level of

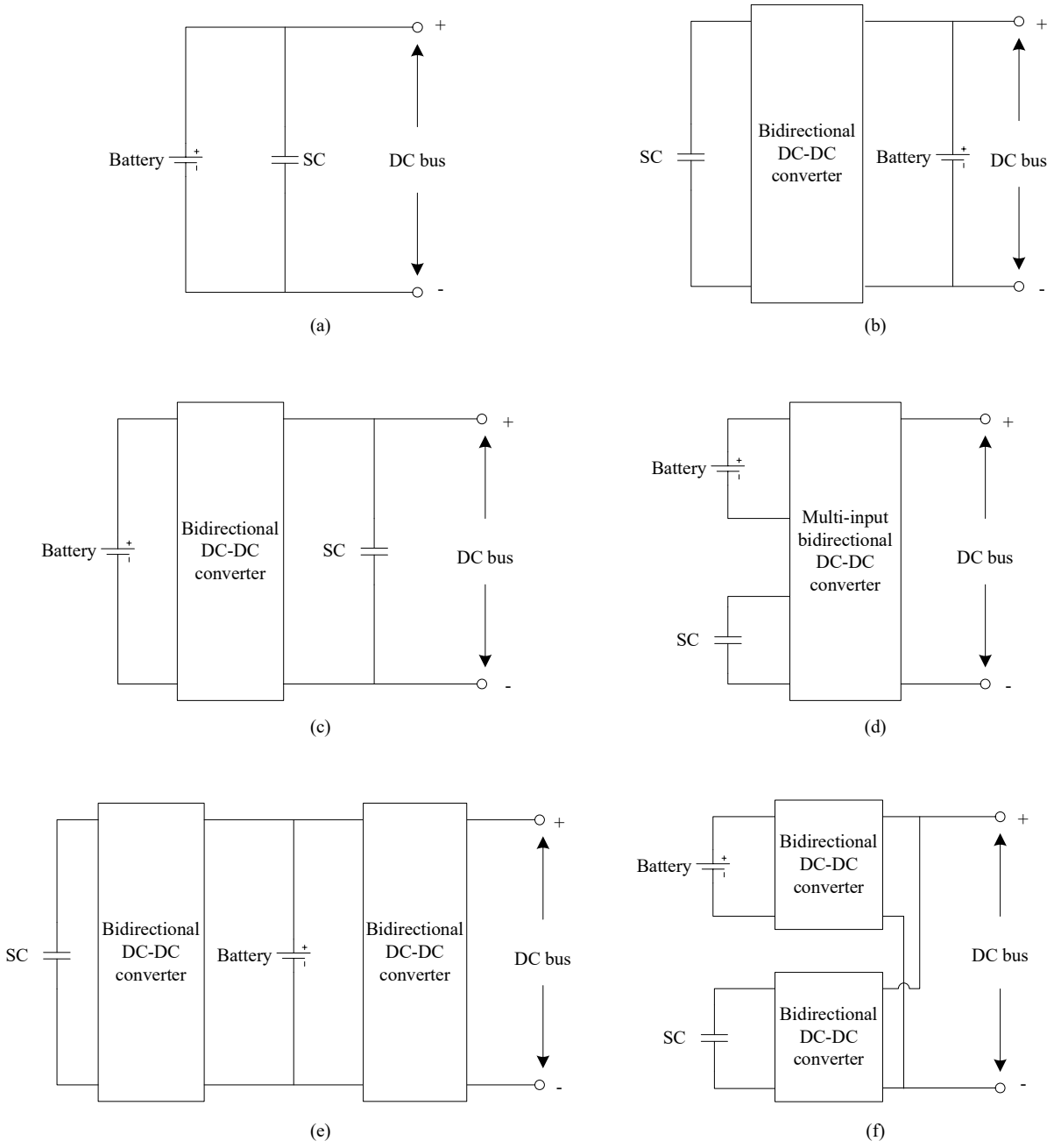

Figure 2.1. Topologies of battery-SC HESS. (a) Passive layout; (b) SC-Battery layout, (c) Battery-SC layout, (d) Multi-input layout, (e) Cascade layout, (f) Parallel layout

complexity and cost associated with the active architectures. The latter, presented in Figure 2.1(d), (e) and (f), involves full control over the two ES components. These architectures usually result in higher performances than the previous but at the cost of increasing complexity and investment.

With regard to the hybridization of a BESS, any of the above topologies can be considered when

retrofitting SC to the existing system. Nevertheless, an option may introduce additional drawbacks. For example, applying the multi-input topology may require a replacement, with the temporary unavailability of the HESS. Based on the power split algorithm, the battery's DC-DC converter in a parallel layout can experience a significant drop in efficiency due to load reduction.

2.3 BATTERY-SC HESS CONTROL FOR ELECTRICAL STRESS REDUCTION IN BATTERIES

Many control models have been previously reported on reducing the wear of BESS. Primarily based on mathematical programming, this includes [32] which proposes a battery ageing factor to be minimized simultaneously with the electricity cost, a control model aimed to penalize charging and discharging of batteries is developed in [33], [34] formulated a set of optimization constraints to ensure the state of health of batteries is kept above a threshold, and a state of charge (SoC)-driven control model is presented in [35].

In practice, large and sudden changes in battery current damage its health due to increased heat generation and internal resistance, resulting in further heating by the Joule's effect [36, 37, 38]. In the particular case of grid-tied renewable energy systems, the regulation bodies usually require each operator to ensure that the power profile is stable at the point of common coupling (PCC) [39, 40]. As a result, despite the implementation of wear control models, batteries will still be forced to handle the power fluctuations due to the presence of intermittent renewable generators such as wind turbines and solar photovoltaic (PV) panels. In this context, the implementation of battery-SC HESS is today regarded as a cost-effective means for addressing the above concern. Reasons for this include the feasibility and maturity of two ES technologies [41, 42, 43, 44]. Batteries are characterized by high energy density, but low power density and slow response speed, which are suitably complemented by the low energy density, high power density, and rapid response speed of SCs.

The positive impact of the battery-SC HESS passive topology on the battery with respect to power peak enhancement, internal losses reduction and service life extension has been previously studied under pulsed load [45], and pulsed charging sources [46]. However, as mentioned earlier, the current sharing between the two ES components depends upon their internal voltages and resistances. Accordingly, no power supervision is possible in this configuration.

Various models for power allocation between the battery and SC within a battery-SC HESS have been studied in the past. [47] reports DC-bus voltage-driven control algorithms that rely on the battery to ensure power balance in the DC grid, while the SC handles fast DC-bus voltage dynamics. A receding horizon control strategy for directing the fast and slow current components to the SC and battery, respectively, is proposed in [48]. In another study [36], it has been shown that the energy losses that occur in the SC lead to stress levels in the battery during operation. Thus, a model predictive controller is proposed that simultaneously minimizes the energy loss seen in the SC and the magnitude and fluctuations of the battery current. Somewhere else [49], a heuristic-based power split algorithm is proposed for a custom active parallel HESS, where only the SC is interfaced by a DC-DC converter. In this study, the paths and directions of power flow within the HESS are subject to several factors, such as the power balance, the terminal voltages of ES components and the SoC of the battery. [50] introduces a variable two-stage rate-limit scheme designed to optimize the speeds of charge/discharge and the amount of energy exchanged by the battery, taking into consideration the load requirement and the settling time. In this context, the SC complements the battery during transient phases. It can be observed that the above power management strategies focus on the HESS alone.

Control algorithms aimed to coordinate the power flow in renewable energy systems equipped with battery-SC HESS have been reported in the past. [40] proposes a heuristic power management scheme to ensure the dispatch of a grid-tied PV power plant in compliance with the Australian grid requirements. A variant of this model, more robust against forecasting errors, is reported in [51]. A heuristic receding horizon control that controls charging and discharging power flows in the battery was presented in [52]. Here the power output of a wind generator is decomposed in multiple layers using the wavelet theory. [53] presents an algorithm that features a dynamic rate limiter designed for grid-connected wave energy park. This rate limiter enables direct control over the amplitude of power variations in the battery. In another study, [54] proposes a power management framework for a grid-tied concentration photovoltaic plant, which embarks a second-order filter to achieve power allocation between the battery and SC. In [21], a dynamic hierarchical optimization model is investigated for real-time tracking of reference power specified by the grid manager. It is worth mentioning that the above control methods are primarily targeted at utility-scale renewable plants. Accordingly, little attention is paid to the local demand, like in smaller systems, where it plays a crucial role in the specification of control objectives.

A few studies considered the requirements associated with the presence of electrical loads to be supplied

on-site. [55] proposed a hierarchical framework for energy management in a power system comprising multiple distributed PV-SC-load hybrid renewable systems (HRS) and a centralized BESS. Using first-order filters, the net power deficit or excess of each HRS is split into high- and low-frequency components, which are respectively directed to the local SC and the central BESS. The power balance at the PCC is also maintained at all times. A heuristic aimed at regulating the DC-bus voltage and smoothing the power profile at the PCC is presented in [56]. In this study, the power split between the ES components is primarily driven by their respective SoC. [57] also propose a heuristic aimed to regulate the DC-bus voltage and the network voltage and frequency, depending on the network availability and the electricity price. Another heuristic for automatic selection of the operation mode of the battery among pre-set options is introduced in [58]. With the SC directly linked to the DC bus, the battery's operation mode that corresponds to the direction and amplitude of the current supplied by it varies with respect to the PV power output, the battery SoC and the power demand from local electrical loads. [59] proposes a heuristic aimed to assist in splitting the power excess or deficit between the public network and the battery-SC HEES of a PV-based HRS. This is achieved considering the nature and magnitude of the net power and the SoC of ES components.

In the case of existing HRS equipped with BESS, the above control models for battery-SC HESS will normally require a complete restructuring of the control system in place before the upgraded HESS can operate effectively. This situation can raise technical (shut-down, decommissioning), financial (decommissioning and disposal), and environmental (disposal of material) concerns, which will further delay the adoption of this hybrid ES by plant owners. Only a filtration-based control model proposed in [60] has been found suitable for smooth retrofit of BESS with SC in isolated PV/battery HRS. Using a probe connected upstream to the HESS, the high-frequency current components are extracted and used as control setpoints for the SC, which can directly feed the DC bus through a DC-DC converter. Direct benefits include decreased battery current fluctuations and improved battery health. While this control strategy could also be envisaged for existing grid-tied PV-battery HRS, significant fluctuations are still observed in the battery current profile after the upgrade with the SC. Failure to account for forecast information during power split can be cited among the key reasons for this reduced performance of the HESS. Next, the absence of the SC SoC in the control model exposes this ES component to frequent unavailability as soon as fully charged or discharged.

2.4 BATTERY-SC HESS CONTROL FOR THERMAL AND THERMOELECTRIC MANAGEMENT OF BATTERIES

In the past, thermal and thermoelectric management of batteries through adequate control of battery-SC HESS has much less attention compared to electrical stress reduction reviewed above. Depending on the technology involved, the battery temperature should remain within a specific range to ensure safety and an optimal trade-off between its operating performance and lifespan. This will be between 15°C and 35°C in the case of lithium-ion batteries [61], and around 25°C for lead-acid batteries [62]. Below those ranges, the battery cells start exhibiting sluggish chemistry, which translates into temporary capacity loss, a drop in efficiency and a reduction in power and energy densities. On the other side, higher temperatures cause irreversible degradation of electrodes, which results in accelerated ageing and capacity loss [63, 64, 65].

With the above in mind, various technologies have been proposed for battery cooling. This includes air cooling, liquid cooling, direct refrigerant cooling, phase change material (PCM) cooling, thermoelectric cooling, and heat pipe cooling [66, 67]. The resulting heat dissipation helps avoid a temperature rise in the battery. In the case of air cooling, this can be natural or forced using fans. It has been reported that the technologies with high heat transfer efficiency are often complex and costly to operate [68]. In the case of batteries operated in cold environments, warm-up techniques such as internal heating via battery resistance and external heating via resistive heaters and fluid circulation have been envisaged in the past [69]. These cooling and heating strategies are mainly targeted to BESS.

Thermal management of batteries in the context of battery-SC HESS has been investigated in a few research. [70] proposes a heuristic control for battery cooling. A passive configuration is used to supply the load under normal operating conditions. As soon as the battery temperature exceeds a threshold, the two ES devices are alternatively connected and disconnected to insert idle periods in the battery operation. This assists in slowing down heat generation inside the battery without the power supply interrupting the load. Despite the total absence of DC-DC converters, the strategy is relatively effective. This precludes an opportunity of introducing a control layer for electrical stress relief. [71] proposes a receding horizon control aimed at addressing the SoC and temperature imbalances within the battery and the energy losses in the DC-DC converters used to interface the battery and SC with the DC bus. While effective at balancing the temperature and energy across the battery cells/modules, little incidence is observed at the system level. A controller based on the pulse technique is proposed

in [72] to reduce the average battery current over each pulse cycle. While this is supposed to assist in cooling the battery, failing to account for the actual condition of the battery can yield unnecessary control and excessive workload for SC.

With regard to battery heating, a heuristic is proposed in [65] to reduce battery degradation and electricity costs for an electric vehicle powered by a battery-SC HESS operating at subzero temperatures. Here, the SC serves primarily to supply peak power demand, while the battery focuses on the baseload and emergencies. To ensure proper operation under ambient conditions between -20°C and 0°C, a heating kit consisting of a resistor and a fan is used to heat up the battery. However, the impact of heat generation by the ES components on the amount of external heat required is overlooked in this study.

The literature review above shows that the issue of power split within battery-SC HESS and that of battery thermal management have been studied separately in the past, although the shape and amplitude of the battery current can affect the latter. The few attempts to take advantage of the power split problem to achieve temperature regulation of the battery fail to relieve the batteries either at the power [70], or thermal [72, 65, 73] level. Moreover, the proposed control schemes are not designed for easy retrofitting of existing BESS.

2.5 ECONOMIC SIZING OF BATTERY-SUPERCAPACITOR HESS

A few research studies that address the economic sizing of battery-SC HESS have been reported in the past. [28] proposes a mathematical programming problem for the sizing of a stand-alone wind-photovoltaic HRS with battery-SC HESS. A similar model for a stand-alone HRS consisting of wind turbines, fuel cells, electrolyzers, batteries and SCs are reported in [30]. Given the characteristics of SC, an hourly control, as intended in the above studies, makes the presence of SC irrelevant. Further, the assumption of fixed service life for the battery and SC tends to overlook the critical impact of operating conditions on their actual lifespan. In [29], an optimization problem is formulated for the sizing of the battery-SC HESS of an electric vehicle taking into account the impact of DC-DC converters. The model has proved effective in reaching a trade-off between the storage capacity and the initial investment cost incurred. However, it suffers from a lack of comprehensive economic assessment over the vehicle's entire lifespan. In a study on the optimal sizing of battery-SC HESS for a fuel cell ship

[31], the battery degradation, voltage fluctuation, energy loss and capital cost of ES components are used to form the cost function to be minimized. Here also, the lack of comprehensive techno-economic assessment over the ship's lifespan is the main shortcoming of this model. [74] develops mathematical programming for sizing a battery-SC HESS, with the purchase costs of ES components and the battery capacity loss used to formulate the multi-objective function to be minimized.

Similarly to the above models, no assessment over the plant lifespan is considered. A hierarchical sizing model aimed to minimize the battery degradation cost, and the energy consumption of a plug-in hybrid electric vehicle is developed in [75]. Only a few factors relevant to the economic sizing of ES components ar considered in this work. [76] introduces mathematical programming for sizing the battery-SC HESS intended for frequency regulation applications. Here, an original capacity model is proposed to estimate the battery lifespan as a function of the SC size. In another study [27], the root-mean-square (RMS) of the battery current and the purchase cost of ES components is adopted as an objective function for the optimal sizing of the battery-SC HESS. Still, in another work [77], the purchase cost of SC and the capacity degradation of batteries are used to form multi-objective mathematical programming to size the ES components. A few factors of the capital costs (CAPEX) and O&M costs of battery-SC HESS are considered, which will cause a sub-optimal sizing of ES components.

2.6 CONCLUDING REMARKS

Based on the above review of the literature in Section 2.3, it is noted that the previous control schemes for battery-SC HESS are usually not suitable for retrofit of existing BESS with SC. In the particular case of HRS, the maximal use of renewable energy resources is usually not treated as a priority. For grid-tied HRS, limited attention is given to power stability during export towards the grid. To address these gaps, Chapter 3 will introduce a control framework for trouble-free retrofit of BESS installed in grid-tied HRS. This controller will aim at improving the power profile at the PCC, while relieving the battery from abrupt power variations.

Regarding thermal and thermoelectric management of batteries, Sections 2.3 and 2.4 indicate the problem of effective power split within battery-SC HESS and that of thermal management of batteries have been investigated separately in the past. To bridge this gap, Chapter 4 will introduce a fuzzy

logic controller aimed at thermoelectric management of batteries within battery-SC HESS. That the controller will also enable easy upgrades from BESS to battery-SC HESS is also considered. In the same vein, Chapter 5 will present a brief investigation on the relationship between the level of thermal stress sustained by the battery and the spatial arrangement of cells within a battery-SC HESS. It will be established that a adequate arrangement of ES cells can further support the thermal management of batteries considered in Chapter 4.

Finally, considering the market share of BESS, the adoption of battery-SC HESS will depend primarily upon a complete assessment of the costs and benefits of each alternative. However, Section 2.5 has revealed several shortcomings in the previous techno-economic models of battery-SC HESS. Moreover, their applicability to the retrofit of BESS with SC is not guaranteed. To address these gaps, Chapter 6 will present optimization programming for the cost-effective retrofitting of BESS into battery-SC HESS. The model will aim to size the SC and its DC-DC converter so that the life-cycle cost (LCC) of the resulting HESS is minimized.

CHAPTER 3 A HIERARCHICAL RECEDING HORIZON CONTROL FOR SUPERCAPACITOR-RETROFITTED GRID-TIED HYBRID RENEWABLE SYSTEMS

3.1 CHAPTER OVERVIEW

In this chapter, a two-layer control strategy is developed to easily retrofit SC into a grid-tied solar PV-battery HRS. It is assumed that a typical receding horizon controller is implemented to control the existing HRS. In this context, a new control layer is added to enable the effective operation of the upgraded system, with no or little modifications of the pre-existing architecture.

Given the complementary characteristics of batteries and supercapacitors, the new RHC layer will be coordinated with the one on-site to deliver a stable power profile at the PCC. The new control framework will also aim to remove fast variations in the battery power and increase the solar PV utilisation rate. Historical measurements of solar radiation in Pretoria, South Africa, were applied during the simulations to test the performances of the proposed strategy.

The rest of this chapter is structured as follows. Section 3.2 deals with the modelling of the grid-tied HRS. The proposed control framework is detailed in Section 3.3. The case study is introduced in Section 3.4. The simulation results are presented and discussed in Section 3.5. Concluding remarks are given in Section 3.6.

3.2 ENERGY MODELLING OF THE GRID-TIED HYBRID RENEWABLE SYSTEM

The HRS envisioned in this study is illustrated in Figure 3.1, where the equipment retrofitted to the existing system is indicated in the shaded area. The upgraded HRS, therefore, consists of solar PV panels, batteries, SC and electric loads. Power can be absorbed from the utility grid or injected into it at the PCC. Before the retrofit, the power flow across the power system was supervised by the power management unit 1 (PMU-1) alone. A circuit breaker (CB) enables the connection and disconnection of the utility grid by PMU-1. After the retrofit, the control signals sent to the PV and the CB are transferred to PMU-2, while the measurements are sent to both controllers. Only the battery remains fully controlled by PMU-1. A forecasting unit (not represented) supplies the two PMUs with forecast data about the load demand and the PV generation. It is worth mentioning that a single PMU with sufficient computation resources can play the role of both PMU-1 and PMU-2. In that case, no physical modifications are required to the original control infrastructure.

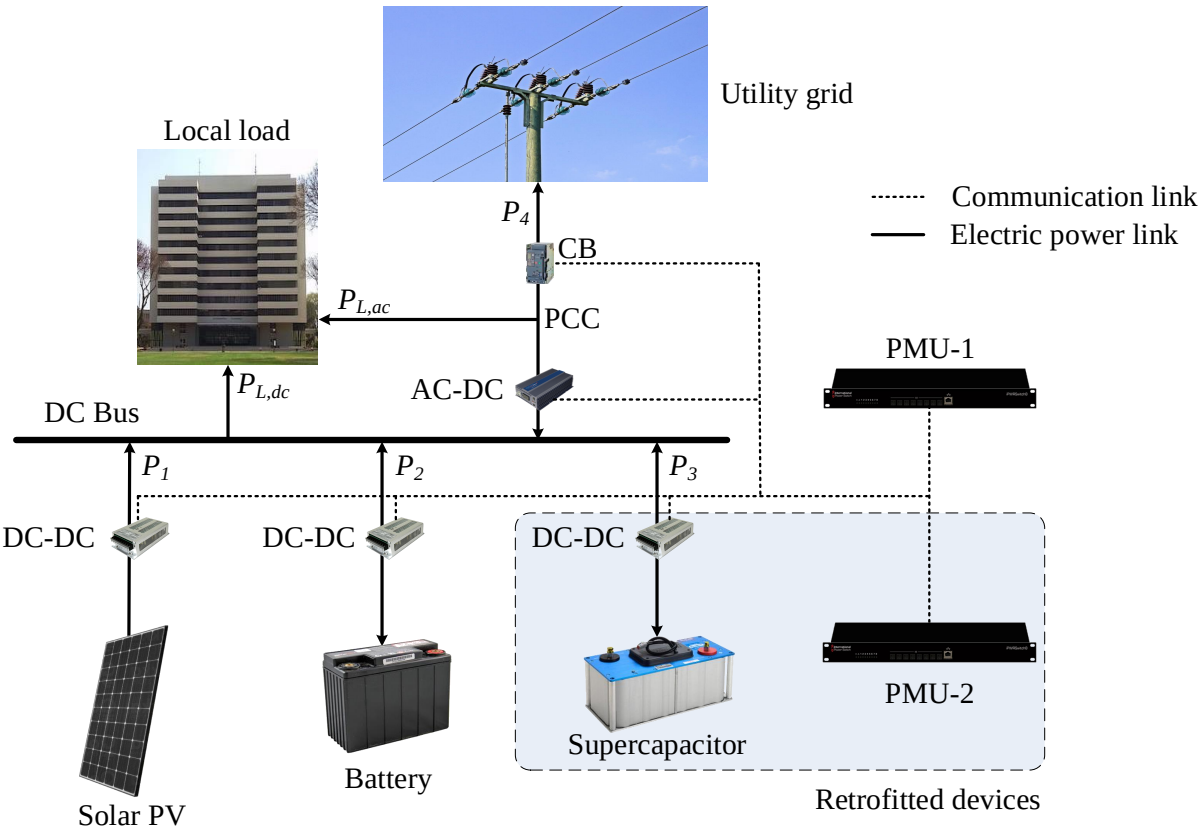

Figure 3.1. Layout of the grid-tied HRS

RHC schemes aim to minimize or maximize a specific performance criterion. For example, this consists in increasing self-sufficiency and encouraging the use of clean energy. In this case, the RHC scheme intends to minimize the power consumption from the grid and maximize the use of PV production. Considering the sampling rate of forecast data, relatively "large" control steps will be required to avoid rapid fluctuations of the battery power if battery lifespan is to be prioritized. This results in little margin to maintain power stability during export towards the utility grid. The opposite is experienced when the power quality at the PCC takes precedence over the battery's service life.

The proposed retrofit will help conciliate these two conflicting objectives and increase the use of solar energy at the same time. The rest of this section deals with the modelling of the HRS components.

3.2.1 Solar photovoltaic generator

The solar PV generator consists of panels that harvest solar radiation and convert it into DC power. The radiation that strikes the surface of collectors comprises three components: direct-beam radiation, diffuse radiation and reflected radiation.

The output power $P_{pv,BC}$ related to beam radiation $I_{BC}(k)$ that strikes the PV panel at a sample time k is expressed by [78]:

$$P_{pv,BC}(k) = \eta_{pv} I_{BC}(k) A_c. \tag{3.1}$$

Here, η_{pv} corresponds to the conversion efficiency of the PV panels, and A_c corresponds to the active area of the PV panels. Beam radiation is translated from the direct-beam radiation $I_B(k)$ (normal to the rays) by

$$I_{BC}(k) = I_B(k) \cos\theta(k), \tag{3.2}$$

with the incident angle $\theta(k)$ given by

$$\cos\theta(k) = \cos\beta(k)\cos(\phi_S(k) - \phi_C(k))\sin\psi + \sin\beta(k)\cos\psi. \tag{3.3}$$

In (3.3), $\beta(k)$ corresponds to the altitude angle, $\phi_C(k)$ corresponds to the azimuth angle of the panels, $\phi_S(k)$ corresponds to the solar azimuth angle, and ψ corresponds to the tilt angle of PV panels, as depicted in Figure 3.2.

In the absence of actual measurements of diffused radiation, the output power $P_{pv,DC}$ associated with this component is estimated by [78]

$$P_{pv,DC}(k) = \eta_{pv} C I_B(k) \left(\frac{1+\cos\psi}{2} \right) A_c, \tag{3.4}$$

with the sky diffuse coefficient C given by [78]

$$C = 0.095 + 0.04 sin\left[\frac{360}{365}(n-100) \right]. \tag{3.5}$$

Here, n corresponds to the day number in the year.

Similarly, in the absence of actual measurements of reflected radiation, the output power $P_{pv,RC}(k)$ associated with this component is estimated by [78]

$$P_{pv,RC}(k) = \eta_{pv} \rho I_B(k) \left(\sin\beta(k) + C \right) \left(\frac{1-\cos\psi}{2} \right) A_c, \tag{3.6}$$

where ρ denotes the ground reflectance.

Let $P_{pv}(k)$ denote the maximum power available to the PV system at sample time k. Given the above, this quantity is given by:

$$P_{pv}(k) = P_{pv,BC}(k) + P_{pv,DC}(k) + P_{pv,RC}(k). \tag{3.7}$$

Based on the operating conditions, the net power injected by the PV solar system, denoted by P_1 in Figure 3.1, can vary between zero and the maximum power available. This is expressed by

$$0 \leq P_1(k) \leq \eta_1 P_{pv}(k), \tag{3.8}$$

where η_1 corresponds to the efficiency of the DC-DC converter of the PV system. Whenever $P_{pv}(k) > P_1(k)/\eta_1$, the PV regulator (not shown in Figure 3.1) will limit its output power at $P_1(k)$. A variable resistor can also be used to dissipate the excess power.

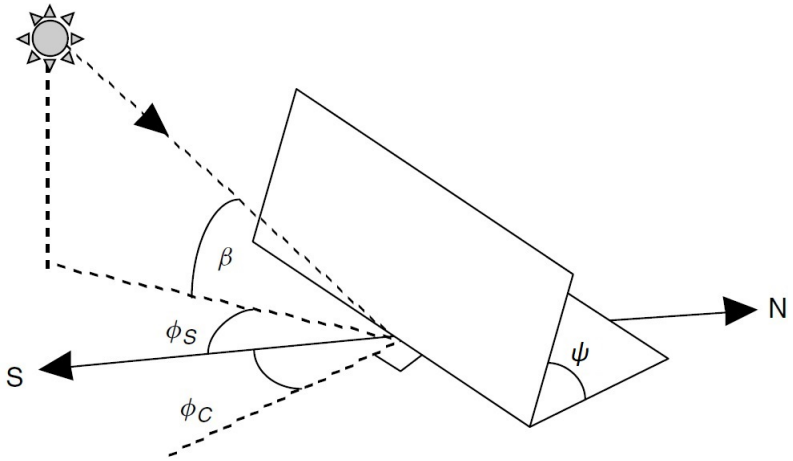

Figure 3.2. Collector azimuth angle $\phi_S(k)$, tilt angle ψ, solar azimuth angle $\phi_S(k)$ and altitude angle $\beta(k)$

3.2.2 Battery bank

The battery power P_2 can be decomposed into P_2^+ and P_2^-, which respectively denote the charging and a discharging components. The variations of the battery SoC with respect to charging and discharging operations can be estimated by

$$SoC_b(k+1) = SoC_b(k) + \frac{\eta_2 \eta_{b,c}}{E_{b,N}} P_2^+(k+1)\Delta T - \frac{1}{\eta_2 \eta_{b,d} E_{b,N}} P_2^-(k+1)\Delta T. \tag{3.9}$$

Here, $SoC_b(k+1)$ and $SoC_b(k)$ correspond the battery SoC at, respectively, sample times $k+1$ and k, η_2 corresponds to the conversion efficiency of the DC-DC converter of the battery, $\eta_{b,c}$ and $\eta_{b,d}$ correspond to charging and discharging efficiency, respectively, $E_{b,N}$ denote the battery's rated capacity, and ΔT denotes the sampling step. Considering (3.9), can be expressed as

$$SoC_b(k) = SoC_b(0) + \frac{\eta_2 \eta_{b,c}}{E_{b,N}} \sum_{\tau=0}^{k} P_2^+(\tau)\Delta T - \frac{1}{\eta_2 \eta_{b,d} E_{b,N}} \sum_{\tau=0}^{k} P_2^-(\tau)\Delta T, \tag{3.10}$$

where $SoC_b(0)$ the battery SoC at time instant zero.

To prevent deep discharge and overcharging, the battery SoC is subject to

$$\underline{SoC_b} \leq SoC_b(k) \leq \overline{SoC_b}, \tag{3.11}$$

where $\underline{SoC_b}$ and $\overline{SoC_b}$ denote the lower and upper bounds, respectively.

The battery power should not exceed a maximum bound $\overline{P_{b,ch}}$ and a minimum bound $\overline{P_{b,disch}}$.

$$0 \leq P_2^+(k) \leq \overline{P_{b,ch}}/\eta_2, \tag{3.12}$$

$$0 \leq P_2^-(k) \leq \eta_2 \overline{P_{b,disch}}. \tag{3.13}$$

The constraint below indicates that charging and discharging cannot take place at the same time

$$P_2^+(k)P_2^-(k) = 0. \tag{3.14}$$

The total battery power P_2 is therefore expressed by (3.15)

$$P_2(k) = P_2^-(k) - P_2^+(k). \tag{3.15}$$

3.2.3 Supercapacitors

The SC power P_3 consists of a charging component P_3^+ and a discharging component P_3^-. The SC SoC at sample time k, denoted by $SoC_{sc}(k)$, is expressed by

$$SoC_{sc}(k) = SoC_{sc}(0) + \frac{\eta_3 \eta_{sc,c}}{E_{sc,N}} \sum_{\tau=0}^{k} P_3^+(\tau)\Delta T - \frac{1}{\eta_3 \eta_{sc,d} E_{sc,N}} \sum_{\tau=0}^{k} P_3^-(\tau)\Delta T, \tag{3.16}$$

where $SoC_{sc}(0)$ denotes the initial SoC, η_3 corresponds to the conversion efficiency of the DC-DC converter of the SC, $\eta_{sc,c}$ and $\eta_{sc,d}$ denote, respectively, the charging efficiency and discharging efficiency of the SC, and $E_{sc,N}$ denotes the rated capacity of the SC.

At any sample time k, the SC SoC is subject to

$$\underline{SoC_{sc}} \leq SoC_{sc}(k) \leq \overline{SoC_{sc}}, \tag{3.17}$$

with $\underline{SoC_{sc}}$ and $\overline{SoC_{sc}}$ the lower and upper bounds, respectively.

The charging and discharging components of the SC power cannot take place simultaneously and should not exceed their respective upper bounds $\overline{P_{sc,ch}}$ and $\overline{P_{sc,disch}}$.

$$0 \leq P_3^+(k) \leq \overline{P_{sc,ch}}/\eta_3, \tag{3.18}$$

$$0 \leq P_3^-(k) \leq \eta_3 \overline{P_{sc,disch}}, \tag{3.19}$$

$$P_3^+(k)P_3^-(k) = 0. \tag{3.20}$$

The total SC power P_3 is therefore given by (3.21)

$$P_3(k) = P_3^-(k) - P_3^+(k). \tag{3.21}$$

3.2.4 Utility grid

The power flow P_4 between the HRS and the utility grid can be decomposed into two components: the power supplied by the utility grid, denoted by P_4^-, and the power injected by the HRS into to network, denoted by P_4^+. The following constraints ensure that the thermal capacity of electrical conductors between the HRS and the grid, denoted by $\overline{P_{tie}}$, is never exceeded:

$$P_4^+(k) \leq \overline{P_{tie}}, \tag{3.22}$$

$$P_4^-(k) \leq \overline{P_{tie}}. \tag{3.23}$$

Moreover, the power cannot flow in both directions at the same time

$$P_4^+(k)P_4^-(k) = 0. \tag{3.24}$$

The total power exchange between the network and the HRS is expressed by

$$P_4(k) = P_4^-(k) - P_4^+(k). \tag{3.25}$$

3.3 MODELLING OF RECEDING HORIZON CONTROLLERS

As indicated earlier, the existing grid-integrated HRS is assumed to have an RHC. This RHC model is first introduced, followed by the new controller's design.

3.3.1 RHC for grid-tied PV-battery HRS

In this study, the RHC that supervises the power across the existing HRS is implemented in PMU-1, as shown in Figure 3.1. The performance criterion can either maximize or minimize a certain function J, which can be purely technical (e.g. energy autonomy), economic (e.g. operation cost), environmental (e.g. carbon footprint), social (e.g. comfort level), or a combination.

The optimization problem to be solved at the beginning of each control interval also involves operational constraints, such as the power balance requirement and power and energy bounds. It is assumed that the existing RHC was designed to maximize simultaneously the self-sufficiency and the use of solar energy, which corresponds to minimizing the energy consumption from the utility grid and the energy shed from the PV systems. To limit the thermal stress sustained by the battery power, the sampling time ΔT is assumed to be in the range of minutes.

Given the above, the RHC strategy for the existing HRS is formulated as follows:

$$\min J(k) = \sum_{i=1}^{N_p} \Big[P_4^-(k+i) + \big(\eta_1 P_{pv}(k+i) - P_1(k+i)\big) \Big], \tag{3.26}$$

subject to

$$P_1(k+i) + P_2^-(k+i) - P_2^+(k+i) + \eta_4 P_4^-(k+i) - P_4^+(k+i)/\eta_4 = P_L(k+i), \tag{3.27a}$$

$$P_2^-(k+i) P_2^+(k+i) = 0, \tag{3.27b}$$

$$P_4^+(k+i) P_4^-(k+i) = 0, \tag{3.27c}$$

$$\underline{SoC_b} \le SoC_b(k) + \frac{\eta_2 \eta_{b,c}}{E_{b,N}} \sum_{\tau=k}^{k+i} P_2^+(\tau)\Delta T - \frac{1}{\eta_2 \eta_{b,d} E_{b,N}} \sum_{\tau=k}^{k+i} P_2^-(\tau)\Delta T \le \overline{SoC_b}, \tag{3.27d}$$

$$0 \le P_1(k+i) \le \eta_1 P_{pv}(k+i), \tag{3.27e}$$

$$0 \le P_2^-(k+i) \le \eta_2 \overline{P_{b,disch}}, \tag{3.27f}$$

$$0 \leq P_2^+(k+i) \leq \overline{P_{b,ch}}/\eta_2, \tag{3.27g}$$

$$0 \leq P_4^+(k+i) \leq \overline{P_{tie}}, \tag{3.27h}$$

$$0 \leq P_4^-(k+i) \leq \overline{P_{tie}}, \tag{3.27i}$$

with $i = 1, \cdots, N_p$. Here, N_p corresponds to the prediction horizon, η_4 corresponds to the conversion efficiency of the inverter next to the PCC, and the power demand $P_L(k+i)$ at time sample $k+i$ is determined by

$$P_L(k+i) = P_{L,dc}(k+i) + P_{L,dc}(k+i)/\eta_4 \tag{3.28}$$

Given the nonlinearity of (3.27b) and (3.27c), the optimization problem (3.26) and (3.27) is classified as a nonlinear programming (NLP) to be solved at each sample time k. Here, the optimization variables are P_1, P_2^-, P_2^+, P_4^-, and P_4^+.

3.3.2 Unified RHC for grid-tied PV-battery-SC HRS

The retrofit of SC to the HRS aims to: (1) reduce the influence of short-term fluctuations of solar radiation and load demand on achieving the operational objective expressed by the performance index; (2) stabilize the power flow at the PCC; (3) prevent frequent fluctuations of the battery power. From a control viewpoint, one way to operate the upgraded HRS is to replace the existing RHC scheme with a new one purposefully designed to achieve the above goals, considering the SC characteristics. In this case, a higher sampling frequency of forecast data and a shorter control step ΔT are required to enable the SC to contribute actively despite its low energy capacity.

The proposed RHC strategy for grid-tied PV-battery-SC HRS is detailed from (3.29) to (3.30p). Besides the revision of the power balance constraint in (3.30a) and the introduction of additional constraints related to the SC ((3.30d), (3.30i), (3.30m) and (3.30n)), a few extra constraints are also added to the previous RHC. In particular, (3.30b) keeps the grid power constant over N_g consecutive control intervals. On the other hand, the constraints (3.30f) and (3.30g) help maintain the battery power between the ramp-rates limits $\underline{\Delta P_2}$ and $\overline{\Delta P_2}$.

$$\min J(k) = \sum_{i=1}^{N_p} \Big[P_4^-(k+i) + \big(\eta_1 P_{pv}(k+i) - P_1(k+i)\big) \Big], \tag{3.29}$$

subject to

$$P_1(k+i)+P_2^-(k+i)-P_2^+(k+i)+P_3^-(k+i)-P_3^+(k+i)+\eta_4 P_4^-(k+i)-P_4^+(k+i)/\eta_4 = P_L(k+i), \tag{3.30a}$$

$$P_4^+(k+s) = P_4^+(k+r), \tag{3.30b}$$

$$P_2^-(k+i)P_2^+(k+i) = 0, \tag{3.30c}$$

$$P_3^+(k+i)P_3^-(k+i) = 0, \tag{3.30d}$$

$$P_4^+(k+i)P_4^-(k+i) = 0, \tag{3.30e}$$

$$\underline{\Delta P_2} \le P_2^-(k+m)-P_2^-(k+n) \le \overline{\Delta P_2}, \tag{3.30f}$$

$$\underline{\Delta P_2} \le P_2^+(k+m)-P_2^+(k+n) \le \overline{\Delta P_2}, \tag{3.30g}$$

$$\underline{SoC_b} \le SoC_b(k)+\frac{\eta_2\eta_{b,c}}{E_{b,N}}\sum_{\tau=k}^{k+i}P_2^+(\tau)\Delta T-\frac{1}{\eta_2\eta_{b,d}E_{b,N}}\sum_{\tau=k}^{k+i}P_2^-(\tau)\Delta T \le \overline{SoC_b}, \tag{3.30h}$$

$$\underline{SoC_{sc}} \le SoC_{sc}(k)+\frac{\eta_3\eta_{sc,c}}{E_{sc,N}}\sum_{\tau=k}^{k+i}P_3^+(\tau)\Delta T-\frac{1}{\eta_3\eta_{sc,d}E_{sc,N}}\sum_{\tau=k}^{k+i}P_3^-(\tau)\Delta T \le \overline{SoC_{sc}}, \tag{3.30i}$$

$$0 \le P_1(k+i) \le \eta_1 P_{pv}(k+i), \tag{3.30j}$$

$$0 \le P_2^-(k+i) \le \overline{P_{b,ch}}/\eta_2, \tag{3.30k}$$

$$0 \le P_2^+(k+i) \le \eta_2\overline{P_{b,disch}}, \tag{3.30l}$$

$$0 \le P_3^-(k+i) \le \eta_3\overline{P_{sc,disch}}, \tag{3.30m}$$

$$0 \le P_3^+(k+i) \le \overline{P_{sc,ch}}/\eta_3, \tag{3.30n}$$

$$0 \le P_4^+(k+i) \le \overline{P_{tie}}, \tag{3.30o}$$

$$0 \le P_4^-(k+i) \le \overline{P_{tie}}, \tag{3.30p}$$

with $i = 1,\cdots,N_p$, $m = n+1,\cdots,n+N_b-1$, $n = 0,N_b,2N_b,\cdots,N_p-N_b$, $s = r+1,\cdots,r+N_g-1$, and $r = 0,N_g,2N_g,\cdots,N_p-N_g$. Here, the optimization variables are P_1, P_2^-, P_2^+, P_3^-, P_3^+, P_4^-, and P_4^+.

Compared to the previous RHC scheme described in Section 3.3.1, the proposed RHC will increase the lifespan of batteries and deliver a smoother power profile at the PCC. However, considering the long prediction horizon N_p required for energy management purposes (ranging from 24 hours and above), the relatively short control step ΔT necessary for power quality reasons (in the order of tens of seconds), and the nature and size of the new RHC scheme, the above benefits are only achievable

at the expense of a significant increase in computing power and memory capacity to proceed with the implementation this unified control strategy. The next section proposes a less resource-intensive alternative.

3.3.3 Hierarchical RHC of grid-tied PV-battery-SC system

3.3.3.1 Architecture and design

Figure 3.3 shows the general architecture of the two-layer control framework investigated in this section. Keeping the RHC of the original PV-battery HRS as the upper layer, a second RHC scheme implemented in the control unit PMU-2 (see Figure 3.1) is run at the bottom layer to deliver a finer control. As indicated earlier, a single PMU with sufficient computation resources can replace the two units, thus avoiding partial changes in the existing control infrastructure.

The RHC at the upper layer is still used prior to the retrofit (see 3.3.1), with the only difference being that the control sequences calculated by the RHC for the PV and the grid are systematically discarded. As shown in Figure 3.3, the first set-point $P_2(k+1)$ in the optimal sequence obtained for the battery is implemented to control it and is passed on to PMU-2 for finer optimization at the next layer. As mentioned above, the prediction horizon of the existing RHC is in the range of one day and above to account for the cycles of solar energy and local demand. Further, a sampling step in the order of minutes is considered to increase the lifespan of batteries. As a result, the RHC executed at the upper layer provided in Section 3.3.3.2 is the same as that of the existing HRS in Section 3.3.1.

At the bottom layer, the next upper layer control step $k+1$ is further divided into even subintervals, as indicated in Figure 3.3. At the time instant $(k+1,l)$, which corresponds to the end of the current subinterval, the SC SoC, the set-point $P_2(k+1)$ of the battery power, and short-term prediction of solar radiation and load demand are submitted as input to the RHC at the bottom layer. The short-term prediction data submitted to PMU-2 are in the order of minutes, sampled at intervals of a few seconds. While keeping P_2 as determined by the upper layer to limit the thermal stress sustained by the battery, relevant constraints are introduced in the RHC at the bottom layer to ensure that a smooth power profile is delivered at the PCC, as detailed in Section 3.3.3.3. Upon completion of the computation cycle, the

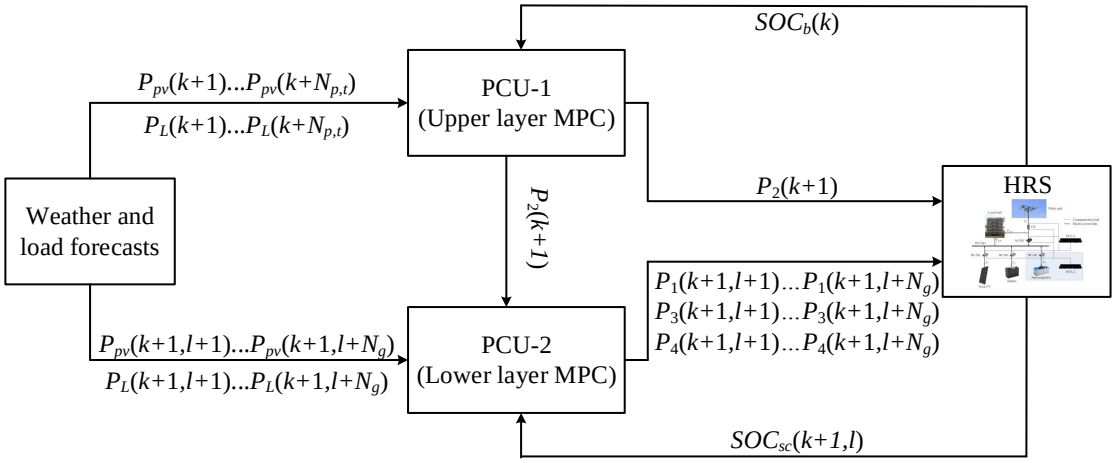

Figure 3.3. Control architecture of the hierarchical MPC strategy

first N_g elements of the control sequences of P_1, P_3 and P_4 obtained from PMU-2 are sent to the power conditioning units for implementation.

3.3.3.2 Upper layer RHC model

Since this RHC scheme is the same as that of the existing HRS, (3.31) to (3.32i) are copied from Section 3.3.1. Let the t subscript denote the upper layer variables. The RHC executed at the upper layer can be given below.

$$\min J_t(k) = \sum_{i=1}^{N_{p,t}} \left[P_{4,t}^{-}(k+i) + \left(\eta_1 P_{pv,t}(k+i) - P_{1,t}(k+i) \right) \right], \tag{3.31}$$

s.t.

$$P_{1,t}(k+i) + P_{2,t}^{-}(k+i) - P_{2,t}^{+}(k+i) + \eta_4 P_{4,t}^{-}(k+i) - P_{4,t}^{+}(k+i)/\eta_4 = P_{L,t}(k+i), \tag{3.32a}$$

$$P_{2,t}^{+}(k+i) P_{2,t}^{-}(k+i) = 0, \tag{3.32b}$$

$$P_{4,t}^{+}(k+i) P_{4,t}^{-}(k+i) = 0, \tag{3.32c}$$

$$\underline{SoC_b} \leq SoC_b(k) + \frac{\eta_2 \eta_{b,c}}{E_{b,N}} \sum_{\tau=k}^{k+i} P_2^{+}(\tau) \Delta T_t - \frac{1}{\eta_2 \eta_{b,d} E_{b,N}} \sum_{\tau=k}^{k+i} P_2^{-}(\tau) \Delta T_t \leq \overline{SoC_b}, \tag{3.32d}$$

$$0 \leq P_{1,t}(k+i) \leq \eta_1 P_{pv,t}(k+i), \tag{3.32e}$$

$$0 \leq P_{2,t}^{+}(k+i) \leq \overline{P_{b,ch}}/\eta_2, \tag{3.32f}$$

$$0 \leq P_{2,t}^{-}(k+i) \leq \eta_2 \overline{P_{b,disch}}, \tag{3.32g}$$

$$0 \leq P_{4,t}^{+}(k+i) \leq \overline{P_{tie}}, \tag{3.32h}$$

$$0 \leq P_{4,t}^{-}(k+i) \leq \overline{P_{tie}}, \tag{3.32i}$$

with $i = 1, \cdots, N_{p,t}$. Here, the optimization variables are $P_{1,t}$, $P_{2,t}^{-}$, $P_{2,t}^{+}$, $P_{4,t}^{-}$, and $P_{4,t}^{+}$.

3.3.3.3 Lower layer RHC model

Let the b subscript denote the lower layer variables. The MPC executed at the bottom layer is expressed by

$$\min J_b(k,l) = \sum_{j=1}^{N_{p,b}} \left[P_{4,b}^{-}(k+1,l+j) + \left(\eta_1 P_{pv,b}(k+1,l+j) - P_{1,b}(k+1,l+j) \right) \right], \tag{3.33}$$

s.t.

$$P_{1,b}(k+1,l+j) + P_{2,t}^{-}(k+1,l+j) - P_{2,t}^{+}(k+1,l+j) + P_{3,b}^{-}(k+1,l+j) - P_{3,b}^{+}(k+1,l+j) + \eta_4 P_{4,b}^{-}(k+1,l+j) - P_{4,b}^{+}(k+1,l+j)/\eta_4 = P_{L,b}(k+1,l+j), \tag{3.34a}$$

$$P_{4,b}^{+}(k+1,l+r) = P_{4,b}^{+}(k+1,l+s), \tag{3.34b}$$

$$P_{3,b}^{+}(k+1,l+j) P_{3,b}^{-}(k+1,l+j) = 0, \tag{3.34c}$$

$$P_{4,t}^{+}(k+1,l+j) P_{4,t}^{-}(k+1,l+j) = 0, \tag{3.34d}$$

$$\underline{SoC_{sc}} \leq SoC_{sc}(k+1,l) + \frac{\eta_3 \eta_{sc,c}}{E_{sc,N}} \sum_{\tau=l}^{l+i} P_3^{+}(k+1,\tau)\Delta T_b - \frac{1}{\eta_3 \eta_{sc,d} E_{sc,N}} \sum_{\tau=l}^{l+i} P_3^{-}(k+1,\tau)\Delta T_b \leq \overline{SoC_{sc}}, \tag{3.34e}$$

$$0 \leq P_{1,b}(k+1,l+j) \leq \eta_1 P_{pv,b}(k+1,l+j), \tag{3.34f}$$

$$0 \leq P_{3,b}^{+}(k+1,l+j) \leq \overline{P_{sc,ch}}/\eta_3, \tag{3.34g}$$

$$0 \leq P_{3,b}^{-}(k+1,l+j) \leq \eta_3 \overline{P_{sc,disch}}, \tag{3.34h}$$

$$0 \leq P_{4,b}^{+}(k+1,l+j) \leq \overline{P_{tie}}, \tag{3.34i}$$

$$0 \leq P_{4,b}^{-}(k+1,l+j) \leq \overline{P_{tie}}, \tag{3.34j}$$

where $l = 1, N_g + 1, 2N_g + 1, \cdots, (M-1)N_g + 1$, $M = \Delta T_t/(\Delta T_b N_g)$, $j = 0, \cdots, N_{h,b} - 1$, $r = 0, N_g, 2N_g, \cdots, N_{h,b} - N_g$, and $s = r+1, r+2, \cdots, r+N_g-1$. As previously, N_g corresponds to the number of control steps over which power flow at the PCC should remain constant. Here, the optimization variables are $P_{1,b}$, $P^-_{3,b}$, $P^+_{3,b}$, $P^-_{4,b}$, and $P^+_{4,b}$.

The operation of the hierarchical control strategy is summarized in the algorithm 1.

Algorithm 1 Hierarchical Receding Horizon Control

Upper layer

1: For time k, minimize (3.31) subject to (3.32)

Optimization outputs: $P_{1,t}(k+i)$, $P^-_{2,t}(k+i)$, $P^+_{2,t}(k+i)$, $P^-_{4,t}(k+i)$, and $P^+_{4,t}(k+i)$, with $i = 1 \ldots N_{p,t}$.

2: Pass $P^+_{2,t}(k+1)$ and $P^-_{2,t}(k+1)$ on to the bottom layer as a part of the optimization inputs.

Bottom layer

3: **for** $m = 0$ to $M-1$ **do**

4: Set $l = mN_g + 1$

5: Minimize (3.33) subject to (3.34)

Optimization outputs: $P_{1,b}(k+1, l+n)$, $P^-_{3,b}(k+1, l+n)$, $P^+_{3,b}(k+1, l+n)$, $P^-_{4,b}(k+1, l+n)$, and $P^+_{4,b}(k+1, l+n)$, with $n = 0 \ldots N_g - 1$.

6: **for** $n = 0$ to $N_g - 1$ **do**

7: Implement $P_{1,b}(k+1, l+n)$, $P^+_{2,t}(k+1)$, $P^-_{2,t}(k+1)$, $P^+_{3,b}(k+1, l+n)$, $P^-_{3,b}(k+1, l+n)$, $P^+_{4,b}(k+1, l+n)$, $P^-_{4,b}(k+1, l+n)$

8: **end for**

9: **end for**

3.4 CASE STUDY

Given the load profile in Figure 3.4(a) and the grid connection of the HRS [78], a 1-MW solar PV is envisaged to test and compare the performances of the different control strategies introduced in this study. Past measurements of the direct and diffuse solar radiations have been retrieved from the solar radiometric station installed at the University of Pretoria (25° 45' S and 28° 13.72'E) [79, 80]. The solar radiation data are applied to the PV arrays oriented South-North and tilted at 36°. The PV output power related to reflected radiation is estimated using (3.6), and the contributions due to direct-beam

and diffused radiations are calculated using (3.1) and (3.4), respectively. The conversion efficiency of solar panels is provided in Table 3.2.

To evaluate the controller performances over a full day and try to spare the battery from untimely setpoint changes, the prediction horizon and the control horizon at the upper layer are respectively set at 24 hours and 30 minutes. Given the control horizon applied at the upper layer and the energy content of the SC, the prediction horizon and the control horizon at the lower layer are respectively set at 30 minutes and five minutes. To ensure, on the one hand, the smooth functioning of the battery and a fast response of the SC, and on the other hand, to accommodate the capacity limitations of the PC, the sampling periods are set at 30 minutes and 10 seconds at the upper and lower layers, respectively. The solar radiation during a sampling interval of the upper layer is averaged using actual measurements sampled at a one-minute interval. The alleged effect of forecast errors and the difference in sampling speeds between the upper layer (one minute) and the lower layer (ten seconds) is mimicked by adding white Gaussian noise to the actual solar radiation data, with a signal-to-noise ratio (SNR) of 25dB. Similarly, the power demand at the bottom layer (sampled at 5-minute intervals) is derived from that of the upper layer (sampled at 30-minute intervals) by adding a white Gaussian noise with an SNR of 35dB. Compared to solar radiation, a higher SNR is applied to the load because, at a facility level, the load is usually more stable than solar radiation, which is directly affected by the displacement of clouds.

The energy storage system consists of a 250-kW/1464-kWh bank of lead-acid batteries [81] and a 13.1-MW/5.74-kWh bank of supercapacitors [82]. Table 4.3 details the rest of the simulation parameters. The model-plant mismatch (MPM) is assumed to be small enough to be handled by the proposed controller. Otherwise the control performance can be significantly deteriorated and even, in some cases, leading to shutdowns [83]. It should also be noted that this study does not consider the influence of time-varying electricity prices on the energy flow across the power system. Under such a tariff, in addition to the current performance measures, PMUs may also be required to prioritize the use of HESS during high-priced hours and to replenish it in low-priced hours.

Table 3.2. Parameters of the hybrid renewable system

Parameter	Value	Unit
Solar PV		
η_{pv}	0.124	
ρ	0.20	
Battery bank		
$E_{b,N}$	1 464	kWh
$\eta_{b,c}$	0.85	
$\eta_{b,d}$	1	
$\overline{P_{b,ch}}$ & $\overline{P_{b,disch}}$	250	kW
$\overline{SoC_b}$	0.9	p.u
$\underline{SoC_b}$	0.50	p.u
Supercapacitors		
$E_{sc,N}$	5.74	kWh
$\eta_{sc,c}$	0.80	
$\eta_{sc,d}$	1	
$\overline{P_{sc,ch}}$ & $\overline{P_{sc,disch}}$	4 857	kW
$\overline{SoC_{sc}}$	1	p.u
$\underline{SoC_{sc}}$	0.25	p.u
Utility grid		
$\overline{P_{tie}}$	1 200	kW
DC-DC converters		
η_1	0.90	
η_2, η_3	0.85	
AC-DC inverter		
η_4	0.95	

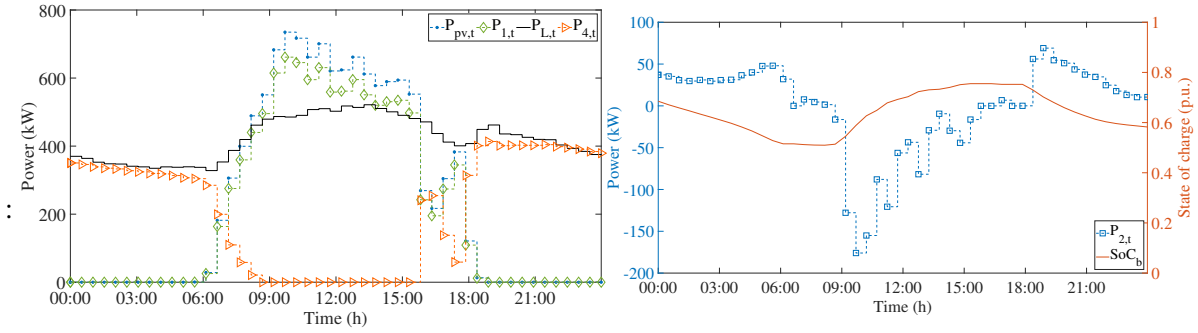

(a) Demand and power profiles of the PV and the grid

(b) Power and SoC of the battery

Figure 3.4. Demand profile and control inputs of original MPC strategy (upper layer)

3.5 SIMULATION AND DISCUSSION

A PC Core(TM) i5, 3.00 GHz, with 8 GB of RAM running Windows 10, was used to simulate the different control schemes presented earlier. Being nonlinear programming (NLP) type, the optimization problems were solved in MATLAB using the "fmincon" function. Given the limited resources of the PC, the short sampling period (10 seconds) and the long prediction horizon (24 hours), the unified RHC of grid-tied HRS introduced in Section 3.3.2 takes far too long to simulate. This scheme is, therefore, impractical for real-time control. As a result, going forward, the discussion involves only the RHC of PV-battery HRS and the hierarchical RHC of PV-battery-SC HRS. Furthermore, given that the former is identical to the upper layer of the latter, the discussion will compare the performances of the upper layer against those of the full hierarchical MPC.

3.5.1 RHC of grid-tied PV-battery power system (Upper layer)

Figure 3.4(a) displays the forecasted load profile $P_{L,t}$, the forecasted PV production $P_{pv,t}$ and the resulting PV power supply $P_{1,t}$ and the grid power $P_{4,t}$. The power and SoC of the battery are presented in Figure 3.4(b). It appears that at night and before daybreak, the public network supplies most of the energy needed by the HRS, with the participation of batteries until the minimum SoC is reached. During the daytime, PV power production primarily supplies the load and charges the battery. Only excess power is exported into the utility network.

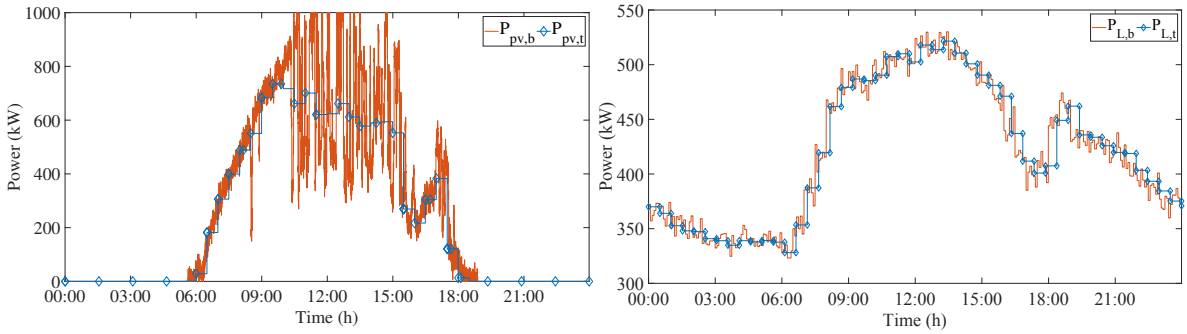

(a) PV generation **(b)** Load profile

Figure 3.5. Upper vs. bottom layer predictions of the PV production and the load demand

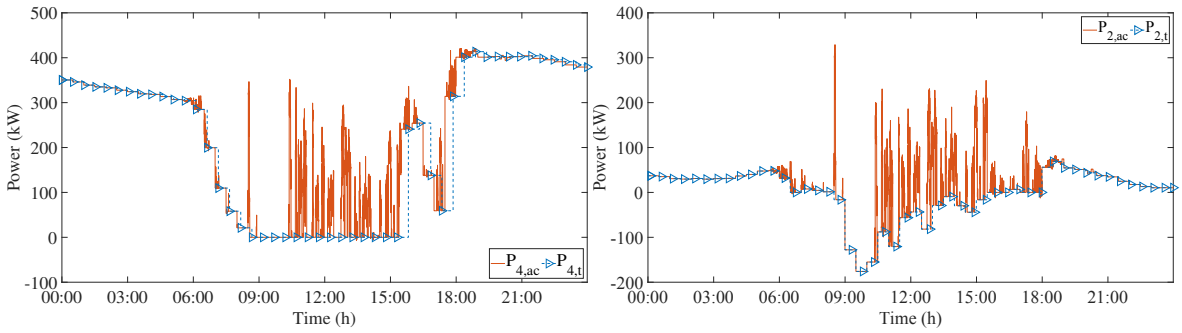

(a) Power flow at the PCC **(b)** Power flow of the battery

Figure 3.6. Optimized vs. actual power flows at the PCC and the battery

A superimposition of the PV production derived from the predictions at the upper layer and the bottom layer is displayed in Figure 3.5(a), and that of the load demand is displayed in Figure 3.5(b). To ensure the power system remains balanced, the excess and deficit caused by the fluctuations of the PV production and the load demand need to be handled by the public network or the battery. The resulting power profiles at the PCC and the battery are shown in Figure 3.6(a) and Figure 3.6(b), respectively. In Figure 3.6(a), $P_{4,ac}$ corresponds to the actual power profile at the PCC, assuming the fluctuations are handled by the network alone. Similarly, $P_{2,ac}$ denotes the actual battery power, assuming it takes care of the fluctuations alone. Figure 3.6 shows that, unless adequate actions are taken, the large peaks observed may affect the power quality of the electrical network through frequency instability or put at risk the safety and reduce the service life of batteries through overheating.

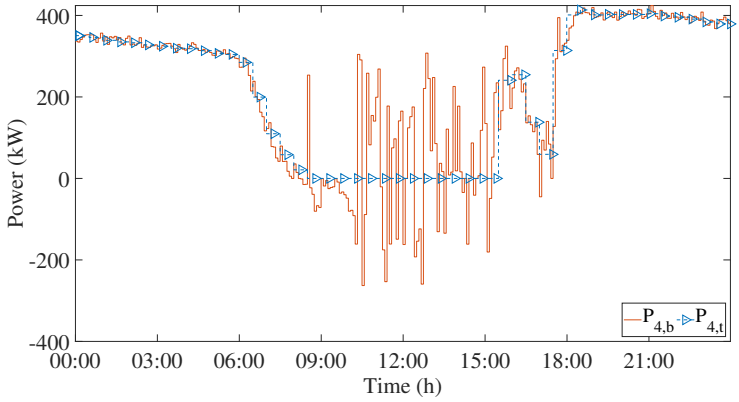

Figure 3.7. Power flow at the PCC: MPC PV-battery vs. Hierarchical MPC PV-batt-SC

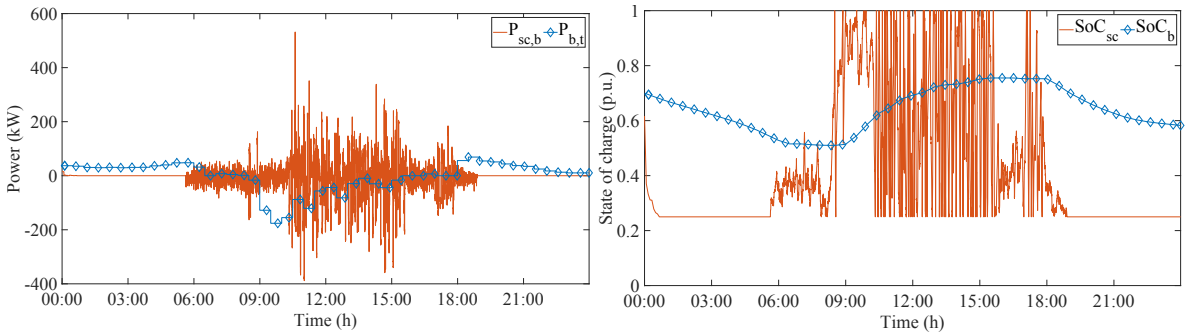

(a) Power flow comparison

(b) SoC comparison

Figure 3.8. Comparison of power and SoC profiles of the ESS components

3.5.2 Hierarchical RHC of grid-tied PV-battery-SC system

Figure 3.7 displays the power profile at the PCC before and after implementing a second RHC at the bottom layer. The additional controller proves to be effective at smoothing the power flow between the HRS and the grid and conditioning the PV production to maximize its use by the HRS. The increase observed in the amount of renewable energy exported to the electrical network contributes to the advent of eco-friendly networks at a minimum cost.

The comparison between the battery and the SC power profiles in Figure 3.8(a) establishes that the SC fully handles the fluctuations while the battery power varies slowly. Figure 3.8(b) shows that, like the battery, the SC gets depleted after sunset in an attempt to reduce the power import from the utility network.

3.5.3 Comparison of power and energy performances

A quantitative comparison between the existing control scheme and the hierarchical alternative can be conducted using the performance indicators given in Table 3.3. The second and third columns relate to the existing RHC before and after considering the effect of fluctuations, respectively. The last column relates to the hierarchical RHC scheme. It is noteworthy that the losses in the DC-DC converter of the PV contribute, with the dumping load, to the difference between the maximum PV production available and the actual supply of the PV plant. A comparison of the first two columns Table 3.3 indicates that the lack of capacity to handle the fluctuations of PV power and load demand prevents the HRS from benefiting from the increase in PV production over the implementation stage.

Regarding the use of the power injected by the PV plant, a smaller fraction is effectively supplied to the HRS, while an increased quantity (+12.13%) is shed or dissipated. Moreover, an increase in the import of electricity from the network without a significant counterpart is also observed. Depending on the entity responsible for power balancing, the frequency stability of the grid or the battery health may be jeopardized.

Looking at the last two columns in Table 3.3, it is observed that there is a net increase in the use of solar energy, with only 3.08% shed or dissipated. Despite the operation of SC causing a direct increase in the amount of energy imported from the network (+53.49 kWh), a net diminution (-245.12 kWh) is finally achieved through the extra electricity exported towards it. In addition, the hierarchical layout results in a better power profile at the PCC. The battery-SC HESS also provides greater support to the HRS without further solicitation of the battery.

3.5.4 Setting of the duration of the prediction horizon at the bottom layer

Table 3.4 shows the average and maximum computation times and the selected energy indicators as functions of the duration of prediction horizons at the bottom layer. As a general observation, the longer the prediction horizons, the better the performance. This is materialized by an increase in energy injection by the PV plant, a decrease in consumption from the network, and an increase in electricity exported towards it. Nevertheless, a similar trend is also observed in the computation time, which can negatively affect the implementability of optimal control sequences. Therefore, a trade-off is required

Table 3.3. Comparison between existing RHC and hierarchical RHC

Performance indicator	MPC (optimized)	MPC (actual)	Hierarchical MPC
PV energy generation (kWh)	5796.93	6153.18	6153.18
PV energy supply (kWh)	5217.24	4866.26	5348.00
PV energy dissipated (%)	0.00	12.13	3.41
Total energy import (kWh)	5187.26	5540.97[1]	5594.46
Total energy export (kWh)	0.00	14.86[1]	313.47
5-min intervals with stable P_4 (%)	100	66.67[1]	100
$max(\lvert P_2 + P_3 \rvert)$ (kW)	176.00	329.08[1]	509.03

[1] Fluctuations handled by the utility grid

Table 3.4. Duration of the lower layer prediction horizon vs energy performances

Predic. horiz.	Avg time[1]	Max. time[1]	PV supply[2]	Grid import[2]	Grid export[2]
5 min.	0.09	0.88	5301.84	5668.60	331.42
10 min.	0.42	9.39	5349.00	5594.46	313.47
15 min.	1.09	31.17	5380.64	5591.11	347.50
20 min.	3.45	125.07	5388.33	5591.42	352.72
30 min.	8.68	237.88	5387.80	5590.56	351.83

[1] in seconds; [2] in kWh

between the energy benefit and the extra computation time induced. In that regard, Table 3.4 indicates that a ten-minute prediction horizon leads to energy performances sensibly close to those obtained under longer prediction horizons but with a better average computation time. However, a five-minute prediction horizon might be preferable since the computation time under the ten-minute prediction horizon can reach up to 9 seconds.

3.6 CONCLUSIONS REMARKS

This chapter has reported on a hierarchical RHC framework aimed to facilitate the retrofit of supercapacitors to a BESS part of an existing grid-tied HRS, initially controlled by a typical RHC. By means of a second control layer, the proposed scheme operates the supercapacitor to deliver a stable power profile

at the PCC. Furthermore, the variable components of power requested from the HESS are handled by the supercapacitor alone, which allows the battery power to vary slowly. Simulations performed on a practical case study have proven the validity and effectiveness of the new control framework. Opportunities for compliance with power quality regulations, conditioning of the power generated by intermittent renewable sources, and lifetime extension for batteries have also been demonstrated.

CHAPTER 4 FUZZY LOGIC CONTROL OF PLUG-IN SUPERCAPACITORS FOR THERMOELECTRIC MANAGEMENT OF BATTERIES

4.1 CHAPTER OVERVIEW

This chapter presents a fuzzy logic controller (FLC) for plug-in SC intended for trouble-free upgrade of BESS into battery-SC HESS. Besides relieving batteries from fast-varying currents, the SC can also contribute to the supply of low-frequency currents. The latter assists in regulating the battery temperature and further reducing the magnitude of currents supplied by the battery.

In summary, the novelty of this study is as follows:

1. An original, cost-effective solution is proposed to easily retrofit BESS with SC without changing the existing control infrastructure.
2. The problem of battery ageing caused by high rate currents, usually overlooked, is addressed.
3. The proposed power split model assists in regulating the battery temperature, which also benefits the cooling and heating systems.

The rest of this chapter is structured as follows. The power system under study is described in Section 4.2. The design of the controller is carried out in Section 4.3. Section 4.4 presents the mathematical programming used to tune the controller parameters. The case study considered to test

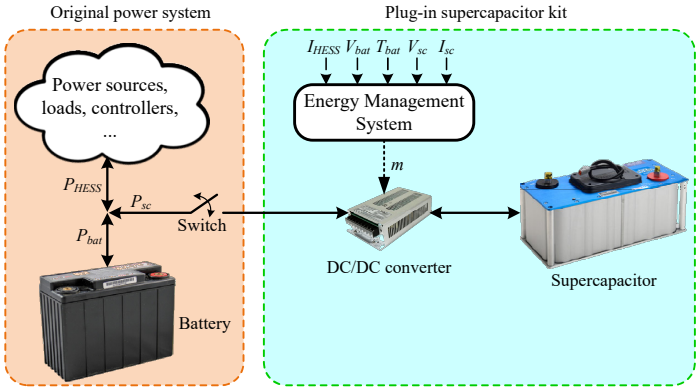

Figure 4.1. Layout of the battery-SC HESS

the proposed controller is given in Section 4.5. The simulation results are presented and discussed in Section 4.6. Conclusive remarks are given in Section 4.7.

4.2 POWER SYSTEM DESCRIPTION

Figure 4.1 shows the topology of the power system under study. The existing power system consists of a BESS, electric sources, consuming loads and relevant controllers. The plug-in kit includes SC storage, a bidirectional DC/DC converter, and an energy management system (EMS) that supervises the power flow from and to the SC. Measurements of the battery temperature and a few electric variables are periodically supplied to the EMS. In practice, the battery temperature can be accessed from sensors that feed the temperature compensation circuit and/or the battery monitoring interface.

In addition to the power allocation between the HESS components, the EMS also plays the following role:

- It assists in maintaining the battery temperature within the prescribed range;
- It keeps the SC SoC within the desired limits;
- It enables power to flow directly between the battery and SC whenever required.

4.3 CONTROLLER DESIGN

The control system implemented in the EMS is shown in Figure 4.2. It consists of a low-pass filter (LPF), a fuzzy inference system (FIS), a current controller, and a few arithmetic operators. The following sequence of operations is periodically performed as soon as the retrofit kit is plugged in. The required inputs are supplied to EMS: (1) the per-unit value i_{HESS} of the current I_{HESS} requested by the load from the HESS is filtered by the LPF to extract the low-frequency component, denoted by i_{lf}; (2) A subtraction operator uses i_{HESS} and i_{lf} to extract the fast-varying current, denoted by i_{hf}; (3) i_{lf} is then sent to FIS, which determines the low frequency current $i_{sc,lf}$ to be supplied by SC. To assist in managing the battery temperature and to increase the utilization rate of SC, the battery shell temperature T_{bat} and the deviation ΔSoC_{sc} of the SC SoC, denoted by SoC_{sc}, from the desired level SoC_{ref}, are also supplied to FIS; (4) The obtained value of $i_{sc,lf}$ is given at the output by FIS. SoC_{ref} will usually be halfway between the lower and upper bounds of SoC_{sc}, denoted by $\underline{SoC_{sc}}$ and $\overline{SoC_{sc}}$, respectively. Accordingly, ΔSoC_{sc} at sample instant k is expressed by

$$\Delta SoC_{sc}(k) = SoC_{sc}(k) - SoC_{ref}, \tag{4.1}$$

where $SoC_{ref} = (\underline{SoC_{sc}} + \overline{SoC_{sc}})/2$; (5) i_{hf} and $i_{sc,lf}$ are then summed up and converted back to SI value so as to determined the total current assigned to the SC, denoted by $I_{sc,req}$. (6) This set-point is finally enforced by the current controller, taking the values of the battery voltage V_{bat}, the SC voltage V_{sc}, and the SC current I_{sc} into consideration. The controller components are modelled in the rest of this section.

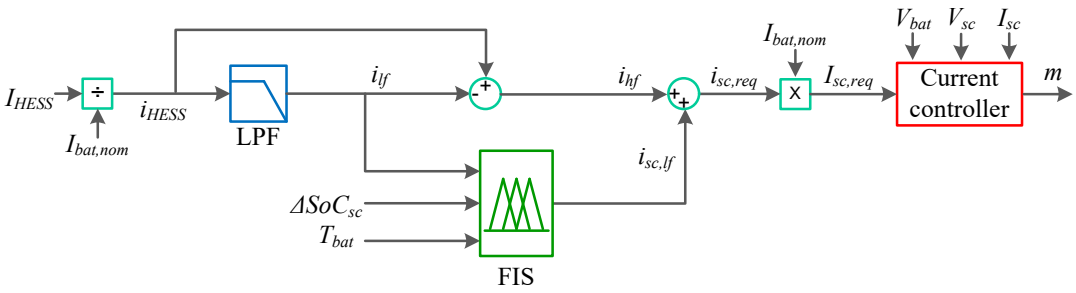

Figure 4.2. Proposed thermal-electrical controller for battery-SC HESS

4.3.1 Frequency split of the HESS total current

Considering the forward Euler method, the filtering action of LPF is expressed by

$$i_{lf}(k+1) = \left(1 - \frac{T_s}{T}\right) i_{lf}(k) + \frac{T_s}{T} i_{HESS}(k), \tag{4.2}$$

where $i_{lf}(0) = i_{HESS}(0)$. Here, T_s and T correspond respectively to the sample time and the filter's time constant in seconds. Accordingly, the high frequency current i_{hf} available at the subtraction block's output is expressed by

$$i_{hf}(k+1) = i_{HESS}(k+1) - i_{lf}(k+1). \tag{4.3}$$

Considering the fast change in polarity of i_{hf} and the use of $i_{sc,lf}$ to keep SoC_{sc} within the desired limits through power exchange with the load and the battery, i_{hf} can be assigned to SC in full.

4.3.2 Design of the fuzzy inference system

To mitigate the thermal stress and the high currents sustained by the battery while maintaining SoC_{sc} the desired range, the FIS assigns, on an ongoing basis, a portion of slow-varying current to SC taking into consideration its SoC, the battery temperature, and the magnitude and direction of i_{lf}. Previous studies on the performances of fuzzy logic control found the number (partitions) of membership functions (MFs), their approximate placement across the universe of discourse (or universe), and the degree of overlapping of MFs are of greater importance than their precise shapes [84]. Therefore, the trapezoidal shape is adopted for all the input MFs of FIS. Moreover, the intuitive method is used to determine the number and placement of MFs, while their overlapping and the parameters of output functions are optimized using Genetic Algorithm [84, 85]. Last, the Sugeno fuzzy inference is implemented in FIS, based on its computational efficiency and effective tuning by optimization techniques [86].

Considering the influence of the amplitude and polarity of i_{lf} on the HESS components, three MFs are assigned to i_{lf}: Negative High (NH), Low (L), and Positive High (PH), with L spreading on both sides of zero (no current). With regard to the current polarity, NH and the negative portion of L correspond to the charging current absorbed by the HESS, while the positive portion of L and PH correspond

discharging current supplied by the HESS. To maintain, as much as possible, SoC_{sc} around SoC_{ref}, three MFs are assigned to the input variable ΔSoC_{sc}: Negative High (NH), Low (L) and Positive High (PH), with L spreading on both sides of the central value (zero deviation). Previous experiments showed that for optimal performances, lithium-ion batteries should preferably be maintained between 15 °C and 35 °C, and lead-acid batteries around 25 °C [61, 62]. Accordingly, for both technologies, the universe of T_{bat} can be occupied by three MFs: Low (L), Medium (M) and High (H), with M spreading on both sides of the optimal temperature.

In devising the fuzzy logic rules, the governing principles to be followed are:

1. If T_{bat} is Medium, then SC gives moderate support to the battery in handling i_{lf}. This varies with the magnitude of i_{lf} and the SoC deviation ΔSoC_{sc}.
2. If T_{bat} is Low, then, taking "T_{bat} is Medium" as reference operating condition, double the current handled by the battery. This will halve the portion of i_{lf} allocated to the SC and doubles the current between SC and battery. However, no slow varying current is allocated to SC if ΔSoC_{sc} is Low.
3. If T_{bat} is High, then, taking "T_{bat} is Medium" as reference operating condition, half the current flow from/to the battery. This will double the portion of i_{lf} allocated to the SC and halve the current between SC and battery.

The general formulation of fuzzy logic rules of FIS is detailed in Tables 4.2. The following definitions apply to FIS's rule output levels (ROLs): NH for negative high, NM for negative medium, Z for zero, PM for positive medium, and PH for positive high. Based on the above governing principle, the parameters α, β and γ are such that:

- α=0.5, β=2 and γ=0 if T_{bat} is Low;
- α=1, β=1 and γ=1 if T_{bat} is Medium;
- α=2, β=0.5 and γ=2 if T_{bat} is High;

The formulation of ROLs as functions of input variables is detailed in Section 4.4.

Table 4.2. Generalized fuzzy logic rules of FIS.

		i_{lf}		
		NH	L	PH
ΔSoC_{sc}	NH	α·NH	β·NM	Z
	L	γ·NM	Z	γ·PM
	PH	Z	β·PM	α·PH

4.3.3 Current controller

The PI current controller, adapted from [87], and the electrical circuit that connects the SC in parallel with the battery are depicted in Figure 4.3. Here, L and R represent an inductor and its equivalent series resistance. Using the average model of the DC/DC converter, the plant to be controlled in the SC current control loop is modelled by (4.4) and (4.5)

$$V_{sc} - V_L = mV_{batt}, \tag{4.4}$$

$$V_L = RI_{sc} + L\frac{dI_{sc}}{dt}, \tag{4.5}$$

where V_L corresponds to the terminal voltage across the inductor. Adopting the inductor voltage as the control variable, the plant to be controlled is expressed by the Laplace transformation of (4.5) as

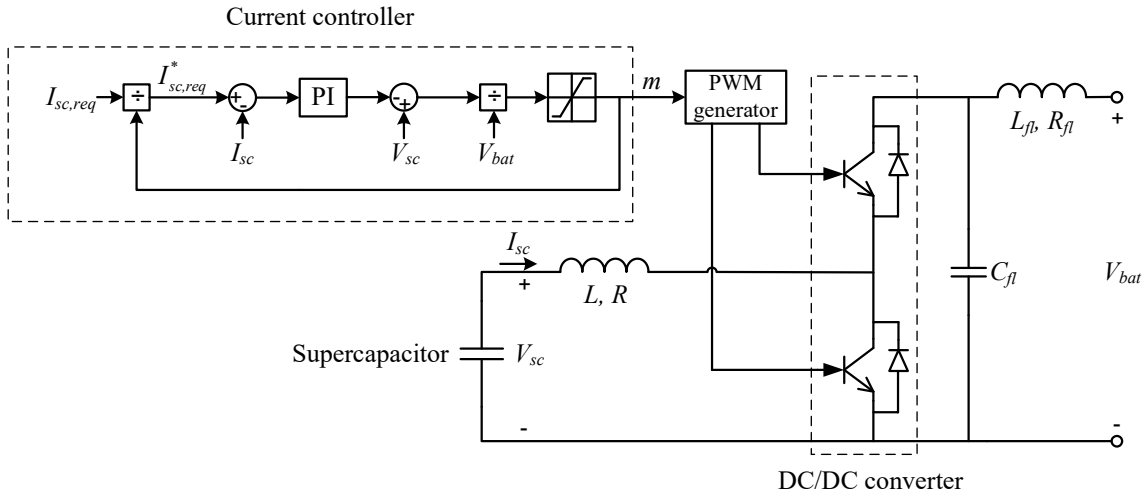

Figure 4.3. Current controller and power circuit of SC

follows

$$I_{sc}(p) = \frac{1}{Lp+R} V_L(p), \tag{4.6}$$

with p is the Laplace transform variable. Based on (4.4), the modulation index m is therefore expressed by

$$m = \frac{V_{sc} - V_{L,ref}}{V_{bat}}, \tag{4.7}$$

where $V_{L,ref}$ corresponds to the PI controller output [87]. The block diagram corresponding to the current controller is depicted in Figure 4.3. Here, $I_{sc,req}$ is divided by the modulation index m so that the SC set-point current is transferred from the battery side to the SC side of the DC/DC converter. In the Laplace domain, $V_{L,ref}$ is expressed by

$$V_{L,ref}(p) = \left(k_p + \frac{k_i}{p}\right) E(p), \tag{4.8}$$

where kp and k_i correspond respectively to the proportional gain and the integral gain of the PI controller, and $E(p)$ corresponds to the Laplace transform of the error signal expressed by

$$E(p) = I^*_{sc,req}(p) - I_{sc}(p). \tag{4.9}$$

4.4 OPTIMIZATION OF FIS PARAMETERS

4.4.1 Overview of Genetic Algorithms

Genetic algorithms refer to a population-based optimization technique inspired by both the natural selection theory and the evolutionary genetics [88, 89]. For an initial population of individuals (candidate solutions) to gradually evolve towards an optimum within a search space, three basic operations are applied by these algorithms to form a new generation from the previous population:

- Selection: consists of choosing a group of individuals (parents) aimed to be part of the next generation.
- Crossover: combines pairs of parents to form new individuals (children) for the next generation.

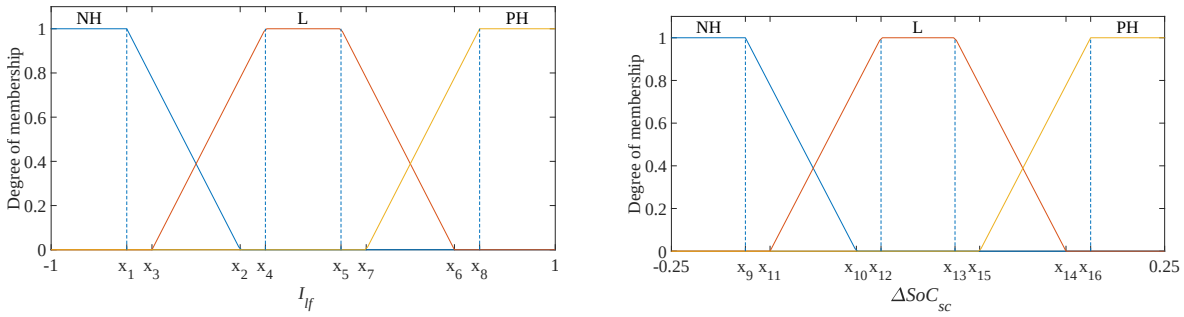

(a) Slow-varying component of I_{HESS}, i_{lf}

(b) Deviation of the state-of-charge of SC

Figure 4.4. Parameters of the input membership functions optimized by GA

- Mutation: consists of applying random alterations (mutations) to individuals to create new ones (children).

The individuals are compared to each other by means of their respective fitness values, which are determined by evaluating the function to be optimized, referred to as fitness function. Usually, parents with better fitness values are those likely to survive the selection process. Interested readers may refer to [89, 90] for further details about genetic algorithms.

4.4.2 Optimization model

The optimization problem solved by the Genetic Algorithm to obtain the parameters of FIS is introduced in this chapter.

4.4.2.1 Optimization variables and FIS output

The array X of optimization variables is made up of the parameters of input MFs and those of ROLs. The MF parameters of input variables optimized by GA are shown in Figure 4.4. It should be noted that the MF parameters of T_{bat} are not subject to optimization, as they have been derived from previous laboratory experiments. Having regard to the governing principles listed in Section 4.3.2, the ROLs of FIS can be generalised as follows:

$$z_k = \lambda_k(x_j i_{lf} + x_{j+1}\Delta SoC_{sc}), \tag{4.10}$$

where z_k ($k = 1,\ldots,27$) corresponds to any ROL in Table 4.2, $\lambda_k \in \Lambda = \{0, 0.5, 1, 2\}$, and x_j and x_{j+1} are parameters subject to optimization by GA, with j corresponds to the element index in the array X. Table 4.2 indicates that the determination of ROLs NH, NM, Z, PM and PH under medium T_{bat}, i.e, $\alpha = \beta = \gamma = 1$, is sufficient to derive the ROLs under low and high T_{bat}. Therefore, the remaining analysis of Table 4.2 will focus on medium battery temperature conditions unless stipulated otherwise.

The formulation of NH, NM, Z, PM and PH as functions of the optimization variables is conducted here. Table 4.2 indicates that the charge of SC under the ROL NH is closely depend upon the supply of a high-intensity current i_{lf} by the external circuit. Similarly, the discharge of SC under the ROL PH results primarily from supplying an intensive current i_{lf} to the external system. Considering the high intensity of i_{lf}, the component proportional to ΔSoC_{sc} in (4.10) appears to be redundant, and may even cause high current transients across the HESS. Accordingly, the parameters x_{j+1} in (4.10) are manually set at zero for both NH and PH. In the case of the ROL Z, x_j and x_{j+1} are equal to zero so that no slow-varying current is assigned to the SC. Lastly, Table 4.2 indicates that the ROL NM applies to "low ΔSoC_{sc}/negative high i_{lf}" and "negative high ΔSoC_{sc}/low i_{lf}" conditions. Similarly, the ROL PM applies to "low ΔSoC_{sc}/positive high i_{lf}" and "positive high ΔSoC_{sc}/low i_{lf}" operating conditions. As a result, the first term in the brackets of (4.10) should be the dominating term in the output when i_{lf} is of high intensity, while the second term should be the dominating term when ΔSoC_{sc} is high. Therefore, both x_k and x_{k+1} are needed for both NM and PM.

The above findings are summarized in Equations (4.11) to (4.15):

$$\text{NH} = x_{17} i_{lf}, \tag{4.11}$$

$$\text{NM} = x_{18} i_{lf} + x_{19} \Delta SoC_{sc}, \tag{4.12}$$

$$\text{Z} = 0, \tag{4.13}$$

$$\text{PM} = x_{20} i_{lf} + x_{21} \Delta SoC_{sc}, \tag{4.14}$$

$$\text{PH} = x_{22} i_{lf}, \tag{4.15}$$

where $x_{17},\ldots,x_{22}$ correspond to the ROL parameters subject to optimization.

Given (4.10), the final output $i_{sc,lf}$ of FIS is expressed by

$$i_{sc,lf} = \frac{\sum_{k=1}^{N} w_k z_k}{\sum_{k=1}^{N} w_k}, \tag{4.16}$$

where N=27 is the total number of rules, w_k corresponds to the rule firing strength derived from the rule antecedent and is expressed by

$$w_k = \min(F_1(i_{lf}), F_2(\Delta SoC_{sc}), F_3(T_{bat})). \tag{4.17}$$

Here, $F_1(...)$, $F_2(...)$ and $F_3(...)$ denotes the MFs for inputs 1, 2, and 3, respectively, and min is the mathematical function "minimum" implementing the fuzzy logical operator AND.

4.4.2.2 Fitness function

In this study, the fitness function $J(X)$ aims to minimize both the thermal and electrical stress sustained by the battery while maximizing the SC availability. $J(X)$ is therefore formulated as a multi-objective function consisting of three factors:

1. the root-mean-square (RMS) of the battery current [91], denoted by $J_1(X)$.
2. the mean deviation between the actual battery temperature and the recommended value, denoted by $J_2(X)$.
3. the mean absolute deviation of SoC_{sc} from SoC_{ref}, denoted by $J_3(X)$.

Accordingly, the fitness function to be minimized is expressed by

$$J(X) = v_1 J_1(X) + v_2 J_2(X) + v_3 J_3(X), \tag{4.18}$$

where v_1 to v_3 correspond to weighting coefficients, and $X = [x_1, x_2, \ldots, x_{22}]^T$ denotes the array of optimization variables identified above. It should be noted that the first two components of the objective function can be replaced by a single battery ageing model that features the deterioration related to both temperature and current intensity.

Let N denote the number of sample intervals within the optimization period. The normalized expression of J_1 is

$$J_1(X) = \frac{1}{I_{bat,nom}} \sqrt{\frac{1}{N} \sum_{k=1}^{N} I_{bat,k}^2(X)}, \tag{4.19}$$

with $I_{bat,k}(X)$ corresponds the battery current throughout the k-th sample interval.

The normalized expression of J_2 is

$$J_2(X) = \frac{1}{N(T_{max} - T_{ref})} \sum_{k=1}^{N} \mid T_{bat,k}(X) - T_{ref} \mid, \tag{4.20}$$

with T_{max} and T_{ref} correspond to the maximum attainable and the prescribed temperatures, respectively.

The normalized expression of J_3 is

$$J_3(X) = \frac{1}{N\Delta\overline{SoC_{sc}}} \sum_{k=1}^{N} \mid \Delta SoC_{sc,k}(X) \mid, \tag{4.21}$$

with $\Delta\overline{SoC_{sc}}$ the maximum deviation of SoC_{sc} from SoC_{ref}, and $\Delta SoC_{sc,j}$ is expressed by

$$\Delta SoC_{sc}(k) = SoC_{sc}(k) - SoC_{ref}. \tag{4.22}$$

Here, $SoC_{sc}(k)$ is determined using the Coulomb counting method given by:

$$SoC_{sc}(k) = SoC_{sc}(k-1) + \frac{I_{sc}(k)}{CV_{max}} T_s. \tag{4.23}$$

Here $I_{sc}(k)$ denotes the SC current throughout the sample time k, C denotes the SC capacitance in Farads, and V_{max} denotes the maximum terminal voltage of the SC in Volts.

Based on the lumped RC-thermal circuit model of the battery, its thermal behaviour is determined by

$$P_{bat} = C_{bat} \frac{dT_{bat}}{dt} + \frac{T_{bat} - T_a}{R_{b2a}}. \tag{4.24}$$

Here P_{bat}, T_{bat}, T_a, C_{bat}, and R_{b2a} denote, respectively, the battery heat generation, battery temperature, ambient temperature, thermal capacity of the battery, and thermal resistance between the battery and ambient air.

Since the ohmic heat varies proportionally to the square of the current, it will usually form the main source of heat production inside the battery under a large load current. Accordingly, the heat production inside the battery can be reduced to

$$P_{bat} = R_{bat} I_{bat}^2, \tag{4.25}$$

with R_{bat} the ohmic resistance of the battery. Substituting (4.25) into (4.24) yields after discretization

$$T_{bat}(k) = \left(1 - \frac{T_s}{C_{bat} R_{b2a}}\right) T_{bat}(k-1) + \frac{T_s}{C_{bat}} \left(R_{bat} I_{bat}^2(k) + \frac{T_{amb}}{R_{b2a}}\right). \tag{4.26}$$

4.4.2.3 Optimization constraints

The following constraints aim to retain the trapezoidal shape of MFs in Figure 4.4(a), and to keep their overlapping along the oblique sides:

$$x_1 - x_2 \leq 0 \tag{4.27}$$

$$x_1 - x_3 \leq 0, \tag{4.28}$$

$$-x_2 + x_3 \leq 0, \tag{4.29}$$

$$x_2 - x_4 \leq 0, \tag{4.30}$$

$$x_3 - x_4 \leq 0, \tag{4.31}$$

$$x_4 - x_5 \leq 0, \tag{4.32}$$

$$x_5 - x_6 \leq 0, \tag{4.33}$$

$$x_5 - x_7 \leq 0, \tag{4.34}$$

$$-x_6 + x_7 \leq 0, \tag{4.35}$$

$$x_6 - x_8 \leq 0, \tag{4.36}$$

$$x_7 - x_8 \leq 0, \tag{4.37}$$

The constraints below aims also to retain the trapezoidal shape of MFs in Figure 4.4(b), and to keep their overlapping along the oblique sides:

$$x_8 - x_{10} \leq 0 \tag{4.38}$$

$$x_9 - x_{11} \leq 0, \tag{4.39}$$

$$-x_{10} + x_{11} \leq 0, \tag{4.40}$$

$$x_{10} - x_{12} \leq 0, \tag{4.41}$$

$$x_{11} - x_{12} \leq 0, \tag{4.42}$$

$$x_{12} - x_{13} \leq 0, \tag{4.43}$$

$$x_{13} - x_{14} \leq 0, \tag{4.44}$$

$$x_{13} - x_{15} \leq 0, \tag{4.45}$$

$$-x_{14} + x_{15} \leq 0, \tag{4.46}$$

$$x_{14} - x_{16} \leq 0, \tag{4.47}$$

$$x_{15} - x_{16} \leq 0, \tag{4.48}$$

The constraint (4.49) ensures that the SC is charged by the battery whenever i_{lf} and ΔSoC_{sc} are respectively L and NH:

$$x_5 x_{18} + x_9 x_{19} \leq 0. \tag{4.49}$$

The constraint below aims to ensure that the charging of SC whenever i_{lf} and ΔSoC_{sc} are respectively NH and L:

$$x_1 x_{18} + x_{13} x_{19} \leq 0. \tag{4.50}$$

The constraint (4.51) ensures that the SC is in discharging mode whenever i_{lf} and ΔSoC_{sc} are respectively L and PH:

$$-x_4 x_{20} - x_{16} x_{21} \leq 0. \tag{4.51}$$

The constraint aims to ensure the discharge of SC whenever i_{lf} and ΔSoC_{sc} are respectively PH and L:

$$-x_8 x_{20} - x_{12} x_{21} \leq 0. \tag{4.52}$$

Given the fuzzy rules in Table 4.2, the following constraints ensure that the peak of the ROL NH is less than that of NM.

$$x_1 x_{17} - x_4 x_{18} - x_9 x_{19} \leq 0. \tag{4.53}$$

$$x_1 x_{17} - x_1 x_{18} - x_{12} x_{19} \leq 0. \tag{4.54}$$

Similarly, the following constraints ensure that the peak of the ROL PH is greater than that of PM.

$$x_8 x_{20} + x_{13} x_{21} - x_8 x_{22} \leq 0. \tag{4.55}$$

$$x_5 x_{20} + x_{16} x_{21} - x_8 x_{22} \leq 0. \tag{4.56}$$

The bound limits are such that

$$-1 \leq x_1, x_2, x_3, x_4 \leq 0. \tag{4.57}$$

$$0 \leq x_5, x_6, x_7, x_8 \leq 1. \tag{4.58}$$

$$\underline{\Delta SoC_{sc}} \leq x_9, x_{10}, x_{11}, x_{12} \leq \Delta SoC_{sc,avg}. \tag{4.59}$$

$$\Delta SoC_{sc,avg} \leq x_{13}, x_{14}, x_{15}, x_{16} \leq \overline{\Delta SoC_{sc}}. \tag{4.60}$$

$$1/4 \leq x_{17}, x_{19}, x_{21}, x_{22} \leq 1/2. \tag{4.61}$$

$$0 \leq x_{18}, x_{20} \leq 1/4. \tag{4.62}$$

The boundaries (4.61) on x_{17} and x_{22} translate in a relatively large current assigned to the SC when i_{lf} is of high intensity. The bound limits on x_{19}, x_{21} also translate in a relatively large current assigned to the SC when ΔSoC_{sc} is high. In both cases, the current supplied by SC will not exceed $\frac{1}{2} I_{bat,nom}$ so that the rules α·NH and α·PH in Table 4.2 under low battery temperature, and β·NM and β·PM in Table 4.2 under high battery temperature will not cause the low frequency current $i_{sc,lf}$ to exceed 1 p.u, i.e, $I_{bat,nom}$ in SI unit. The boundaries (4.62) applied to x_{18} and x_{20} cause the SC to handle a relatively small percentage of $i_{sc,lf}$ when it is medium, i.e, under NM and PM rules.

4.4.2.4 Optimization problem

In light of the above, the optimization problem to be solved by GA is stated as follows:

$$\min_{X} \quad J(X)$$

$$\text{s.t.} \quad G(X) \leq 0,$$

where J is described by (4.18), (4.19) and (4.21), G(X) is made up of equations (4.27) through to (4.62), and X is the array of the optimization variables introduced in Section 4.4.2.1. Algorithm 2 details the steps followed in determining the fitness value of an individual, i.e, a candidate solution X to the optimization problem.

4.5 CASE STUDY

A battery-SC HESS consisting of four 3.6V lithium-ion battery cells and twelve 2.7V SC cells is considered for simulation. The technical parameters of these storage devices are given in Table 4.3. To ensure a stable operation after retrofitting the SC to the existing BESS and to prolong the SC service life, the variation of SoC_{sc} is restricted between 0.5 and 1. In order To test the controller under normal and extreme operating conditions, the following scenarios are considered:

Algorithm 2 Determination of individual fitness by Genetic Algorithm

1: Build FIS using X, Figure 4.4, Table 4.2, and (4.11) to (4.15)
2: **for** $k = 1$ to N **do**
3: Determine $i_{lf}(k)$ and $i_{hf}(k)$ from i_{HESS}, (4.2) and (4.3)
4: Compute $i_{lf,sc}(k)$ from FIS, with $i_{lf}(k)$, $\Delta SoC_{sc}(k)$ and $T_{bat}(k)$ as inputs
5: $I_{sc,req}(k) \leftarrow (i_{hf}(k) + i_{sc,lf}(k))I_{bat,nom}$
6: $I_{sc}(k) \leftarrow I_{sc,req}(k)$
7: $I_{bat}(k) \leftarrow I_{HESS}(k) - I_{sc}(k)$
8: Determine $T_{bat}(k+1)$ from (4.26), and $\Delta SoC_{sc}(k+1)$ from (4.22) and (4.23)
9: **end for**
10: Determine $J_1(X)$, $J_2(X)$ and $J_3(X)$ from (4.19), (4.20) and (4.21), respectively
11: $J(X) \leftarrow v_1 J_1(X) + v_2 J_2(X) + v_3 J_3(X)$.

- Scenario I — Optimal conditions: T_{amb} and $T_{bat}(0)$ are both set at 25 °C, $SoC_{sc}(0)$ is set around 75 %, and i_{HESS} has a non-zero profile.
- Scenario II.a — Low temperature mode: T_{amb} and $T_{bat}(0)$ are both set at 5 °C, $SoC_{sc}(0)$ is set around 75 %, and i_{HESS} has a non-zero profile.
- Scenario II.b — High temperature mode: T_{amb} and $T_{bat}(0)$ are both set at 45 °C, $SoC_{sc}(0)$ is set around 75 %, and i_{HESS} has a non-zero profile.

Together, these scenarios provide the full picture of the control performances.

4.6 SIMULATIONS AND DISCUSSION

4.6.1 Controller parameters

Figure 4.5 shows the load profile obtained from the U.S. guideline intended for the determination of duty cycle for energy storage systems in PV smoothing applications [94]. This current profile corresponding to I_{HESS} was applied to the battery-SC HESS to compute the array X of optimization variables. In the rest of this chapter, the sign convention is such that a negative current charges the storage device, and the opposite applies to positive current. Figure 4.6(a) displays the convergence curve obtained for this case study subject to the load profile in Figure 4.5. Figure 4.6(b) presents

Table 4.3. Simulation parameters for testing of the battery-SC HESS controller

Parameter	Value	Unit	Parameter	Value	Unit
`Battery cells` [70, 92]			`GA parameters`		
$E_{batt,nom}$	8.64	Wh	$v_1; v_2$	0.25; 0.25	
$V_{batt,nom}$	3.60	V	v_3	0.5	
$I_{batt,nom}$	2.20	A	Population size	100	
R_{batt}	0.10	Ω	Elite count	5	%
$C_{batt,cell}$	17.26	J/°C	Crossover fraction	0.8	
$R_{b2a,cell}$	6.84	°C/W	`Low-pass filter`		
# in series	4		T	100	sec
`SC cells` [93]			`Current controller`		
$C_{sc,nom}$	450.00	F	k_p	1.85	
$V_{sc,nom}$	2.70	V	k_i	2720	
$R_{sc,cell}$	2.80e-3	Ω	`DC-DC converter`		
$R_{b2a,cell}$	6.84	°C/W	L, L_{fl}	0.56	mH
# in series	6		R, R_{fl}	0.09	Ω
# in parallel	2		C_{fl}	72.73	mF
			Switching frequency	20	kHz

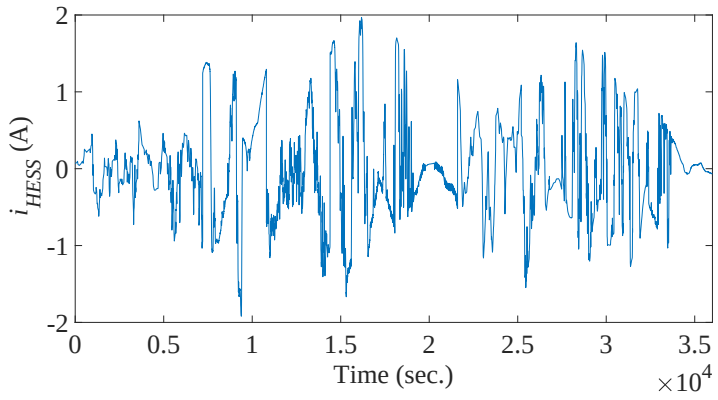

Figure 4.5. Sandia National Laboratory's load profile for determination of duty cycle for energy storage systems in a PV smoothing application

the MFs of T_{bat} derived from previous experiments on Li-ion batteries [61]. The array X of optimal controller parameters is as follows: $X =$ [-0.6981; -0.3797; -0.5292; -0.2025; 0.2417; 0.6537; 0.3508; 0.8789; -0.2328; -0.1841; -0.2067; -0.1020; 0.0127; 0.1845; 0.1014; 0.2427; 0.3896; 0.2054; 0.3053; 0.1785; 0.3317; 0.3600]. The membership functions of i_{lf} and ΔSoC_{sc} are given in Figure 4.6(c) and Figure 4.6(d), respectively.

The remaining of this section is devoted to testing the proposed controller and to comparing its performances to those of the BESS and battery-SC HESS controlled by the LPF alone. To this end, three distinct scenarios have been considered: normal operation conditions (Scenario I), low ambient temperature conditions (Scenario II.a), and high ambient temperature conditions (Scenario II.b).

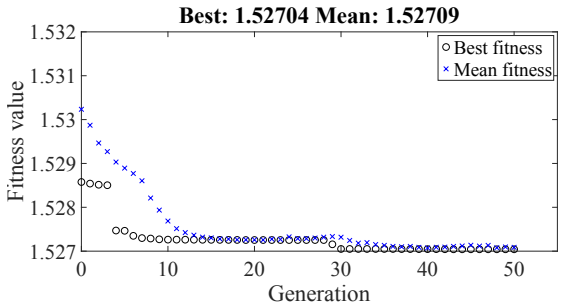

(a) Convergence curve of Genetic Algorithm

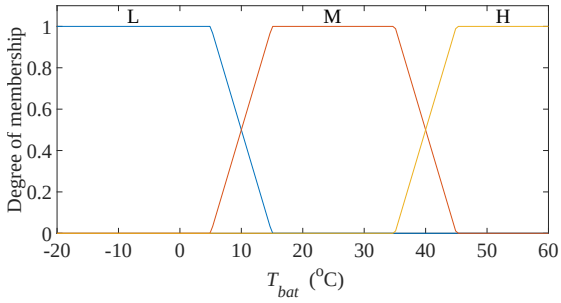

(b) Membership functions of T_{bat} for Li-ion batteries

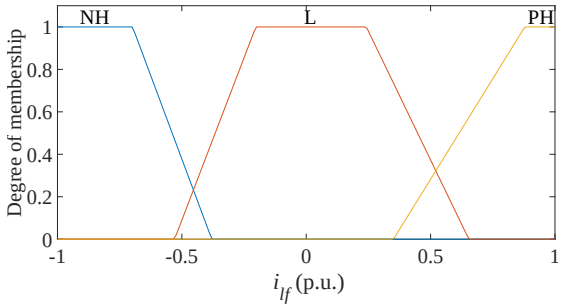

(c) Membership functions of i_{lf}

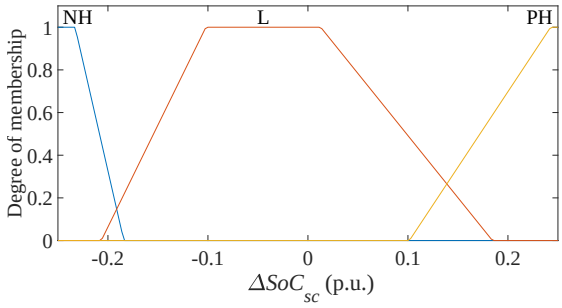

(d) Membership functions of ΔSoC_{sc}

Figure 4.6. Optimization outputs from Genetic Algorithm

Table 4.4. Performance indexes under normal and critical operating modes

Simulation	J_1			J_2			J_3		
	BESS	HESS,w/o	HESS,w	BESS	HESS,w/o	HESS,w	BESS	HESS,w/o	HESS,w
Scenario I	0.6398	0.5476	0.4722	0.0018	0.0014	0.0012	-	0.0062	0.0050
Scenario II.a	0.8854	0.7099	0.8796	0.5665	0.5674	0.5665	-	0.0215	0.0002
Scenario II.b	0.8854	0.7099	0.5405	0.5773	0.5762	0.5751	-	0.0140	0.0336

4.6.2 Scenario I: Controller performance under normal operating conditions

The battery-supercapacitor HESS and the proposed controller were subsequently implemented in Simulink/Matlab. Figure 4.7 shows the current profiles assuming a fast-varying load, with the ambient and initial battery temperatures set at 25°C. Here, the subscript *w/o* denotes the performance achieved when the SC is controlled by the LPF alone, while *w* denotes the performance under the full implementation of the controller investigated in this chapter. One can observe that the LPF causes the SC to handle the spiky components of I_{HESS}. The current supplied by the battery within the LPF-controlled HESS (Figure 4.7(b)) is, therefore, smoother than that of the original BESS (Figure 4.7(a)). Figure 4.7(c) shows the current profile of the SC, characterized by rapid fluctuations. Under full deployment of the proposed EMS, the FIS restricts the supply of high intensity current by the battery. This is achieved by diverting part of the slow-varying component of I_{HESS} towards the SC, as shown in Figure 4.7(d). Under normal operating conditions, the SC contributes up to 18.28% in the supply of low-frequency current by the HESS. In comparison to BESS and HESS,w/o alternatives, Table 4.4 indicates that the RMS value of the battery current (J_1) decreases by, respectively, 26.20% and 13.77% under the proposed controller. One can also note moderate improvement in the deviations of battery temperature (J_2) and SC SoC (J_3) from desired values.

Figure 4.8 displays the variation of battery temperature, assuming that the current profiles given in 4.7(a) and (b) repeat continuously over six hours.

Based on previous studies on the cyclic ageing of Li-ion batteries [95, 96], the capacity loss is expressed by

$$Q_{bat,loss} = B(C)\exp\left(\frac{-31700+370.3C}{RT_{bat}}\right)(A_h)^z, \tag{4.63}$$

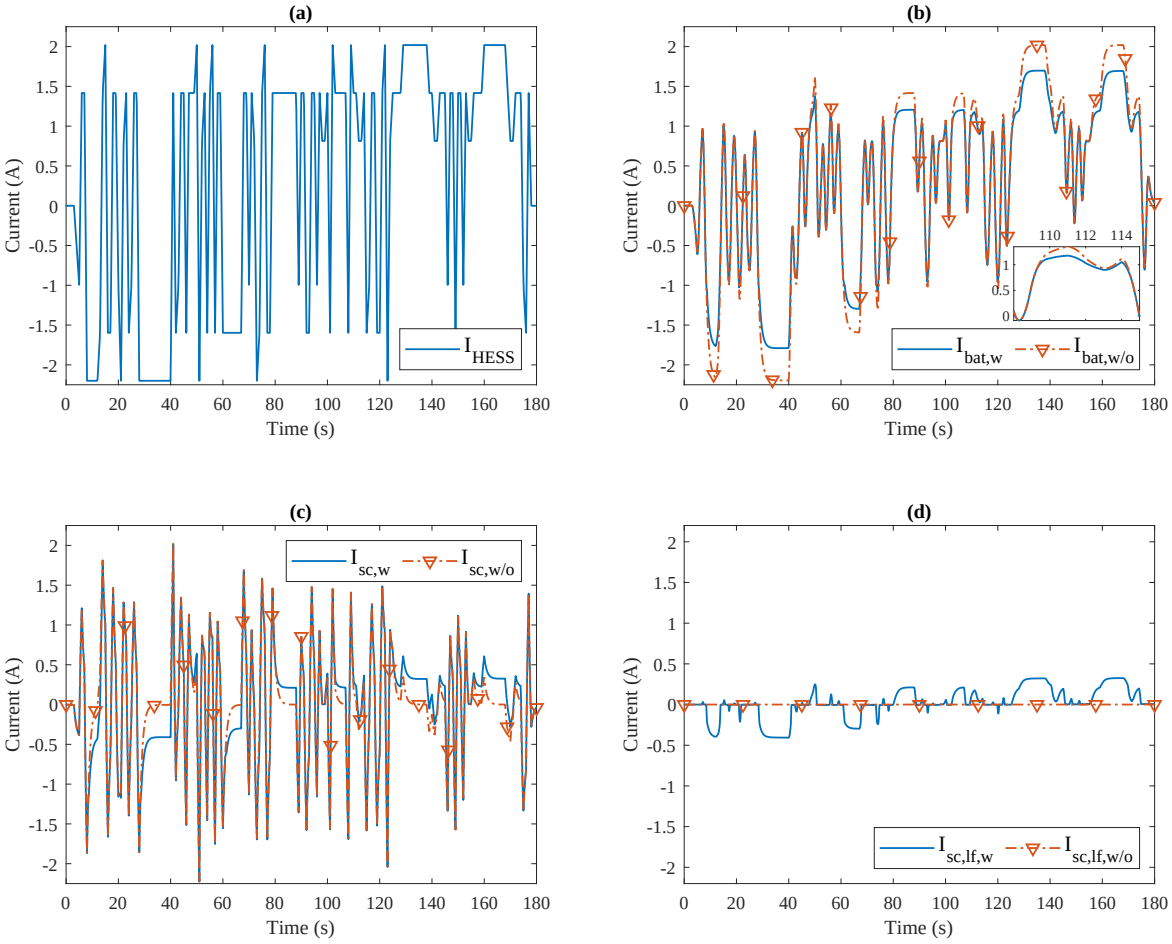

Figure 4.7. Current profiles under a fast-varying load. (a) Total current requested from the HESS. (b) Battery current. (c) SC current. (d) Low-frequency content of SC current.

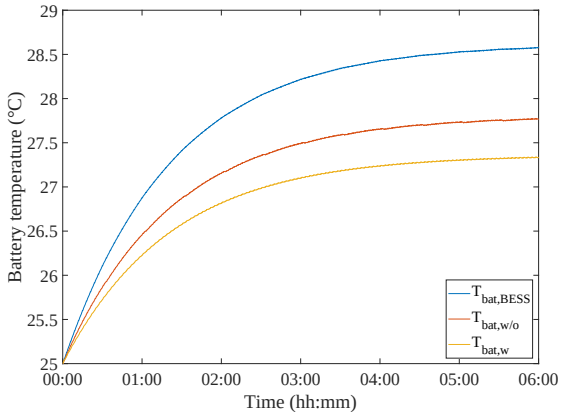

Figure 4.8. Variation of battery temperature under scenario I

with

Table 4.5. Assessment of theoretical battery ageing

	$I_{bat,RMS}$ (A)	$T_{bat,SS}$ (°C)	$T_{bat,avg}$ (°C)	$Q_{bat,loss}$ (%)	Lifespan (hours)
BESS	1.408	28.623	27.803	0.330	60.575
HESS,w/o	1.200	27.802	27.174	0.304	65.777
HESS,w	1.004	27.361	26.833	0.282	70.872

$$B(C) = 25623.71C^{-0.28}. \tag{4.64}$$

Here, B is the pre-exponential factor; C corresponds to the C-rate; R is the ideal gas constant equal to 8.314 J(kg K)$^{-1}$; T_{bat} corresponds to the absolute battery shell temperature in K; A_h corresponds to the Ah throughput of the battery; z is the power law coefficient, which is equal to 0.552. In this study, A_h is determined by the product of $I_{bat,RMS}$ and the total time of operation. It is assumed that the battery is operated for six hours, as shown in Figure 4.8, and is rested for 18 hours daily. The battery's end-of-life corresponds to 20% in capacity.

For each configuration, the RMS value of the battery current ($I_{bat,RMS}$), the final temperature ($T_{bat,SS}$), the average battery temperature ($T_{bat,avg}$), the total battery capacity loss $Q_{bat,loss}$ over the same period, and the corresponding theoretical battery lifespan are given in Table 4.5. The proposed plug-in SC module appears to increase the battery service life by 17.00% and 7.75% compared, respectively, to the BESS and the HESS controlled by the filter alone.

It is worthy recalling that the model adopted to estimate the battery lifespans in Table 4.5 does not account for certain factors that may influence the degradation rate. Besides the battery temperature, C-Rate, current intensity and duration, the actual battery lifespan is also affected by variables related to manufacturing (electrode defects, production variations), calendar ageing (storage temperature and SoC), environmental conditions (mechanical stress, humidity, ...), and battery component (separator, electrolyte, ...) [11]. Therefore, the estimated lifespans in Table 4.5 may differ depending on the battery degradation model adopted.

4.6.3 Scenario II: Controller performance under extreme ambient temperatures

4.6.3.1 Scenario II.a: Supercapacitor support under low temperature conditions

The performance of the proposed controller under low-temperature conditions are assessed in this section. To test it under extremely cold operating conditions, it is assumed that the energy storage system is operated at an ambient temperature of 5 °C. Figure 4.9 shows the current and temperature profiles of the battery-SC HESS. Here, the subscripts *w* and *wo* refer, respectively, to the performances obtained when considering and ignoring the battery temperature in the control scheme. The latter is obtained by assigning a constant temperature of 25 °C to the fuzzy input T_{bat}.

When operating the HESS in a cold environment to supply the load in Figure 4.9(a), the proposed controller tends to increase the battery current (cf. Figure 4.9(b)) by decreasing the share of slow varying current requested from SC (cf. Figure 4.9(c)). This causes an increase in battery heating by Joule's effect (cf. Figure 4.9(d)), which results in a faster rise of temperature aiming to get it as close as to the optimal range. Except for the supply of fast transitions by SC, battery current and temperature profiles appear identical to those obtained under the BESS. Compared to BESS and HESS,w/o configurations, Table 4.4 shows that the average deviation of the battery temperature (J_2) decreases, respectively, by 0% and 0.15% over the six minutes of operation under the new controller. The latter is accompanied by a 23.82% increase in the RMS value of I_{bat} (J_1), since battery warming turns out to be the main priority. A significant improvement of 99.07% is also observed in the deviation of SC SoC.

4.6.3.2 Scenario II.b: Supercapacitor support under high temperature conditions

The performance of the battery-SC HESS controller in a high-temperature environment is investigated in this section. To test it under extremely hot conditions, the HESS is assumed to be operated in an ambient temperature of 45 °C. The current and temperature profiles under the different configurations are presented in Figure 4.10.

When operating the battery-SC HESS under high ambient temperature conditions to supply the load in Figure 4.10(a), the proposed controller tends to decrease the battery current (cf. Figure 4.10(b))

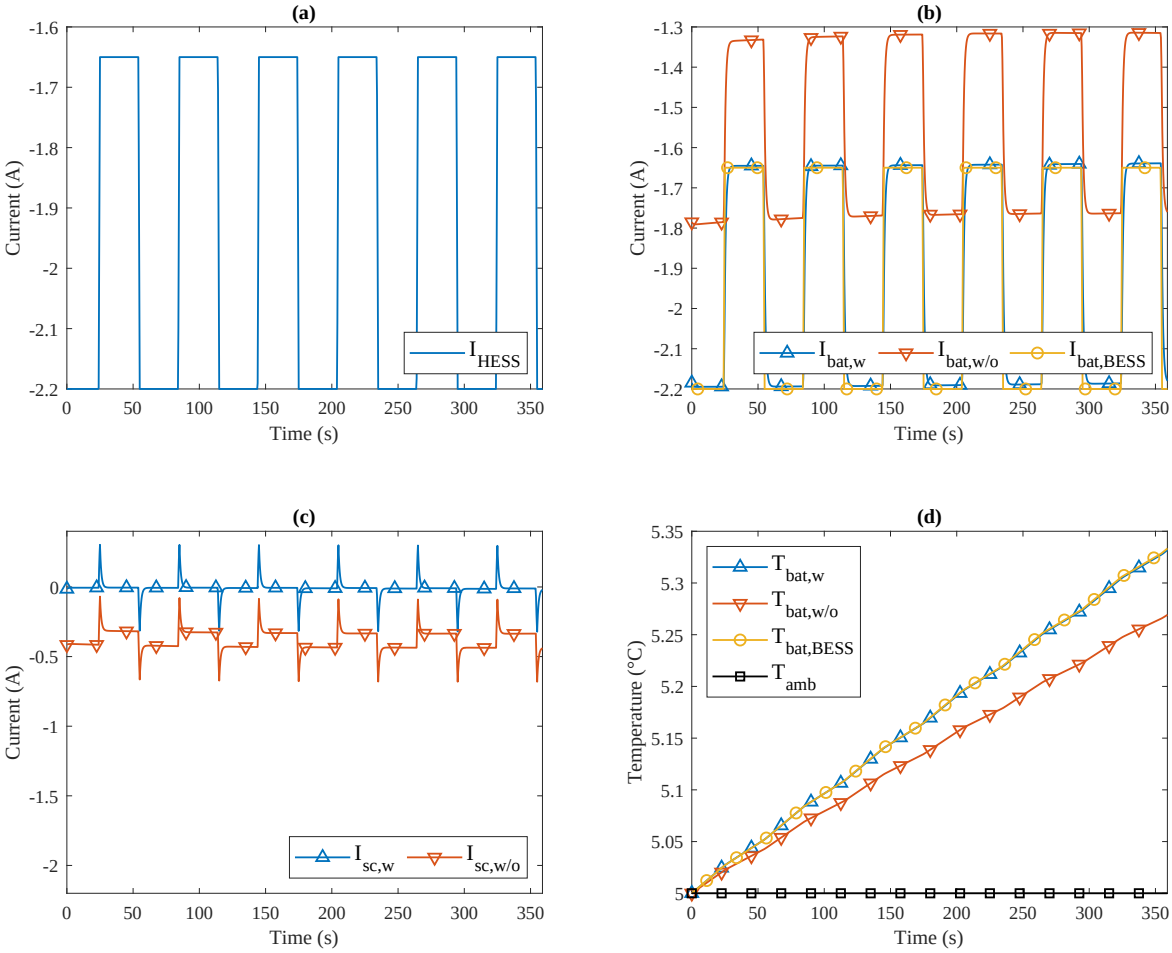

Figure 4.9. Current and temperature profiles under ambient temperature at 5 °C

by increasing the share of slow varying current handled by SC (cf. Figure 4.10(c)). Battery heating by Joule's effect is therefore reduced, which slows the temperature rise. In comparison to the BESS, Figure 4.10(d) shows that a 38.15% decrease in the battery temperature slope is achieved by the proposed controller. Moreover, Table 4.4 shows that, after operating for six minutes, 0.3% and 0.19% reduction in battery temperature deviation (J_2) compared respectively to BESS and w/o alternatives. This is accompanied by 38.95% and 23.87% reduction in the RMS value of I_{bat} (J_1). A degradation of 140% is also observed in the deviation of SC SoC.

4.7 CONCLUDING REMARKS

This paper has presented a fuzzy logic controller for plug-in SC modules retrofitted to a battery-alone storage system. Through adequate control, the SC contributes to the supply of both fast and slow

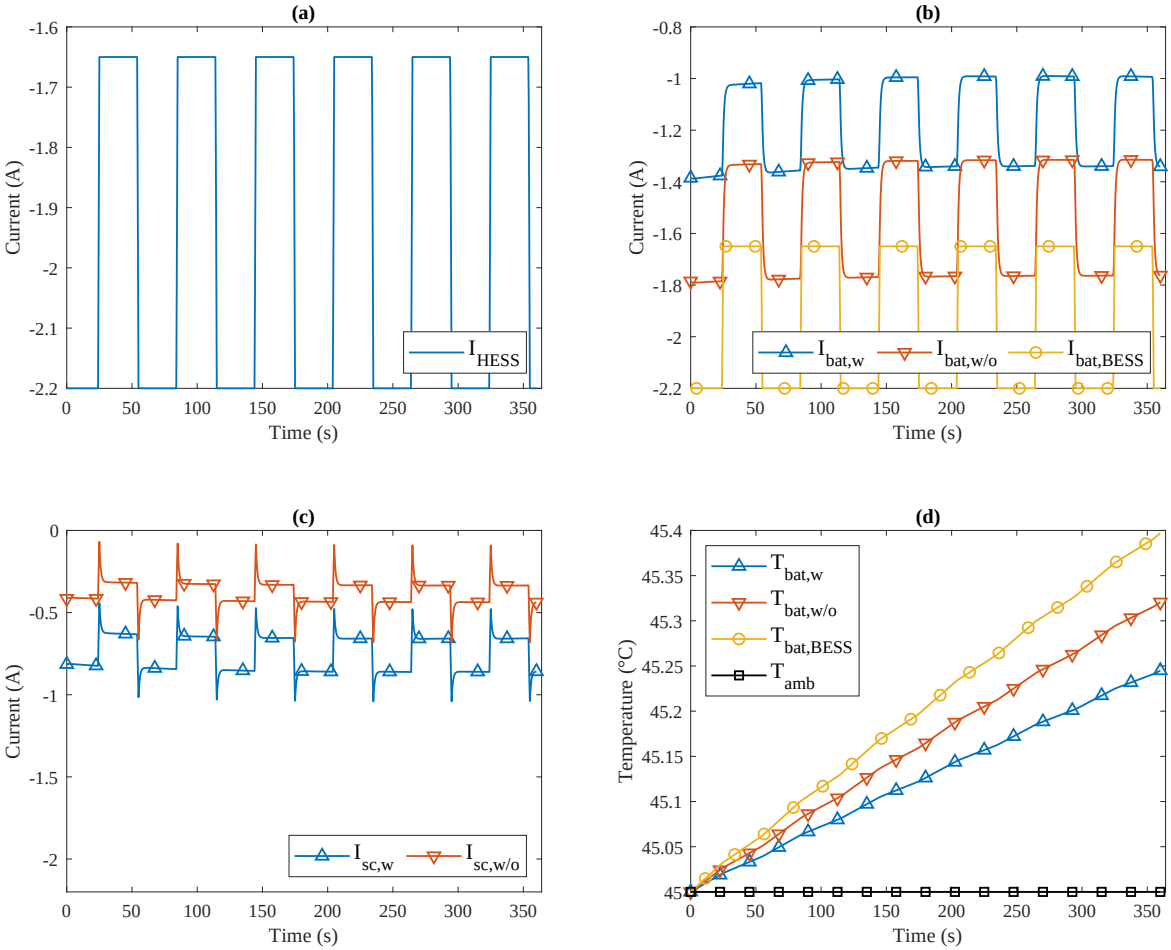

Figure 4.10. Current and temperature profiles under ambient temperature at 45 °C

varying currents. By doing so, the proposed EMS mitigates the electric and thermal stresses sustained by the battery, extending its lifespan as a result. The simulation study indicates a significant peak battery current decrease can be achieved under normal ambient conditions. A decrease in battery temperature slope can also be achieved in a high-temperature environment. The thermal support provided by the SC is gradually reduced when battery warm-up gains in priority. The proposed controller achieved better performance than the BESS counterpart. It also outperforms other battery-supercapacitor HESS controllers with regard to ease of implementation and comprehensive support to batteries.

CHAPTER 5 THERMAL MANAGEMENT OF HYBRID ENERGY STORAGE SYSTEMS BASED ON SPATIAL ARRANGEMENT

5.1 CHAPTER OVERVIEW

Temperature significantly impacts the performance and ageing of electrochemical storage, especially batteries. Therefore, it is critical to understand the thermal stress process to achieve better management. This chapter presents the preliminary findings about the thermoelectric management of batteries within a battery-supercapacitor (SC) hybrid energy storage system (HESS) using the spatial layout of storage cells. The structural arrangement is intended to benefit the cooling characteristics of battery cells through heat transfer with the nearby SC cells.

The content of the remaining sections is as follows. The thermoelectric model of a basic HESS is given in Section 5.2. Section 5.3 introduces the strategy adopted to carry out the thermal analysis. The case study is presented in Section 5.4. The simulation results are discussed in Section 5.5, followed by concluding remarks in Section 5.6.

5.2 THERMOELECTRIC MODELLING OF BATTERY-SC HESS

The layout diagram of an elementary battery-SC HESS consisting of a battery cell and an SC cell is shown in Figure 5.1. The thermoelectric models of these cells combine their respective electrical and thermal mathematical models.

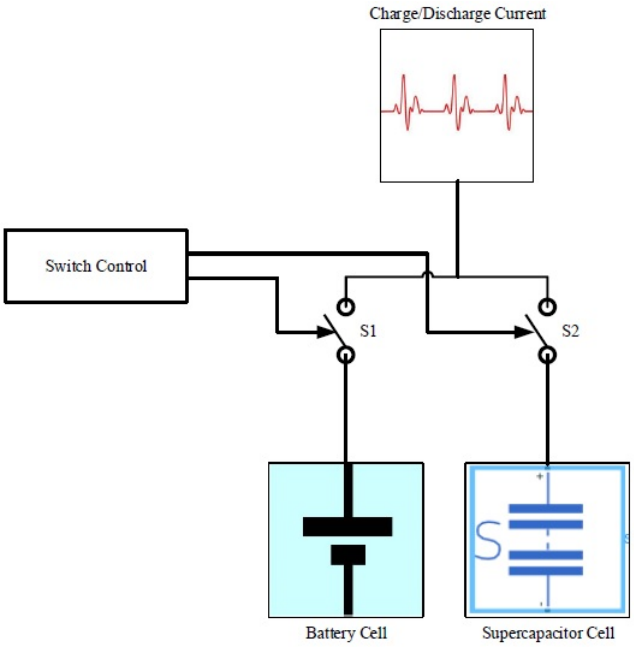

Figure 5.1. System layout diagram

5.2.1 Electrical modelling

Various electrical models of battery and SC have been investigated in the past. Among them, the second-order equivalent circuit models shown in Figure 5.2 are considered in this study, given their relative simplicity and acceptable accuracy with regard to the description of dynamic behaviours of HESS [97, 98, 99]. In Figure 5.2, R_{ser} and R_i denote the series resistance of SC and battery, respectively; C_{sc} denotes the SC capacitance; and OCV denotes the battery open-circuit-voltage, which varies as a function of its state of charge (SoC). The two RC networks are expected to capture both the short-term and long-term dynamics of energy storage (ES) devices.

5.2.2 Thermal modelling

The thermal model of the battery and SC is based on the “Law of conservation of energy”, which explains the temperature dynamics of a system using the heat generation model and a simple model of heat transfer inside and outside the system [97, 98, 100]. The total heat production combines the heat generation due to ohmic losses and entropy change, while the heat transfer can take place by conduction,

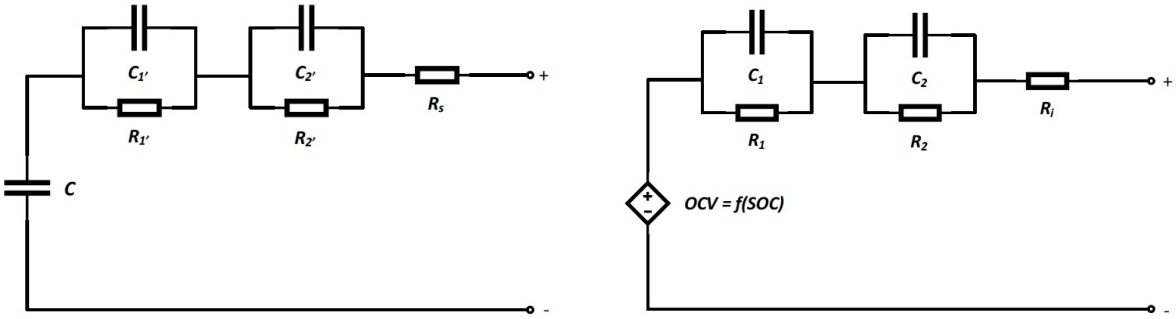

(a) Dynamic electric model of SC

(b) Second order equivalent circuit model of battery

Figure 5.2. Electric models of energy storage devices

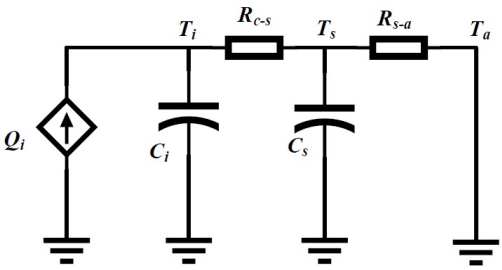

Figure 5.3. Thermal model of ES devices

convection and radiation phenomena. Considering the little quantity of heat generated by entropy change under a large load current, only the ohmic heat production is applied in this study.

Figure 5.3 presents the lumped parameter model that describes the battery and SC thermal behaviours assuming that: (1) heat production, heat transfer and temperature are uniformly distributed; (2) the core of the cell is made up of opaque material; (3) the convection inside the core is negligible [97, 98]. The model parameters consist of the ES internal and shell thermal capacitance, denoted by C_i and C_{sh}, respectively, and the thermal resistance between the ES core and shell, and between the ES shell and the ambience, denoted by R_{c-s} and R_{s-a} respectively. Q_i denotes the ES heat production; and T_a denotes the ambient temperature. T_i and T_{sh} denotes the ES internal and shell temperature, respectively. This is illustrated in the thermal equivalent circuit shown in Figure 5.3. This can also be expressed by

$$Q_i = C_i \frac{dT_i}{dt} + \frac{T_i - T_{sh}}{R_{c-s}}, \tag{5.1}$$

$$\frac{T_i - T_{sh}}{R_{c-s}} = C_{sh}\frac{dT_{sh}}{dt} + \frac{T_{sh} - T_a}{R_{s-a}}, \tag{5.2}$$

To study the effect of thermal interaction between the battery cell and the SC cell situated next to each other, as illustrated in Figure 5.4(a), the thermal model of the entire system is shown in Figure 5.4(b). Here, the subscripts b and s refer to the battery and SC, respectively. The thermal resistance R_{bs} materializes the existence of heat transfer between the battery and SC cell, where the flowing direction depends upon the temperature gradient between the cells.

The heat production corresponds to the total power dissipated in the battery and SC cells, which are expressed by:

$$Q_{ib} = (V_b - OCV)I_b, \tag{5.3}$$

$$Q_{is} = (V_{sc} - U_c)I_{sc}. \tag{5.4}$$

Here V_b and V_{sc} denote the battery and SC terminal voltages, respectively, U_c denotes the SC capacitance voltage, and I_b and I_{sc} denote the current circulating through the battery and SC, respectively.

5.3 THERMAL ANALYSIS STRATEGY

Assuming that the SC is fully charged at the outset and able to supply the discharge current for the entire simulation period, the variations of internal and shell temperatures of the battery and SC as a function of time are collected under the following operating conditions, which depend upon the position of switches:

- S1 = 1 and S2 = 0: the battery in stand-alone mode. The SC is disconnected.
- S1 = 0 and S2 = 1: the supercapacitor in stand-alone mode. The battery is disconnected.
- S1 = 1 and S2 = 1: the battery and SC operate in parallel mode.
- S1 and S2 are set sequentially to 1 and 0 or 0 and 1, respectively: the switching mode.

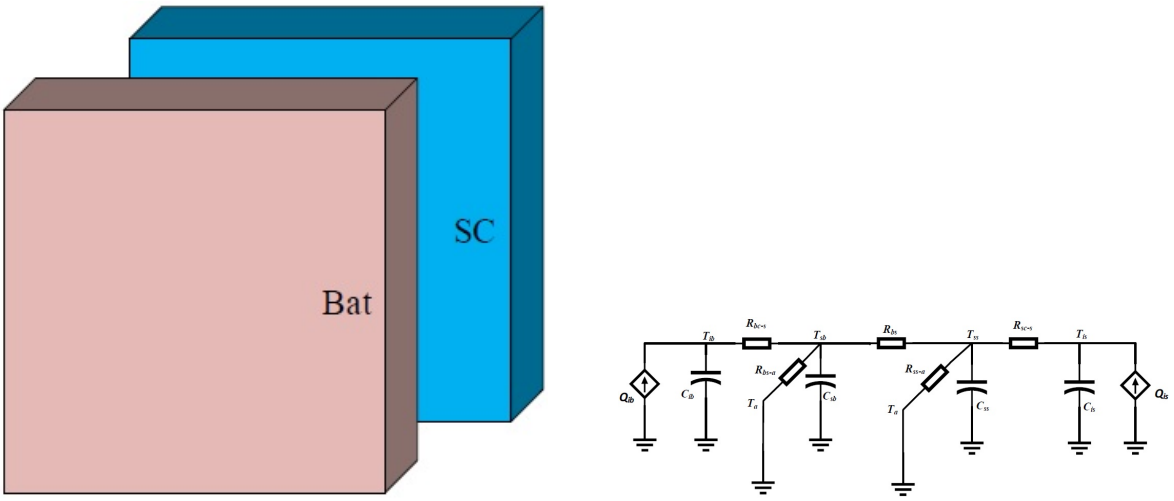

(a) Structural arrangement of ES devices

(b) Thermal model of HESS

Figure 5.4. Arrangement and thermal interaction of ES devices

During stand-alone and parallel modes, the thermal behaviours of ES devices are analysed when the two cells are relatively far from each other, i.e., $R_{bs} \rightarrow \infty$, and when they are relatively close to each other, $0<R_{bs}<\infty$.

The results obtained from the two scenarios are then compared to assess the influence of the spatial configuration of battery and SC cells on their temperature.

5.4 CASE STUDY

We consider a HESS consisting of a prismatic battery cell rated at 3.2V/30Ah, and a prismatic SC cell rated at 2.6V/3000F. The height, width and thickness of the two cells are 182, 100, and 32 mm, respectively [98]. The electrical and thermal characteristics of the battery are taken from the literature [98]. Those of the SC cell are also obtained from the literature [99, 101], respectively. These parameters are summarized in Table 5.2. The thermal resistance R_{bs} is determined using the thermal conductivity of ambient air, which is equal to 0.03 [101]. The space between the ES cells and their initial temperature are set to 1 mm and 20 °C, respectively. Figure 5.5(a) and Figure 5.5(b) show, respectively, the profile of charging/discharging current applied to the HESS and the operating sequence of battery and SC during the switching mode.

Table 5.2. Battery and SC parameters

Battery cell			Supercapacitor cell		
Parameter	Value	Unit	Parameter	Value	Unit
R_i	0.0135	Ω	R_{ser}	0.8216	mΩ
R_1	0.008	Ω	$R_{1'}$	0.3146	mΩ
C_1	1875	F	$C_{1'}$	627	F
R_2	0.006	Ω	$R_{2'}$	0.3883	mΩ
C_2	100000	F	$C_{2'}$	1843	F
C_{ib}	287.77	J/K	C_{is}	580	J/K
C_{sb}	30.8	J/K	C_{ss}	30.8	J/K
R_{bc-s}	0.5776	K/W	R_{sc-s}	2.6	K/W
R_{bs-a}	0.8333	K/W	R_{ss-a}	0.8333	K/W

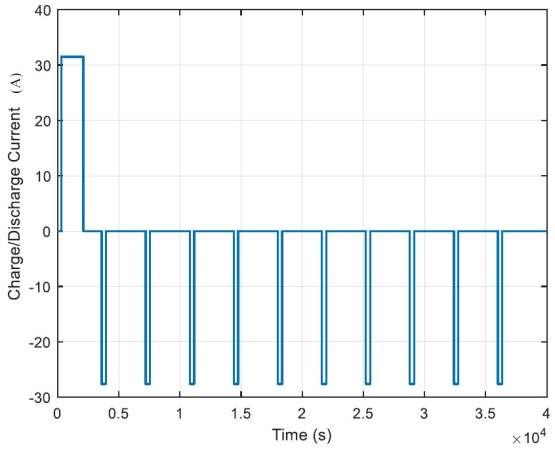

(a) Charging/Discharging current

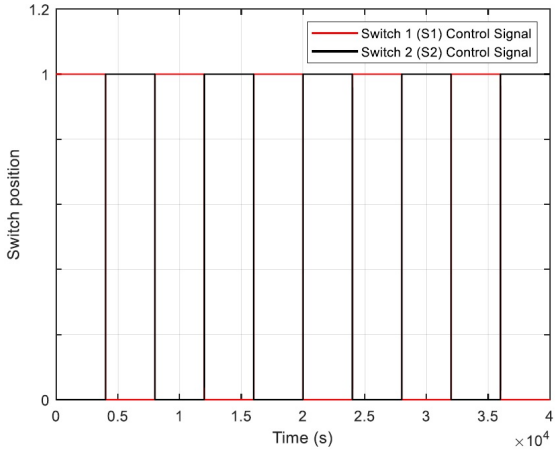

(b) Operating sequence of battery and SC under the switching mode

Figure 5.5. Load profile and switch commutation

5.5 SIMULATION RESULTS AND DISCUSSIONS

The thermal management strategy described earlier was implemented and simulated in an MATLAB/Simulink environment. Figure 5.6(a) presents the comparison of T_{ib} obtained under three modes: the standalone mode, the separate mode with thermal connection to SC, and the switching mode. It is found that the thermal connection allows heat transfer from the battery (hot body) to the SC (cold body), which reduces the battery's internal temperature. A similar trend is observed when comparing T_{sb} for the same three cases, as shown in Figure 5.6(b). It is noteworthy that the higher the temperature gradient between T_{ib} and T_{is} and the smaller the spacing between the cells, the greater the heat transferred from the battery to SC.

Figure 5.7(a) and Figure 5.7(b) show, respectively, T_{ib} and T_{sb} for three different distances between the cells. Figure 5.8(a) shows T_{is} and T_{ss} for SC in standalone mode in the absence of thermal connection with the battery and T_{is} in the switching mode. Under the last mode, an increase in T_{is} is observed during the operating periods of the battery because Q_{is} is zero in this case, and thus more heat is transferred from the battery to SC.

To illustrate the influence of the structural configuration of HESS when SC is used for filtering the load fluctuations, T_{ib} is obtained both in the absence and presence of a thermal connection between the

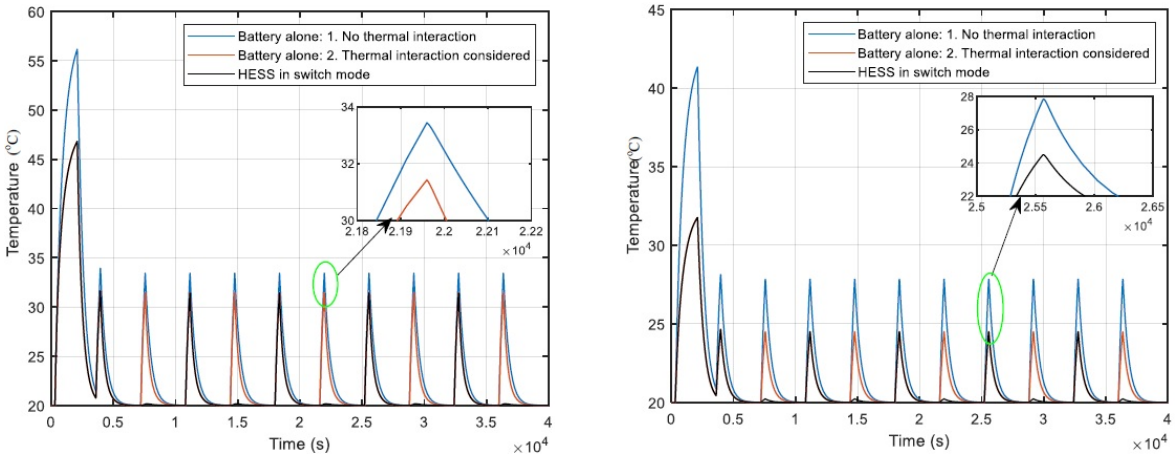

(a) Battery internal temperatures

(b) Battery shell temperatures

Figure 5.6. Battery temperatures with varying interactions between the EES

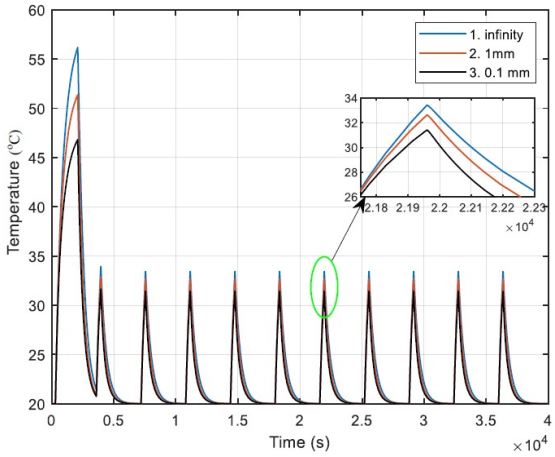

(a) Battery internal temperatures

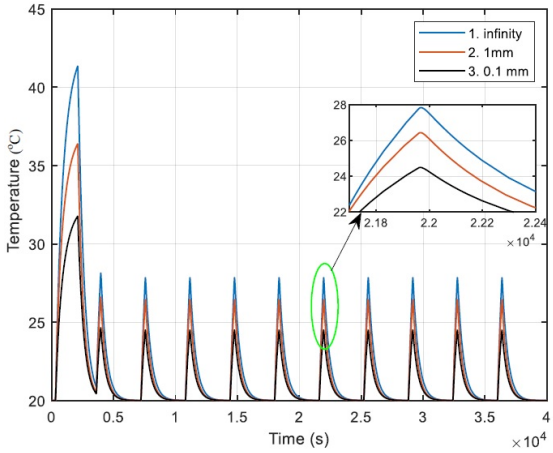

(b) Battery shell temperatures

Figure 5.7. Influence of the distance between the two cells

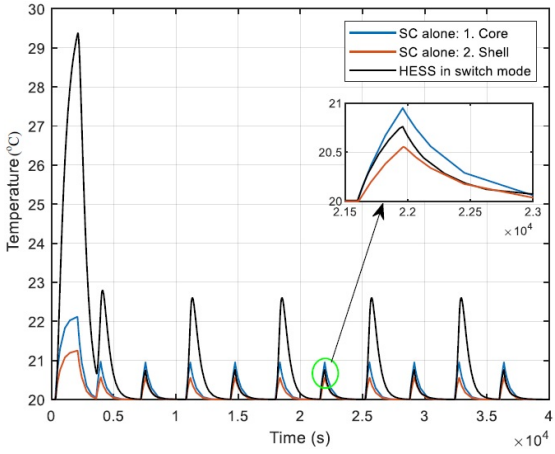

(a) SC internal temperature in switch mode and internal and shell temperatures in standalone mode

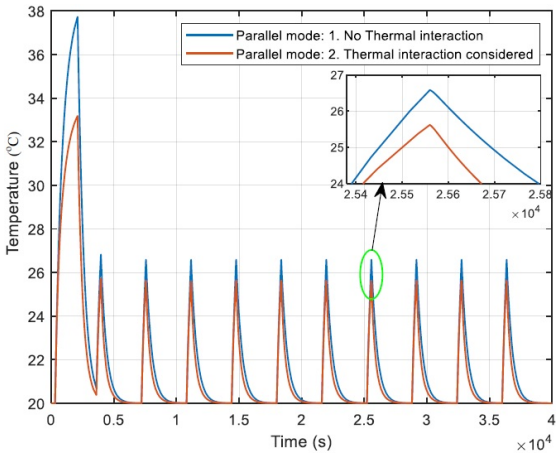

(b) Battery internal temperatures in parallel mode

Figure 5.8. SC temperatures (standalone) and battery temperature (parallel)

cells. It is observed that in addition to the decrease of T_{ib} due to the filtering action of SC, the spatial arrangement can also influence the reduction of T_{ib} as shown in Figure 5.8(b).

5.6 CONCLUDING REMARKS

Thermal management of a batter-SC HESS based on the spatial arrangement of the battery and SC cells was reported in this paper. It was found that the spatial configuration of the cells can influence the

thermal management of the battery and SC. It was also found that the higher the temperature gradient between the internal temperatures of cells and the smaller the spacing between them, the greater the heat transferred from one cell to the other. Accordingly, the spatial arrangement of ES cells can offer a passive assistance to the control strategy proposed in Chapter 4, which aims to help manage the battery temperature.

CHAPTER 6 ECONOMIC SIZING OF SUPERCAPACITORS FOR COST-EFFECTIVE HYBRIDIZATION OF BESS

6.1 CHAPTER OVERVIEW

This chapter presents a life cycle cost (LCC) optimization model for the cost-effective retrofit of battery-alone energy storage systems (BESS) with a supercapacitor. The proposed model can be used to judge the opportunity to implement a battery-SC HESS instead of a BESS in brownfield and greenfield projects.

This chapter is structured as follows. Section 6.2 deals with the modelling of energy storage (ES) devices. The techno-economic optimization model aimed for adequate sizing of SC is addressed in Section 6.3. The case study is introduced in Section 6.4. The presentation and discussion of simulation results are provided in Section 6.5. Concluding remarks are formulated in Section 6.6.

6.2 ENERGY STORAGE MODELLING

The layout of the power system investigated here is shown in Figure 6.1. The existing infrastructure consists of a BESS, power sources, electric loads, etc. The plug-in SC kit consists of SC cells/modules, a bidirectional DC/DC converter that interfaces the SC storage and an energy management system (EMS) responsible for implementing the optimal power split between the HESS components.

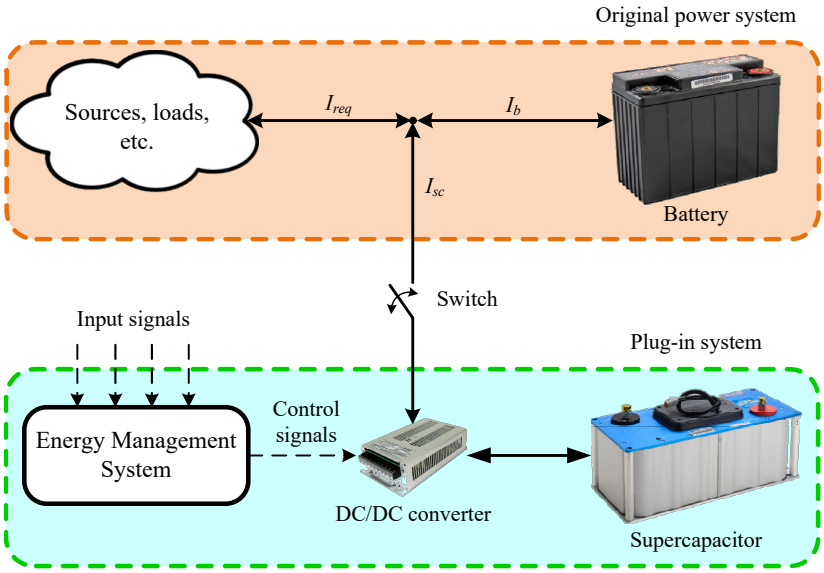

Figure 6.1. Layout of the battery-SC hybrid energy storage system

6.2.1 Battery modelling

Various battery models have been developed in the past to help predict its behaviour. Because of their ability to simulate the electrical performances of batteries with limited insights into electrochemical processes and the reasonable trade-off between speed and accuracy, the Equivalent Circuit Models (ECMs) are today among the most popular battery models.

Figure 6.2 shows the typical ECM battery models. The Internal Resistance Model, also known as the Rint model, in Figure 6.2a comprises an ideal voltage source simulating the open circuit voltage (OCV), and internal series resistance. While characterized by great simplicity, easy parameter measurement, and fast implementation and simulation, the Rint model suffers from two shortcomings: an infinite battery capacity and its validity is limited to the absence of dynamics in the load. To address the latter, a variant known as the Thevenin model, consists in adding an RC parallel network in series with the first two elements (Figure 6.2b). Finally, the RC model shown in Figure 6.2c comprises two RC series networks mounted in parallel and connected to a series resistance. Contrarily to the previous models, The RC model can capture the rate capacity, and charge recovery effects [102].

From an electrochemical perspective, R_0 in figs 6.2a to 6.2c denotes the battery's ohmic internal resistance, combining the electrolyte and electrode resistances [103]; $R_1 - C_1$ in Figure 6.2b mimics

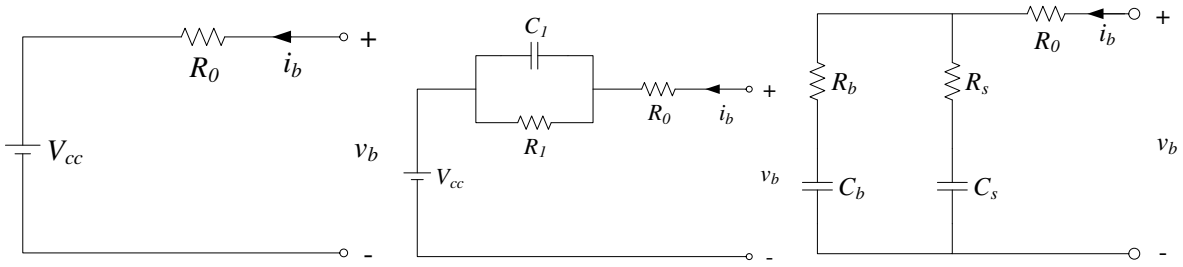

(a) Rint battery model (b) Thevenin model (c) RC model

Figure 6.2. Basic ECM-based models of batteries

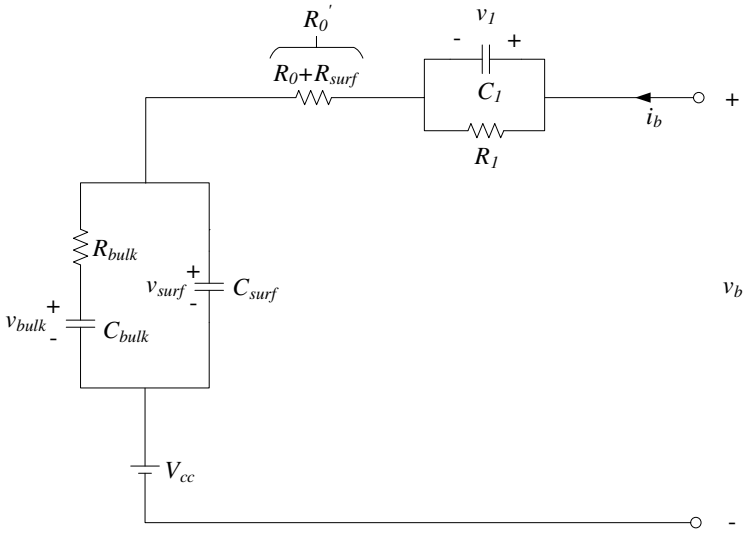

Figure 6.3. Proposed battery model

the voltage transients that result from the charge transfer on the electrode/electrolyte interface and the ion mass diffusion in the battery [104]; $R_b - C_b$ and $R_s - C_s$ in Figure 6.2c correspond, respectively, to the bulk inner part and the surface region of electrodes in contact with the electrolyte [102]. Further details on these ECM battery models is provided in the literature [105, 106].

This chapter proposes an ECM variant shown in Figure 6.3. Based on the previous models. This variant is expected to combine the strengths of both Thevenin and RC models, delivering more accurate predictions without requiring excessive computational burden. Based on the physical structure of electrodes, the surface region's resistance, denoted by R_{surf}, is relocated so that a portion of the energy flowing towards/from the bulk inner part is also dissipated at the surface.

The continuous-time domain state-space model of a battery cell/module modelled in Figure 6.3 is given by [107]

$$\dot{\mathbf{x}}_b = \mathbf{A}_b\mathbf{x}_b + \mathbf{B}_b\mathbf{u_b}, \tag{6.1}$$

$$\mathbf{y}_b = \mathbf{C}_b\mathbf{x}_b + \mathbf{D}_b\mathbf{u_b}, \tag{6.2}$$

where

$$\mathbf{x}_b = [v_{surf} \quad v_{bulk} \quad v_1]^T,$$

$$\mathbf{A}_b = \begin{bmatrix} -\frac{1}{R_{bulk}C_{surf}} & \frac{1}{R_{bulk}C_{surf}} & 0 \\ \frac{1}{R_{bulk}C_{bulk}} & -\frac{1}{R_{bulk}C_{bulk}} & 0 \\ 0 & 0 & -\frac{1}{R_1C_1} \end{bmatrix},$$

$$\mathbf{B}_b = \begin{bmatrix} \frac{N_{b,s}}{C_{surf}} & 0 \\ 0 & 0 \\ \frac{N_{b,s}}{C_1} & 0 \end{bmatrix},$$

$$\mathbf{u_b} = [i_b \quad V_{cc}]^T,$$

$$\mathbf{y}_b = v_b$$

$$\mathbf{C}_b = [1 \quad 0 \quad 1],$$

$$\mathbf{D}_b = [N_{b,s}R_0' \quad 1].$$

The model parameters in Figure 6.3 can be readily scaled to an arbitrary $N_{b,s}$-cell or -module string using the following relationships in [107]:

$$R_1 = N_{b,s}R_{1,u},$$

$$C_1 = C_{1,u}/N_{b,s},$$

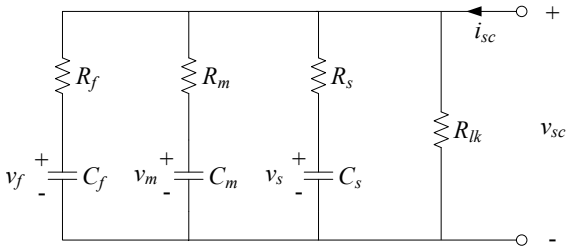

Figure 6.4. Supercapacitor three time constant equivalent circuit

$$R_0{}' = N_{b,s} R_{0,u}{}',$$

$$C_{surf} = C_{surf,u}/N_{b,s},$$

$$R_{bulk} = N_{b,s} R_{bulk,u},$$

$$C_{bulk} = C_{bulk,u}/N_{b,s}.$$

Here, the model parameters of a string and a cell/module are at the left and right sides of the equalities, respectively.

6.2.2 Supercapacitor modelling

The three time constant equivalent circuit shown in Figure 6.4 is adopted to model the supercapacitor [107, 108]. Here, R_s, C_s, R_f, C_f, R_m, and C_m correspond to the slow, medium, and fast branches' resistance and capacitance, respectively, and R_{lk} corresponds to a leakage resistance.

Assuming $N_{sc,s}$ cells or modules connected in series, the continuous-time domain state-space model of the supercapacitor model in Figure 6.4 is expressed as

$$\dot{\mathbf{x}}_{sc} = \mathbf{A}_{sc}\mathbf{x}_{sc} + \mathbf{B}_{sc}\mathbf{u}_{\mathbf{sc}}, \tag{6.3}$$

$$\mathbf{y}_{sc} = \mathbf{C}_{sc}\mathbf{x}_{sc} + \mathbf{D}_{sc}\mathbf{u}_{\mathbf{sc}}, \tag{6.4}$$

where

$$\mathbf{x}_{sc} = [v_s \quad v_m \quad v_f]^T,$$

$$\mathbf{A}_{sc} = \begin{bmatrix} -\frac{R_m R_f + R_f R_{lk} + R_m R_{lk}}{C_s P} & \frac{R_f R_{lk}}{C_s P} & \frac{R_m R_{lk}}{C_s P} \\ \frac{R_f R_{lk}}{C_m P} & -\frac{R_s Rf + R_f Rlk + R_s Rlk}{C_m P} & \frac{R_s R_{lk}}{C_m P} \\ \frac{R_m R_{lk}}{C_f P} & \frac{R_s R_{lk}}{C_f P} & -\frac{R_m Rs + R_s Rlk + R_m Rlk}{C_f P} \end{bmatrix},$$

$$\mathbf{B}_{sc} = \begin{bmatrix} \frac{R_f R_m R_{lk}}{C_s P} & \frac{R_s R_f R_{lk}}{C_m P} & \frac{R_m Rs R_{lk}}{C_f P} \end{bmatrix}^T,$$

$$\mathbf{u}_{sc} = i_{sc}$$

$$\mathbf{y}_{sc} = v_{sc}$$

$$\mathbf{C}_{sc} = \begin{bmatrix} \frac{R_x}{R_s} & \frac{R_x}{R_m} & \frac{R_x}{R_f} \end{bmatrix},$$

$$\mathbf{D}_{sc} = R_x,$$

$$P = R_s R_m R_f + R_{lk} R_m R_f + R_s R_{lk} R_f + R_m R_s R_{lk},$$

$$R_x = \left(\frac{1}{R_f} + \frac{1}{R_m} + \frac{1}{R_s} + \frac{1}{R_{lk}} \right)^{-1}.$$

The model parameters in Figure 6.4 can be readily scaled to an arbitrary $N_{sc,s}$-cell or -module string by means of the relationships below [107].

$$R_{lk} = N_{sc,s} R_{lk,u},$$

$$R_s = N_{sc,s} R_{s,u},$$

$$C_s = C_{s,u} / N_{sc,s},$$

$$R_m = N_{sc,s} R_{m,u},$$

$$C_m = C_{m,u} / N_{sc,s},$$

$$R_f = N_{sc,s} R_{f,u},$$

$$C_f = C_{f,u} / N_{sc,s},$$

with the model parameters of a full string and a single device (cell or module), respectively, at the left and right sides of the equalities. It is noteworthy to mention that the discrete forms of the above ES models will be obtained before the simulation study.

6.3 PROBLEM FORMULATION

Given an existing BESS that comprises $N_{b,s}$ cells or modules in series and $N_{b,p}$ strings in parallel, this section develops the optimization problem that helps find the SC size with the lowest life cycle cost (LCC) for the HESS over the remaining lifespan of the energy system. This optimization problem can be summarized as follows

$$\begin{aligned} \min_{I_{hess}} \quad & LCC(I_{hess}) \\ \text{s.t.} \quad & G(I_{hess}) = 0, \\ & H(I_{hess}) \geq 0, \\ & LB \leq I_{hess} \leq UB, \end{aligned} \tag{6.5}$$

where $I_{hess} = [N_{b,p}I_b; N_{sc,p}I_{sc}] = \left[N_{b,p} \times [I_b(1), I_b(2), \ldots, I_b(N)], N_{sc,p} \times [I_{sc}(1), I_{sc}(2), \ldots, I_{sc}(N)]\right]^T$ correspond to the array of the optimal battery and supercapacitor current profile over a cycle. Here $N_{sc,p}$ denotes the number of supercapacitor strings connected in parallel, $G(I_{hess})$ and $H(I_{hess})$ correspond, respectively, to the functions of equality and inequality constraints, LB and UB correspond, respectively, to the lower and upper bounds on X. The rest of this section develops each component of this optimization model.

6.3.1 Cost function

All the costs incurred throughout the battery-SC HESS lifespan can be classified into capital and operating costs, which are further detailed below.

6.3.1.1 Capital costs

The capital costs of the retrofitted battery-SC HESS comprise three components:

- The replacement cost of batteries.
- The initial and replacement costs of SC.
- The purchase cost of the SC's DC/DC converter.

a) Battery replacement cost

Let $L_{b,*}$ denote the expected lifespan of a battery pack, this quantity is expressed by

$$L_{b,*} = \frac{Q_{b,*} - Q_{b,EOL}}{Q_{b,loss}}. \tag{6.6}$$

Here $Q_{b,*}$ corresponds to the initial capacity of batteries, $Q_{b,EoL}$ corresponds to the end-of-life capacity, and $Q_{b,loss}$ corresponds to the daily capacity loss of batteries under specific operating conditions. $Q_{b,*}$ is equal to the remaining capacity of the current batteries at the time of decision-making about the energy storage upgrade. In the case of brand-new batteries, $Q_{b,*}$ is equal to their nominal capacity. As a rule of thumb, a battery reaches its end of life once the charging capacity falls below 80% of its rated capacity [109]. According to the literature, battery capacity fading results from two additive phenomena: calendar ageing and cycle ageing. The former expresses the capacity loss while resting (no current flowing). Cycling capacity loss refers to the degradation of battery performance while in use. $Q_{b,loss}$ is therefore given by

$$Q_{b,loss} = Q^{cal}_{b,loss} + Q^{cyc}_{b,loss}. \tag{6.7}$$

Here $Q^{cal}_{b,loss}$ and $Q^{cyc}_{b,loss}$ correspond, respectively, to the calendar-related capacity loss and cycle-related capacity loss.

Subject to the influence of the temperature and state-of-charge (SoC), capacity fading by calendar ageing is determined by [110, 111]

$$Q^{cal}_{b,loss} = B_{cal}(SoC_b)\exp\left(-\frac{Ea_{cal}}{R_g\theta}\right)t^{z_{cal}}. \tag{6.8}$$

Here B_{cal} is a pre-exponential factor that varies as a function of the battery SoC denoted by SoC_b, Ea_{cal} corresponds to the activation energy, R_g corresponds to the ideal gas constant, θ denotes the room temperature, z_{cal} is a dimensionless constant. At a time instant τ, the battery SoC is given by

$$SoC_b(\tau) = SoC_b(0) + \frac{\Delta T}{Q_{b,N}} \sum_{j=1}^{\tau} I_b(j), \tag{6.9}$$

with $SoC_b(0)$ the initial battery SoC at the time instant zero.

Subject to the influence of temperature and current intensity, capacity fading due to cycle ageing is expressed as [95]

$$Q_{b,loss}^{cyc} = \begin{cases} B_{cyc} \exp\left(\frac{-Ea_{cyc}}{R\theta}\right)(A_h)^{z_{cyc}}, & \text{if } I_b < C/2. \\ B_{cyc} \exp\left(\frac{-Ea_{cyc}+\alpha C_{rate}}{R_g\theta}\right)(A_h)^{z_{cyc}}, & \text{if } I_b > C/2, \end{cases} \tag{6.10}$$

with B_{cyc} a pre-exponential factor, Ea_{cyc} an activation energy for cycle ageing, α a coefficient for ageing acceleration due to current intensity, C_{rate} the charge/discharge rate, A_h the ampere-hour throughput, and z_{cyc} a dimensionless constant. Based on the optimal battery current profile obtained by solving (6.5), C_{rate} and A_h are expressed by [112, 91]

$$C_{rate} = I_{b,rms}/I_{b,1C}, \tag{6.11}$$

$$A_h = I_{b,rms} C_y N \Delta T/3600, \tag{6.12}$$

with $I_{b,rms}$ the root mean square (RMS) of the battery current, $I_{b,1C}$ the battery current that discharges it from full to empty in one hour (also referred to as "1C current"), ΔT the sampling interval, N the number of sampling intervals per cycle, and C_y the number of cycles per day. The RMS of the battery current is given by

$$I_{b,rms} = \sqrt{\frac{1}{N}(I_b^T I_b)}, \tag{6.13}$$

with $I_b = [I_b(1), I_b(2), \ldots, I_b(N)]^T$.

Let L_{plant} denote the remaining plant's lifespan. The number of battery replacements needed over this period is determined by

$$M_b = \left\lceil \frac{L_{plant} - L_{b,old}}{L_{b,new}} \right\rceil. \tag{6.14}$$

Here, $\lceil \cdot \rceil$ denotes the ceiling function, M_b denotes the number of battery replacements, and $L_{b,new}$ denotes the expected service life of brand new batteries. Based on the above, the net present value

(NPV) of the battery capital expenditures (CAPEX), i.e., the replacement costs over the remaining plant's lifespan, denoted by CC_b, is given by

$$CC_b = \sum_{n=1}^{M_b} p_{b,0} N_{b,p} N_{b,s} \left(\frac{1+\pi}{1+d} \right)^{k_b(n)}, \tag{6.15}$$

with $p_{b,0}$ the battery unit price at year 0 of the energy storage upgrade, π the average inflation rate, d denotes the discount rate, and $k_b(n)$ an exponent expressed follows

$$k_b(n) = \left\lfloor \frac{L_{b,old} + nL_{b,new}}{365} \right\rfloor,$$

where $\lfloor \cdot \rfloor$ is the floor function.

b) Initial and replacement cost of supercapacitors

Let L_{sc} denote the expected service life of a brand-new supercapacitor. This is quantity is expressed by [113, 114]

$$L_{sc} = L_{sc,N} \left(\frac{V_{sc,N}}{V_{sc}} \right)^{-n_1} 2^{\frac{\theta_{ref} - \theta}{n_2}}, \tag{6.16}$$

with V_{sc} the average voltage across the SC, and θ_{ref} the reference room temperature, $L_{sc,N}$ the rated lifespan when operated at the rated voltage $V_{sc,N}$ and at the reference room temperature θ_{ref}. V_{sc} is obtained from (6.4) after solving (6.3).

Assuming an upgrade from BESS into a battery-SC HESS is adopted by the stakeholders, let M_{sc} denote the number of SC packs needed over the remaining lifespan of the plant. This quantity is determined by

$$M_{sc} = \left\lceil \frac{L_{plant}}{L_{sc}} \right\rceil, \tag{6.17}$$

with L_{sc} obtained from (6.16). Given the above, the NPV of the SC CAPEX over the remaining plant's lifespan, denoted by CC_{sc}, is expressed by

$$CC_{sc} = \sum_{n=1}^{M_{sc}} p_{sc,0} N_{sc,p} N_{sc,s} \left(\frac{1+\pi}{1+d} \right)^{k_{sc}(n)}, \tag{6.18}$$

with $p_{sc,0}$ the SC unit price at year 0 of the energy storage upgrade, and $k_b(sc)$ an exponent expressed follows

$$k_{sc}(n) = \left\lfloor \frac{nL_{sc}}{365} \right\rfloor.$$

c) Initial costs of supercapacitor DC-DC converter

Let M_{c2} denote the number of DC-DC converters needed for the SC over the remaining plant's lifespan. This quantity is determined by

$$M_{c2} = \left\lceil \frac{L_{plant}}{L_{c2}} \right\rceil, \tag{6.19}$$

with L_{c2} the expected lifespan of the converter. Accordingly, the NPV of the CAPEX on the DC-DC converters is given by

$$CC_{c2} = \sum_{n=1}^{M_{c2}} p_{c2,0} P_{c2,N} \left(\frac{1+\pi}{1+d} \right)^{k_{c2}(n)}, \tag{6.20}$$

with CC_{c2} the NPV of the purchase cost of the SC DC-DC converter, $p_{c2,0}$ the unit price of DC-DC converters at year 0, and $P_{c2,N}$ the nominal power of the device, and $k_{c2}(n)$ an exponent expressed follows

$$k_{c2}(n) = \left\lfloor \frac{nL_{c2}}{365} \right\rfloor.$$

Let m_c denote the margin applied to the converter capacity concerning the peak power transited by the supercapacitor storage, $P_{c2,N}$ is therefore expressed by

$$P_{c2,N} = m_c N_{sc,p} N_{sc,s} V_{sc,N} \max(|I_{sc}|), \tag{6.21}$$

with $V_{sc,N}$ the nominal voltage of a supercapacitor cell/module.

6.3.1.2 Operating costs

Assuming a retrofit of the BESS into a battery-SC HESS, two categories of operating costs will be affected: (1) the electricity costs related to power losses and the running of the cooling system; (2) the maintenance costs related to the newly added equipment.

a) Electricity costs

Following the energy storage retrofit, variations in electricity costs may result from

- The power losses in the battery.
- The power losses in the SC.
- The power losses in the battery's DC-DC converter.
- The power losses in the SC's DC-DC converter.
- The power consumption by the cooling system.

Based on the battery model in Figure 6.3, the daily energy losses in the battery storage, denoted by $E_{b,loss}$, is given by

$$E_{b,loss} = N_{b,p} \sum_{j=1}^{N} \left[\frac{V_1^2(j)}{R_1} + R_0{}' I_b^2(j) + \frac{(V_{surf}(j) - V_{bulk}(j))^2}{R_{bulk}} \right] C_y \Delta T / 3600, \tag{6.22}$$

where V_{surf}, V_{bulk}, and V_1 are the states obtained by solving (6.1).

Considering the SC model in Figure 6.4, the daily energy losses in the SC storage, denoted by $E_{sc,loss}$ is given by

$$E_{sc,loss} = N_{sc,p} \sum_{j=1}^{N} \left[\frac{V_{sc}^2(j)}{R_{lk}} + \frac{(V_{sc}(j) - V_s(j))^2}{R_s} + \frac{(V_{sc}(j) - V_m(j))^2}{R_m} + \frac{(V_{sc}(j) - V_f(j))^2}{R_f} \right] C_y \Delta T / 3600, \tag{6.23}$$

where V_s, V_m, and V_f are the states obtained by solving (6.3).

The variation of the efficiency of a typical DC-DC converter as a function of the load is shown in Figure 6.5. Let $E_{c1,loss}$ denote the daily energy losses occurring in the battery's converter, this quantity is given by

$$E_{c1,loss} = C_y \Delta T / 3600 \sum_{j=1}^{N} \left(\frac{1}{\eta_{c1}(j)} - 1 \right) P_{c1,out}(j), \tag{6.24}$$

with $\eta_{c1}(j))$ the converter efficiency read on Figure 6.5 given the converter's power rating $P_{c1,N}$, and its output power $P_{c1,out}(j)$ determined as follows

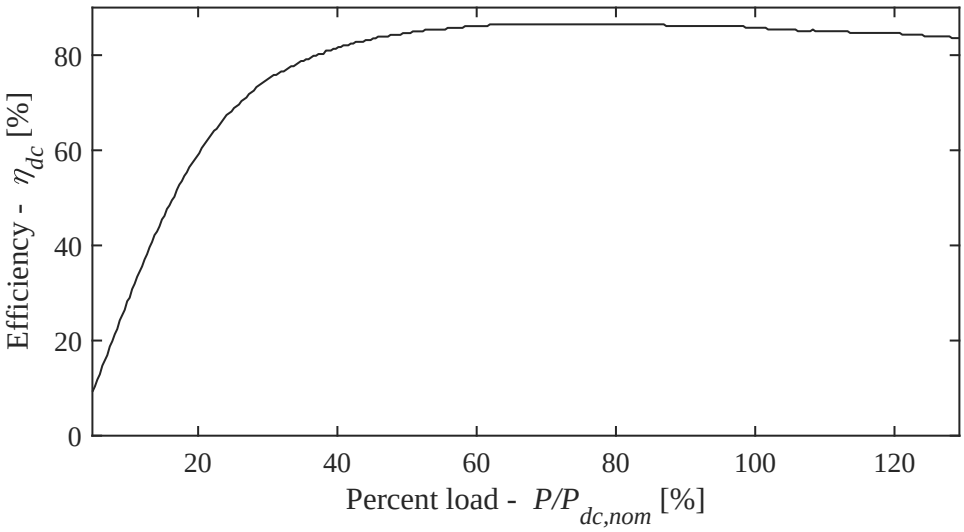

Figure 6.5. Generic conversion efficiency curve of DC-DC converters

$$P_{c1,out}(j) = \begin{cases} V_b(j)I_b(j), & \text{if } I_b(j) \geq 0, \\ |V_{bus}I_b(j)|, & \text{if } I_b(j) < 0, \end{cases} \tag{6.25}$$

with V_{bus} the voltage of the DC bus.

Similarly, let $E_{c2,loss}$ denote the daily energy losses occurring in the SC's converter. This quantity is expressed by

$$E_{c2,loss} = C_y \Delta T/3600 \sum_{j=1}^{N} \left(\frac{1}{\eta_{c2}(j)} - 1 \right) P_{c2,out}(j), \tag{6.26}$$

with $\eta_{c2}(j)$ the converter efficiency read on Figure 6.5 given the converter's power rating $P_{c2,N}$, and its output power $P_{c2,out}(j)$ determined as follows

$$P_{c2,out}(j) = \begin{cases} V_{sc}(j)I_{sc}(j), & \text{if } I_{sc}(j) \geq 0, \\ |V_b(j)I_{sc}(j)|, & \text{if } I_{sc}(j) < 0. \end{cases} \tag{6.27}$$

It is assumed that a heat ventilation and air conditioning (HVAC) system is operated to ensure the energy storage system and the other electrical equipment in the same room are maintained at the prescribed temperature of 25 $^\circ$ C. Let E_{hvac} denote the daily electricity consumption of the HVAC

system required to remove the heat dissipated by the battery, the SC, and their DC-DC converters. This quantity is expressed by

$$E_{hvac} = \frac{E_{b,loss} + E_{sc,loss} + E_{c1,loss} + E_{c2,loss}}{EER}, \tag{6.28}$$

with EER the energy efficiency ratio (cooling efficiency) of the HVAC system, and $E_{b,loss}$, $E_{sc,loss}$, $E_{c1,loss}$, and $E_{c2,loss}$ provided in (6.22), (6.23), (6.24), and (6.26), respectively.

b) Maintenance costs

Following the upgrade of the existing BESS into a HESS, additional expenses will be incurred to service the new equipment. Let $MC_{sc,0}$ and $MC_{c2,0}$ denote the yearly maintenance costs of the SC and its DC-DC converter, respectively, at year 0. These quantities are expressed by

$$MC_{sc,0} = m_{sc,0} E_{sc,N} N_{sc,p} N_{sc,s}, \tag{6.29}$$

$$MC_{c2,0} = m_{conv,0} P_{c2,N}, \tag{6.30}$$

with $E_{sc,N}$ the rated energy of each SC cell/module, and $m_{sc,0}$ and $m_{conv,0}$ the unit maintenance costs of the SC and its converter, respectively, at year 0.

6.3.1.3 Life cycle cost

Based on the above, the LCC of the battery-SC HESS can be expressed as [115]

$$LCC = CC + \sum_{j=1}^{L_{plant}} \frac{OC(j) + MC(j)}{(1+d)^j} - SV, \tag{6.31}$$

where CC corresponds to the NPV of the capital cost, $OC(j)$ and $MC(j)$ correspond, respectively, to the NPV of the total operating cost during the j-th year, and SV corresponds to the NPV of the total salvage value.

Following Section 6.3.1.1, CC is given by

$$CC = CC_b + CC_{sc} + CC_{c2}, \tag{6.32}$$

with CC_b, CC_{sc}, and CC_{c2} given by (6.15), (6.18), and (6.20), respectively.

As indicated earlier, the operating expenditures considered in this study are the electricity cost related to power losses in the energy storage and the DC-DC converters and their cooling by the HVAC system. The NPV of operating costs during the j-th year is given by

$$OC(j) = 365e_0(1+r)^j(E_{b,loss} + E_{sc,loss} + E_{c1,loss} + E_{c2,loss} + E_{hvac}), \tag{6.33}$$

with $E_{b,loss}$, $E_{sc,loss}$, $E_{c1,loss}$, $E_{c2,loss}$, and E_{hvac} are given by (6.22), (6.23), (6.24), (6.26), and (6.28), respectively. Here, e_0 corresponds to the electricity price at year 0 of the upgrade project, and r corresponds to the annual escalation rate of electricity price.

As indicated earlier, the maintenance cost in this study is limited to the additional expenditure induced by the upgrade activities. Accordingly, the NPV of maintenance cost during the j-th year can be calculated as

$$MC(j) = (1+\pi)^j(MC_{sc,0} + MC_{c2,0}). \tag{6.34}$$

Although efforts are made to promote circular business models in the battery sector, mainly through second-life applications and recycling at the end of the life cycle, the adoption remains marginal in practice. While little is currently known about the share of batteries repurposed for second-life energy storage, it is estimated that only 5% of rechargeable Li-ion batteries are recycled [116]. Thus, most batteries are disposed of in landfill sites. The same applies to lead-acid batteries and other chemistries wherever recycling facilities are not common, especially in developing countries [116]. Accordingly, no salvage value is assumed to be zero in this study. Based on the above, the LCC in (6.31) can be easily determined using (6.32), (6.33) and (6.34).

6.3.2 Constraints

The following constraints apply to the optimization problem summarized in (6.5)

- The power balance constraint.
- The bound constraints on the terminal voltages of the battery and SC.

- The bound constraints on the currents of the battery and SC.

Let I_{req} denote the current requested from the battery-SC HESS by the load, as shown in Figure 6.1. The power balance requirement is satisfied by the equality constraint below

$$I_b(j) + I_{sc}(j) = I_{req}(j), \tag{6.35}$$

for $j = 1, \ldots, N$.

Their respective terminal voltages are kept within specified limits to ensure safety and long service life to the HESS components.

$$V_b(j) \leq \overline{V_b}, \tag{6.36}$$

$$V_b(j) \geq \underline{V_b}, \tag{6.37}$$

$$V_{sc}(j) \leq \overline{V_{sc}}, \tag{6.38}$$

$$V_{sc}(j) \geq \underline{V_{sc}}, \tag{6.39}$$

for $j = 1, \ldots, N$. Here, $\overline{V_b}$, $\underline{V_b}$, $\overline{V_{sc}}$, and $\underline{V_{sc}}$ denote the maximum and minimum voltages applicable to the battery and SC respectively. $V_b(j)$ and $V_{sc}(j)$ are readily obtained from the discrete form of the output equations (6.2) and (6.4), respectively. These can be calculated after discretising the state equations (6.1) and (6.3), and determining the trajectories of the state variables.

The bound constraints on the decision variables, i.e., the battery and SC currents, are given by

$$I_b(j) \leq \overline{I_b}, \tag{6.40}$$

$$I_b(j) \geq \underline{I_b}, \tag{6.41}$$

$$I_{sc}(j) \leq \overline{I_{sc}}, \tag{6.42}$$

$$I_{sc}(j) \geq \underline{I_{sc}}, \tag{6.43}$$

for $j = 1, \ldots, N$. Here, $\overline{I_b}$, $\underline{I_b}$, $\overline{I_{sc}}$, and $\underline{I_{sc}}$ are the allowed maximum and minimum currents of the battery and SC, respectively.

Table 6.2. Datasheet-based energy storage parameters

Parameter	Value	Unit	Parameter	Value	Unit
`Battery cells` [92]			`Supercapacitor cells`[93]		
Rated capacity – $Q_{b,N}$	2.85	Ah	Rated capacity	2.5	F
Rated voltage – $V_{b,N}$	3.65	V	Equivalent series resistance (ESR)	85	mΩ
Standard charging current	1.375	A	Rated voltage – $V_{sc,N}$	5	V
Cut-off voltage	2.50	V	Maximum leakage current	8	μA
# in series – $N_{b,s}$	4		# in series – $N_{sc,s}$	2	
# in parallel – $N_{b,p}$	3				

6.4 CASE STUDY

To test the proposed SC sizing model, a BESS consisting of two strings of four 3.65V battery cells (Samsung INR18650-29E) is considered for upgrade into battery-SC HESS. The remaining capacity of these batteries is assumed to be 90% at the time of assessment, and the remaining plant's lifespan is 5 years. Given the rated voltage and capacity of the BESS, on the one hand, and the SC cells commercially available, on the other hand, the use of SC strings of 5V SC cells (Maxwell BMOD0002-P005-B02) will be applied. The ES parameters are presented in Table 6.2.

Based on Table 6.2 and the relationships in [107], the model parameters of SC cells are as follows: $R_{f,u}$=0.113 Ω, $C_{f,u}$=1.313 F, $R_{m,u}$=2.049×10^9 Ω, $C_{m,u}$=5.001×10^{-4} F, $R_{s,u}$=4.776×10^{10} Ω, $C_{s,u}$=0.012 F, and $R_{lk,u}$ = 1.250×10^6 Ω. The DC voltage is assumed to be stable at 12V. The economic parameters considered in this case study are given in Table 6.3.

6.5 SIMULATIONS AND DISCUSSION

6.5.1 Battery model evaluation

A battery cell was tested using the setup shown in Figure 6.6 to estimate the parameters of ECM battery models in Figures. 6.2 and 6.3. The cell was installed in a climatic chamber where the ambient temperature was regulated at 25 °C. A battery tester was used to cycle the cell by applying various

Table 6.3. Economic parameters of the simulation study

Parameter	Value	Unit
`General parameters`		
Annual inflation rate – π[117]	5.9	%
Discount rate – d [118]	4.4	%
Remaining plant's lifespan – L_{plant}	5	years
`Capital cost parameters`		
Remaining battery capacity at year 0 - $L_{b,0}$	90	%
Battery unit price at year 0 - $p_{b,0}$ [119]	7.74	USD
SC unit price at year 0 - $p_{sc,0}$[120]	8	USD
Unit price of DC-DC converter – $p_{c2,0}$ [121]	300	USD/kW
`Operating cost parameters`		
Electricity price at year 0 – e_0 [122]	0.092	USD/kWh
Annual escalation rate of electricity – r [123]	9.47	%
HVAC's energy efficiency ratio – EER [124]	2.5	
`Maintenance cost parameters`		
Unit maintenance cost of SC at year 0 – $m_{sc,0}$ [121]	5.55	USD/kWh
Unit maintenance cost of DC-DC converter at year 0 – $m_{c2,0}$ [121]	2	USD/kW

current profiles provided by a computer host. The latter also stored and displayed measurement data received from the battery tester and a temperature sensor.

The cell was subjected to variable current profiles shown in Figure 6.7(a) by scaling the Urban Dynamometer Driving Cycle (UDDS) profile obtained to span the ranges of 0 2.85A (1C) and 0 2.71A (0.95C). The model parameters were estimated using the former, while the validation was carried out using the latter.

Figure 6.7 presents the current and voltage profiles obtained at the validation stage. The result in Figure 6.7(b) indicates that the Rint model performs poorly in predicting the battery voltage.

Table 6.4 presents the errors and processing speed related to the different models. The latter refers to the average time necessary to complete the prediction of the cell voltage during the validation step. All

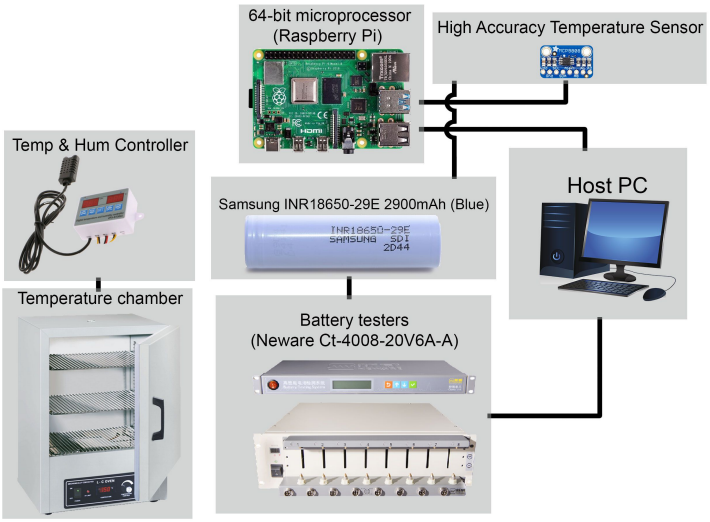

Figure 6.6. Schematic block diagram of the experimental setup

Table 6.4. Performances of ECM battery models

ECM model	Estimation RMSE (V)	Validation RMSE (V)	Computation time (sec.)
Rint	0.0532	0.0505	0.0355
RC	0.0043	0.0038	0.0389
Thevenin	0.0045	0.0049	0.0375
New ECM variant	0.0039	0.0034	0.0682

the model parameters were estimated, and the resulting models were validated using Simulink/Matlab 2019a installed in a PC i5-8500 CPU @ 3.00 GHz, 8.00 Gb of RAM capacity, running Windows 10. Based on Table 6.4, the RC and Rint models appear to be the most accurate and the fastest, respectively, amongst the common ECMs. It is also observed that the voltage prediction by the proposed ECM variant is 10.5% more accurate than the RC model but 1.75 times slower than it, the slowest of the popular ECMs. For a given application, the choice between the proposed ECM variant or a popular one will depend upon the accuracy requirements and the computation resources at disposal. It should be noted that some of the parameters of the ECMs adopted for the battery and SC are subject to variations as a function of temperature and/or SoC, resulting in model-plant mismatches (MPM) during operation. While robust controllers such as MPC may tolerate small MPM, increased MPM can deteriorate the control performance significantly, and even, in some cases, leading to shutdowns [83]. MPM is normally addressed by re-identification, which is beyond the scope of this study.

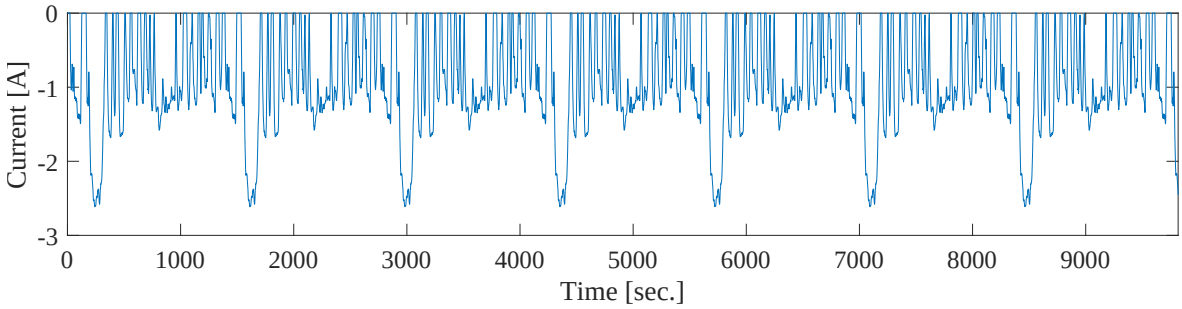

(a) Current profile applied to the battery cell

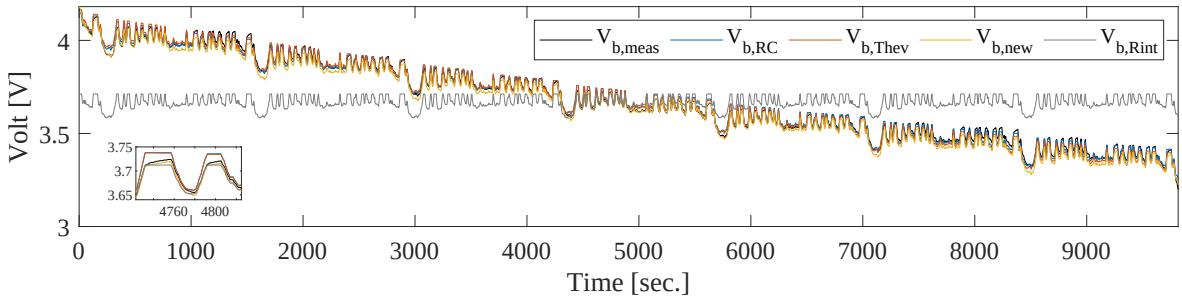

(b) Terminal voltages of the battery cell

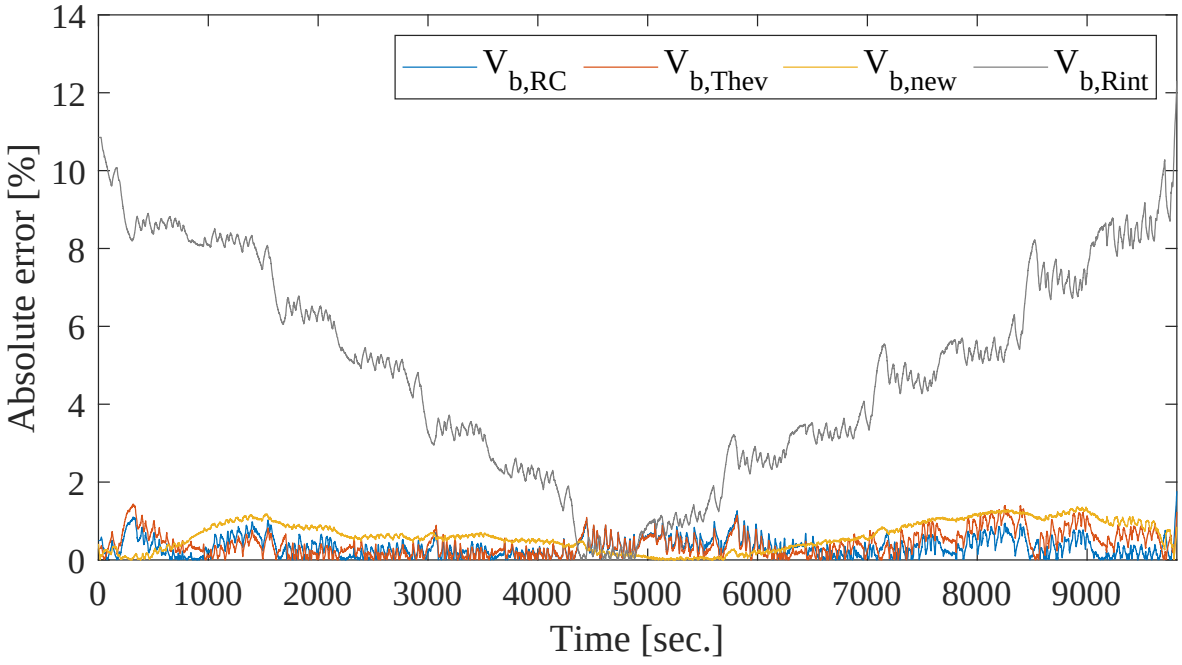

(c) Relative errors of the simulated battery voltages against the experiment results

Figure 6.7. Current profile and comparison between measured and simulated battery terminal voltages

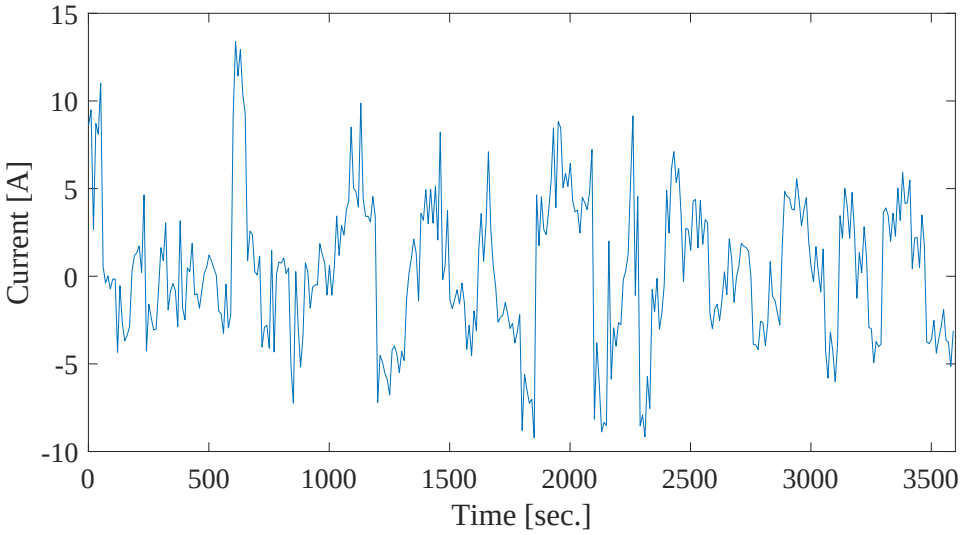

Figure 6.8. Current profile requested from the energy storage system

6.5.2 Energy storage upgrade analysis

Figure 6.8 shows the hourly current profile of the load as perceived by the energy storage system. With a sampling interval of ΔT equals 10 seconds, this load profile is assumed to repeat itself 24 times a day, i.e., Cy=24. Given the above, the bound limits and initial conditions are as follows: $V_{b,u,min}$=3V, $V_{b,u,max}$=3.65V, $V_{b,u}(0)$=3.325V, $\underline{I_b}$=-2.5A, $\overline{I_b}$=2.5A, $SoC_b(0)$=75%, $V_{sc,u,min}$=2.5V, $V_{sc,u,max}$=5V, $V_{sc,u}(0)$=3.75V, $\underline{I_b}$=-2.5A, and $\overline{I_b}$=2.5A.

Figures. 6.9 (a) and (b) present the RMS battery currents and the LCC related to the optimal solutions as a function of the number of SC strings mounted in parallel. Here, the plots labelled as "Battery current-based optimization" relates to the minimization of fluctuations in the battery current. In this context, the cost function is expressed as

$$J = \sum_{j=1}^{N-1} \left(I_b(j+1) - I_b(j)\right)^2 \tag{6.44}$$

It is observed that the greater the number of SC strings, the smoother the battery current, resulting in a lower RMS value as shown in Figure 6.9(a). From an economic viewpoint, the LCC improves simultaneously until a critical number of SC strings is reached. Beyond this point, the cost incurred

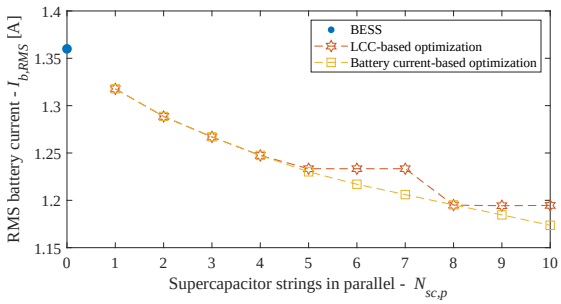

(a) RMS battery current vs # of SC strings

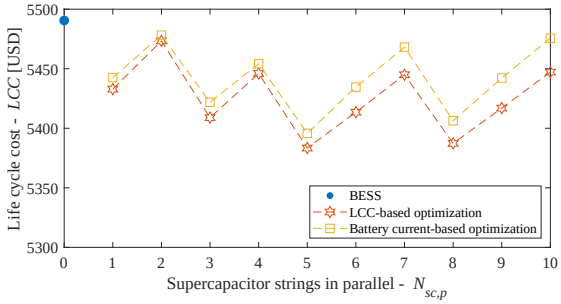

(b) LCC vs # of SC strings

Figure 6.9. RMS battery currents and LCC of optimal battery-SC HESS

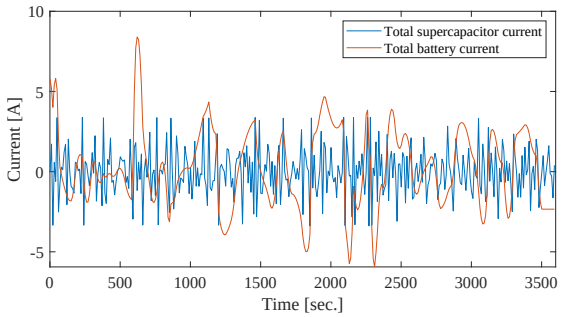

(a) Minimum battery current fluctuations

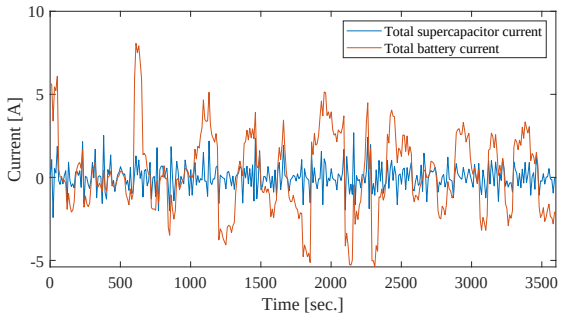

(b) Minimum overall LCC

Figure 6.10. Optimal battery and SC current profiles with $N_{sc,p} = 5$

to upgrade the BESS into a battery-SC HESS increases faster than the savings obtained through the reduction in battery replacement over the remaining lifespan of the plant.

The optimal current profiles in Figure 6.10(a) and (b) associated to $N_{sc,p} = 5$ indicate that sizing the SC to minimize fluctuations in the battery current also benefits the HESS's LCC, as depicted in Figure 6.9(b).

Table 6.5 presents the technical information related to the existing BESS and the most cost-effective HESS depending on the design criteria. Here, Design "D" corresponds to the HESS characterized by the lowest initial upgrade cost when the fluctuations in the battery current are minimized. Derived from [29], this intuitive sizing approach that focuses on capital expenditure at the outset is compared to the LCC-based model investigated in this research (Design "B"). The table shows that a single SC string is required for minimum initial cost while five strings should be mounted in parallel to

achieve the least LCC. The power rating of the SC's DC-DC converter is also increased by half when implementing the latter, while the service life of batteries is extended by 3.71%. This will result in two fewer battery replacements over the remaining lifespan of the power system. Compared to the existing BESS (Design "A"), the three retrofit strategies tend to positively affect the lifespan of batteries, with the best battery current-optimized HESS (Design "C") delivering similar technical performances to the best LCC-optimized HESS.

Table 6.5. Technical characteristics of the BESS and best cost-effective retrofit solutions

Design[(1)]	$N_{sc,p}$	SC's conv. power (W)	$I_{b,rms}$	Lifespan (days)			Nb of replacements[(2)]		
				Old batt.	New batt.	SC	Batt.	SC	SC's conv.
A	0	0.00	1.36	15.90	31.80	1534.78	57	0	0
B	5	36	1.23	16.78	33.56	1528.82	54	2	1
C	5	48	1.23	16.81	33.61	1419.84	54	2	1
D	1	24	1.32	16.18	32.36	1564.96	56	2	1

[(1)] A: BESS; B: LCC-based optimal HESS; C: Battery current-based optimal HESS; D: Least initial cost HESS

[(2)] Including the first SC and SC's DC-DC converter installed at time of upgrade.

The economic parameters of the BESS and the three HESS are presented in Table 6.6. It shows that the retrofit of BESS with SC cells following the LCC-based option (Design "B") will decrease by 1.95% the LCC of the HESS compared to that of the BESS. This savings is reduced at 1.73% when implementing a controller that minimizes the fluctuations in the battery current using the same number of SC cells (Design "C"). In comparison to the intuitive economic upgrade with a single string of SC (Design "D"), the LCC-based option (Design "B") further reduces the LCC of the ES plant by 1.08%.

In addition, Table 6.6 shows that the above savings result entirely from the reduction in battery replacement discussed earlier. Moreover, it is observed that the energy consumption associated with the HVAC operation and the power losses in the converters and ES devices contribute marginally to the LCC of battery-SC HESS, as it is less than 1%. Finally, since the economic viability of the proposed retrofit design depends on the costs incurred to replace worn batteries, this ES hybridization might turn out to be irrelevant under the following circumstances:

- Increase in battery lifespan or decrease in manufacturing cost induced by technology advancement.

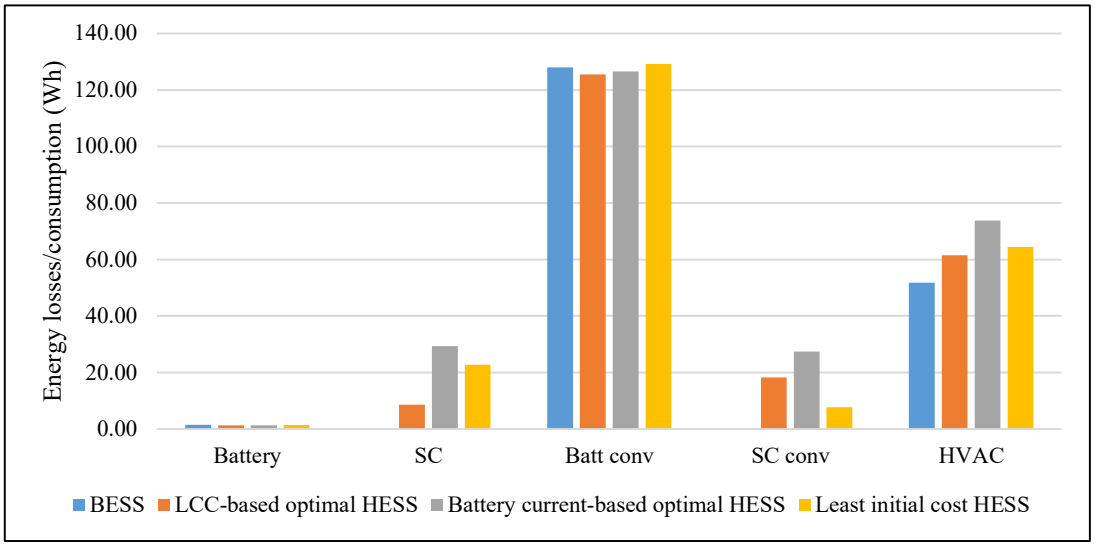

Figure 6.11. Energy consumption and losses related to ES systems

- Imbalance between supply and demand of batteries that results in a low selling price.
- Unfavourable operating conditions such as extended rest time, low current, etc.

Table 6.6. Economic information of the BESS and best cost-effective retrofit solutions

Design[(1)]	Inital cost (USD)		Capital cost NPV (USD)			O&M cost NPV (USD)			LCC
	SC	SC's conv.	Battery	SC	SC conv.	Energy	SC	SC conv.	(USD)
A	0.00	0.00	5455.34	0.00	0.00	35.19	0.00	0.00	5490.53
B	80.00	10.80	5165.85	164.70	10.80	41.72	0.00	0.32	5383.39
C	80.00	14.40	5167.54	163.50	14.80	50.14	0.00	0.42	5395.71
D	16.00	7.20	5358.40	32.94	7.20	43.75	0.00	0.21	5442.50

[(1)]A: BESS; B: LCC-based optimal HESS; C: Battery current-based optimal HESS; D: Least initial cost HESS

Figure 6.11 shows that the battery's DC-DC converter and the HVAC are respectively the first and second largest contributors to the energy consumption necessary to operate the BESS or any of the three optimal HESS. In addition, the proposed optimization model appears to be slightly more energy-efficient than the other two HESS alternatives.

6.6 CONCLUDING REMARKS

This paper reported on the economic retrofit of BESS with SC. An optimization model for cost-effective sizing of the SC and its DC/DC converter was investigated. This paper proved the critical need to rely on a life cycle cost evaluation for decision-making instead of focusing on the smoothing of battery current alone was demonstrated in this paper. While percentage-wise, expected cost savings in small systems may be negligible to justify such a modification, the proposed upgrade can be suitable for large energy systems. In this context, attention should be paid to determining factors such as the plant's remaining lifespan, the batteries' daily operating time, and the stress level sustained by the battery before the retrofit.

In addition, a new ECM variant for battery modelling was investigated in this chapter. Built upon the Thevenin and RC models, the proposed model delivers slightly more accurately than the others without excessively increasing computation resources.

CHAPTER 7 CONCLUSION

The research findings and perspective for future works are provided in this chapter.

7.1 RESEARCH FINDINGS

This thesis has reported on a study investigating strategies for the cost-effective upgrade of BESS into battery-SC HESS. In an attempt to address various gaps identified in the literature, two control strategies intended for the trouble-free upgrade of BESS into battery-SC HESS, a preliminary investigation on the impact of spatial arrangement on the thermal stress sustained by the battery and SC cells, and a model for optimal sizing of SC for cost-efffective retrofit of BESS have been investigated.

Primarily designed for hybrid renewable systems (HRS) originally equipped with BESS and controlled by a receding horizon control (RHC), the first control scheme consists in a hierarchical RHC of the SC-retrofitted HRS. Depending on the characteristics of the power management unit (PMU) running the previous RHC scheme, no or little modifications are required to integrate the SC into the existing infrastructure. Besides the decrease of electrical stress sustained by the battery, the proposed control framework also increases the amount of energy supplied by intermittent renewable and the power stability at the point of common coupling (PCC).

The second control model is built around a fuzzy logic controller unit to assist in retrofitting any BESS with SC. Thermoelectric management of batteries is successfully realized through sharing low-frequency current components between the two ES devices, besides the SC's full supply of high-frequency current components. Further extension in battery lifespan through this control scheme has been demonstrated.

The preliminary study conducted on the influence of spatial arrangement of battery-SC HEES cells on the thermal management of batteries demonstrates that the proximity between a battery cell and an SC cell can effectively contribute to the cooling process of batteries, thanks to the thermal interaction between them.

Finally, the thesis introduces a life cycle cost (LCC)-based optimization model that assists in properly sizing SC intended for retrofit in existing BESS. The possibility offered to stakeholders to take informed decisions about the economic opportunity of such an upgrade is also demonstrated.

7.2 FUTURE WORKS

While this thesis made significant steps towards extending the battery lifespan and improving the technical performances of renewable power systems through the retrofit of SC, it suffers from certain limitations as detailed below.

The impact of battery storage capacity loss over time, the efficiency variations of the converters with the load, and the possible model-plant mismatches have not considered in the hierarchical MPC model framework proposed in Chapter 3. In addition, the influence of a time-varying electricity tariff, such as time-of-use or critical peak pricing, on the power flow across the plant has not investigated in this work.

In chapter 4, one area of future work involves devising an adequate approach for sizing the supercapacitor and its DC/DC converter to maximize the economic benefit at the plant level. Assuming the sizing model proposed in Chapter 6 is adopted here, it will require to check whether the optimal sizes obtained under standard conditions are also suitable for extreme temperatures. Stability analysis is also required for the proposed fuzzy PI controller.

In practice, tens of battery and SC cells are combined to form HESS, instead of one cell of each type as discussed in Chapter 5. The thermal interaction between ES cells within such an environment needs to be investigated, including the influence of the cooling strategy applied and the geometric shapes of the cells.

In chapter 6, further investigations are required to develop a controller tuned to split power between the battery and SC following the profiles provided by the optimal sizing tool. Moreover, in practice, the inflation rate and the electricity price escalation rate usually vary yearly. The robustness of results obtained under fixed values, as considered in this study, needs therefore to be verified against reasonable fluctuations of the inflation rate and electricity price over the remaining lifespan of the plant.

REFERENCES

[1] U.S. Department of Energy, "Energy storage grand challenge: Energy storage market report [online]," Available: https://www.energy.gov/sites/prod/files/2020/12/f81/Energy%20Storage%20Market%20Report%202020_0.pdf, Accessed: Nov. 17, 2022.

[2] G. L. Soloveichik, "Battery technologies for large-scale stationary energy storage," *Annual Review of Chemical and Biomolecular Engineering*, vol. 2, pp. 503–527, 2011.

[3] J. Chang, J. Shang, Y. Sun, L. K. Ono, D. Wang, Z. Ma, Q. Huang, D. Chen, G. Liu, Y. Cui *et al.*, "Flexible and stable high-energy lithium-sulfur full batteries with only 100% oversized lithium," *Nature Communications*, vol. 9, no. 1, pp. 1–11, 2018.

[4] F. Nadeem, S. S. Hussain, P. K. Tiwari, A. K. Goswami, and T. S. Ustun, "Comparative review of energy storage systems, their roles, and impacts on future power systems," *IEEE Access*, vol. 7, pp. 4555–4585, 2018.

[5] K. Turcheniuk, D. Bondarev, G. G. Amatucci, and G. Yushin, "Battery materials for low-cost electric transportation," *Materials Today*, vol. 42, pp. 57–72, 2020.

[6] P. Ortega-Arriaga, O. Babacan, J. Nelson, and A. Gambhir, "Grid versus off-grid electricity access options: A review on the economic and environmental impacts," *Renewable and Sustainable Energy Reviews*, vol. 143, p. 110864, 2021.

[7] N. Kittner, F. Lill, and D. M. Kammen, "Energy storage deployment and innovation for the clean energy transition," *Nature Energy*, vol. 2, no. 9, p. 17125, 2017.

[8] A. Kumar, N. K. Meena, A. R. Singh, Y. Deng, X. He, R. Bansal, and P. Kumar, "Strategic integration of battery energy storage systems with the provision of distributed ancillary services in active distribution systems," *Applied Energy*, vol. 253, p. 113503, 2019.

[9] P. Haidl, A. Buchroithner, B. Schweighofer, M. Bader, and H. Wegleiter, "Lifetime analysis of energy storage systems for sustainable transportation," *Sustainability*, vol. 11, no. 23, p. 6731, 2019.

[10] M. R. Palacín and A. de Guibert, "Why do batteries fail?" *Science*, vol. 351, no. 6273, p. 1253292, 2016.

[11] N. Harting, R. Schenkendorf, N. Wolff, and U. Krewer, "State-of-health identification of lithium-ion batteries based on nonlinear frequency response analysis: First steps with machine learning," *Applied Sciences*, vol. 8, no. 5, p. 821, 2018.

[12] Sandia National Laboratories, "Cummulative Sum of Energy Storage Installations by Year [Online]," Available: https://sandia.gov/ess-ssl/gesdb/public/statistics.html, Accessed: Nov. 16, 2022.

[13] R. Hemmati and H. Saboori, "Emergence of hybrid energy storage systems in renewable energy and transport applications–a review," *Renewable and Sustainable Energy Reviews*, vol. 65, pp. 11–23, 2016.

[14] S. Hajiaghasi, A. Salemnia, and M. Hamzeh, "Hybrid energy storage system for microgrids applications: A review," *Journal of Energy Storage*, vol. 21, pp. 543–570, 2019.

[15] V. Aravindan, J. Gnanaraj, Y.-S. Lee, and S. Madhavi, "Insertion-type electrodes for nonaqueous li-ion capacitors," *Chemical Reviews*, vol. 114, no. 23, pp. 11 619–11 635, 2014.

[16] A. Z. A. Shaqsi, K. Sopian, and A. Al-Hinai, "Review of energy storage services, applications, limitations, and benefits," *Energy Reports*, vol. 6, pp. 288–306, 2020.

[17] National Aeronautics and Space Administration (NASA), "State-of-the-Art of Small Spacecraft Technology [Online]," Available: https://www.nasa.gov/smallsat-institute/sst-soa/power/, Accessed: Nov. 17, 2022.

[18] W. Jing, C. H. Lai, D. K. Ling, W. S. Wong, and M. D. Wong, "Battery lifetime enhancement via smart hybrid energy storage plug-in module in standalone photovoltaic power system," *Journal of Energy Storage*, vol. 21, pp. 586–598, 2019.

[19] M. Sellali, S. Abdeddaim, A. Betka, A. Djerdir, S. Drid, and M. Tiar, "Fuzzy-super twisting control implementation of battery/super capacitor for electric vehicles," *ISA Transactions*, vol. 95, pp. 243–253, 2019.

[20] Z. Bai, Z. Yan, X. Wu, J. Xu, and B. Cao, "H∞ control for battery/supercapacitor hybrid energy storage system used in electric vehicles," *International Journal of Automotive Technology*, vol. 20, no. 6, pp. 1287–1296, 2019.

[21] M. S. Masaki, L. Zhang, and X. Xia, "Hierarchical power flow control of a grid-tied photovoltaic plant using a battery-supercapacitor energy storage system," *Energy Procedia*, vol. 145, pp. 32–37, 2018.

[22] V. Herrera, A. Milo, H. Gaztañaga, I. Etxeberria-Otadui, I. Villarreal, and H. Camblong, "Adaptive energy management strategy and optimal sizing applied on a battery-supercapacitor based tramway," *Applied Energy*, vol. 169, pp. 831–845, 2016.

[23] J. Faria, J. Pombo, M. d. R. Calado, and S. Mariano, "Power management control strategy based on artificial neural networks for standalone pv applications with a hybrid energy storage system," *Energies*, vol. 12, no. 5, p. 902, 2019.

[24] International Energy Agency, "Technology mix in storage installations excluding pumped hydro, 2011-2016 [Online]," Available: https://www.iea.org/data-and-statistics/charts/technology-mix-in-storage-installations-excluding-pumped-hydro-2011-2016, Accessed: Aug. 06, 2021.

[25] ——, "Energy Storage [Online]," Available: https://www.iea.org/reports/energy-storage, Accessed: Aug. 06, 2021.

[26] International Renewable Energy Agency, "Innovation landscape brief: Utility-scale batteries," 2019.

[27] T. Mesbahi, F. Khenfri, N. Rizoug, P. Bartholomeüs, and P. Le Moigne, "Combined optimal sizing and control of li-ion battery/supercapacitor embedded power supply using hybrid particle swarm–nelder–mead algorithm," *IEEE Transactions on Sustainable Energy*, vol. 8, no. 1, pp. 59–73, 2016.

[28] A. Abdelkader, A. Rabeh, D. M. Ali, and J. Mohamed, "Multi-objective genetic algorithm based sizing optimization of a stand-alone wind/pv power supply system with enhanced battery/supercapacitor hybrid energy storage," *Energy*, vol. 163, pp. 351–363, 2018.

[29] L. Sun, P. Walker, K. Feng, and N. Zhang, "Multi-objective component sizing for a battery-supercapacitor power supply considering the use of a power converter," *Energy*, vol. 142, pp. 436–446, 2018.

[30] S. A. N'guessan, K. S. Agbli, S. Fofana, and D. Hissel, "Optimal sizing of a wind, fuel cell, electrolyzer, battery and supercapacitor system for off-grid applications," *International Journal of Hydrogen Energy*, vol. 45, no. 8, pp. 5512–5525, 2020.

[31] H. Chen, Z. Zhang, C. Guan, and H. Gao, "Optimization of sizing and frequency control in battery/supercapacitor hybrid energy storage system for fuel cell ship," *Energy*, vol. 197, p. 117285, 2020.

[32] Z. Wu, H. Tazvinga, and X. Xia, "Demand side management of photovoltaic-battery hybrid system," *Applied Energy*, vol. 148, pp. 294–304, 2015.

[33] B. Zhu, H. Tazvinga, and X. Xia, "Switched model predictive control for energy dispatching of a photovoltaic-diesel-battery hybrid power system," *IEEE Transactions on Control Systems Technology*, vol. 23, no. 3, pp. 1229–1236, 2015.

[34] Y. Riffonneau, S. Bacha, F. Barruel, S. Ploix *et al.*, "Optimal power flow management for grid connected PV systems with batteries," *IEEE Transactions on Sustainable Energy*, vol. 2, no. 3, pp. 309–320, 2011.

[35] J. Hu, Y. Xu, K. W. Cheng, and J. M. Guerrero, "A model predictive control strategy of pv-battery microgrid under variable power generations and load conditions," *Applied Energy*, vol. 221, pp. 195–203, 2018.

[36] M.-E. Choi, S.-W. Kim, and S.-W. Seo, "Energy management optimization in a battery/supercapacitor hybrid energy storage system," *IEEE Transactions on Smart Grid*, vol. 3, no. 1, pp. 463–472, 2012.

[37] D. Linden, *Handbok of Batteries*. McGraw-Hill, NY, 1994.

[38] S. Pay and Y. Baghzouz, "Effectiveness of battery-supercapacitor combination in electric vehicles," in *Power Tech Conference Proceedings, 2003 IEEE Bologna*, vol. 3. IEEE, Bologna, Italy, Jun. 23–26, 2003, pp. 6–pp.

[39] National Energy Regulator of South Africa, "Grid connection code for renewable power plants (RPPs) connected to the electricity transmission system (TS) or the distribution system (DS) in South Africa (July 2016)," Available: http://www.nersa.org.za/Admin/Document/Editor/file/Electricity/TechnicalStandards/Newable%20Energy/SAGC%20Requirements%20for%20Renewable%20Power%20Plants%20Rev%202%209.pdf, Accessed: Aug. 01, 2018.

[40] G. Wang, M. Ciobotaru, and V. G. Agelidis, "Power smoothing of large solar pv plant using hybrid energy storage," *IEEE Transactions on Sustainable Energy*, vol. 5, no. 3, pp. 834–842, 2014.

[41] L. Feng, J. Zhang, G. Li, and B. Zhang, "Cost reduction of a hybrid energy storage system considering correlation between wind and PV power," *Protection and Control of Modern Power Systems*, vol. 1, no. 1, pp. 1–9, 2016.

[42] J. Li, Y. Xue, L. Tian, and X. Yuan, "Research on optimal configuration strategy of energy storage capacity in grid-connected microgrid," *Protection and Control of Modern Power Systems*, vol. 2, no. 1, pp. 1–7, 2017.

[43] M. Ding, B. Wang, Z. Chen, Z. Chen, Y. Luo, and G. Zheng, "Stabilizing control strategy of complementary energy storage in renewable energy system," in *Innovative Smart Grid Technologies-Asia (ISGT Asia), 2012 IEEE.* IEEE, Tianjin, China, May 21–24, 2012, pp. 1–5.

[44] W. Zuo, R. Li, C. Zhou, Y. Li, J. Xia, and J. Liu, "Battery-supercapacitor hybrid devices: Recent progress and future prospects," *Advanced Science*, vol. 4, no. 7, p. 1600539, 2017.

[45] R. A. Dougal, S. Liu, and R. E. White, "Power and life extension of battery-ultracapacitor hybrids," *IEEE Transactions on Components and Packaging Technologies*, vol. 25, no. 1, pp. 120–131, 2002.

[46] T. Ma, H. Yang, and L. Lu, "Development of hybrid battery–supercapacitor energy storage for remote area renewable energy systems," *Applied Energy*, vol. 153, pp. 56–62, 2015.

[47] N. R. Tummuru, M. K. Mishra, and S. Srinivas, "Dynamic energy management of hybrid energy storage system with high-gain PV converter," *IEEE Transactions on Energy Conversion*, vol. 30, no. 1, pp. 150–160, 2015.

[48] B. Hredzak, V. G. Agelidis, and M. Jang, "A model predictive control system for a hybrid battery-ultracapacitor power source," *IEEE Transactions on Power Electronics*, vol. 29, no. 3, pp. 1469–1479, 2014.

[49] C. Xiang, Y. Wang, S. Hu, and W. Wang, "A new topology and control strategy for a hybrid battery-ultracapacitor energy storage system," *Energies*, vol. 7, no. 5, pp. 2874–2896, 2014.

[50] S. K. Kollimalla, A. Ukil, H. Gooi, U. Manandhar, and N. R. Tummuru, "Optimization of charge/discharge rates of a battery using a two-stage rate-limit control," *IEEE Transactions on Sustainable Energy*, vol. 8, no. 2, pp. 516–529, 2017.

[51] G. Wang, M. Ciobotaru, and V. G. Agelidis, "Power management for improved dispatch of utility-scale pv plants," *IEEE Transactions on Power Systems*, vol. 31, no. 3, pp. 2297–2306, 2016.

[52] X. Han, F. Chen, X. Cui, Y. Li, and X. Li, "A power smoothing control strategy and optimized allocation of battery capacity based on hybrid storage energy technology," *Energies*, vol. 5, no. 5, pp. 1593–1612, 2012.

[53] A. Parwal, M. Fregelius, I. Temiz, M. Göteman, J. G. de Oliveira, C. Boström, and M. Leijon, "Energy management for a grid-connected wave energy park through a hybrid energy storage system," *Applied Energy*, vol. 231, pp. 399–411, 2018.

[54] P. Roncero-Sánchez, A. Parreño Torres, and J. Vázquez, "Control scheme of a concentration photovoltaic plant with a hybrid energy storage system connected to the grid," *Energies*, vol. 11, no. 2, p. 301, 2018.

[55] C. Ye, S. Miao, Q. Lei, and Y. Li, "Dynamic energy management of hybrid energy storage systems with a hierarchical structure," *Energies*, vol. 9, no. 6, p. 395, 2016.

[56] N. R. Tummuru, M. K. Mishra, and S. Srinivas, "Dynamic energy management of renewable grid integrated hybrid energy storage system," *IEEE Transactions on Industrial Electronics*, vol. 62, no. 12, pp. 7728–7737, 2015.

[57] S. Kotra and M. K. Mishra, "A supervisory power management system for a hybrid microgrid with hess," *IEEE Transactions on Industrial Electronics*, vol. 64, no. 5, pp. 3640–3649, 2017.

[58] A. Aktas, K. Erhan, S. Özdemir, and E. Özdemir, "Dynamic energy management for photovoltaic power system including hybrid energy storage in smart grid applications," *Energy*, vol. 162, pp. 72–82, 2018.

[59] U. Manandhar, A. Ukil, G. H. Beng, N. R. Tummuru, S. K. Kollimalla, B. Wang, and K. Chaudhari, "Energy management and control for grid connected hybrid energy storage system under different operating modes," *IEEE Transactions on Smart Grid*, 2017.

[60] W. Jing, D. K. Ling, C. H. Lai, W. S. Wong, and M. D. Wong, "Hybrid energy storage retrofit for standalone photovoltaic-battery residential energy system," in *Innovative Smart Grid Technologies-Asia (ISGT-Asia), 2017 IEEE*. IEEE, Auckland, New Zealand, Dec. 4–7, 2017, pp. 1–6.

[61] A. A. Pesaran, S. Santhanagopalan, and G.-H. Kim, "Addressing the impact of temperature extremes on large format li-ion batteries for vehicle applications (presentation)," National Renewable Energy Lab.(NREL), Golden, CO, Tech. Rep., 2013.

[62] R. Hutchinson, "Temperature effects on sealed lead acid batteries and charging techniques to prolong cycle life." Sandia National Laboratories, Tech. Rep., 2004.

[63] G. Albright, J. Edie, and S. Al-Hallaj, "A comparison of lead acid to lithium-ion in stationary storage applications," *Published by AllCell Technologies LLC, 2012*, 2012.

[64] F. Leng, C. M. Tan, and M. Pecht, "Effect of temperature on the aging rate of li ion battery operating above room temperature," *Scientific Reports*, vol. 5, p. 12967, 2015.

[65] Z. Song, H. Hofmann, J. Li, J. Hou, X. Zhang, and M. Ouyang, "The optimization of a hybrid energy storage system at subzero temperatures: Energy management strategy design and battery heating requirement analysis," *Applied Energy*, vol. 159, pp. 576–588, 2015.

[66] W. Yang, F. Zhou, H. Zhou, and Y. Liu, "Thermal performance of axial air cooling system with bionic surface structure for cylindrical lithium-ion battery module," *International Journal of Heat and Mass Transfer*, vol. 161, p. 120307, 2020.

[67] S. S. Katoch and M. Eswaramoorthy, "A detailed review on electric vehicles battery thermal management system," in *IOP Conference Series: Materials Science and Engineering*, vol. 912, no. 4. IOP Publishing, 2020, p. 042005.

[68] J. Li and Z. Zhu, "Battery thermal management systems of electric vehicles," Master's thesis, Chalmers University of Technology, 2014.

[69] Z. Qu, Z. Jiang, and Q. Wang, "Experimental study on pulse self–heating of lithium–ion battery at low temperature," *International Journal of Heat and Mass Transfer*, vol. 135, pp. 696–705, 2019.

[70] D. Shin, M. Poncino, and E. Macii, "Thermal management of batteries using supercapacitor hybrid architecture with idle period insertion strategy," *IEEE Transactions on Very Large Scale Integration (VLSI) Systems*, vol. 26, no. 6, pp. 1159–1170, 2018.

[71] R. de Castro and R. E. Araujo, "Model predictive power allocation for hybrid battery balancing systems," in *2019 IEEE Vehicle Power and Propulsion Conference (VPPC)*. IEEE, Hanoi, Vietnam, Sep. 22-25, 2019, pp. 1–5.

[72] Z. Huang, Y. Le, H. Liao, Y. Zhou, Y. Wu, H. Li, S. Li, X. Lu, and J. Peng, "A temperature-suppression power allocation strategy for hybrid energy management of evs," in *2019 IEEE Energy Conversion Congress and Exposition (ECCE)*. IEEE, Baltimore, MD, Sep. 29 – Oct. 03, 2019, pp. 3542–3547.

[73] L. W. Chong, Y. W. Wong, R. K. Rajkumar, and D. Isa, "An optimal control strategy for standalone pv system with battery-supercapacitor hybrid energy storage system," *Journal of Power Sources*, vol. 331, pp. 553–565, 2016.

[74] T. Zhu, R. Lot, R. G. Wills, and X. Yan, "Sizing a battery-supercapacitor energy storage system with battery degradation consideration for high-performance electric vehicles," *Energy*, vol. 208, p. 118336, 2020.

[75] J. Li, H. He, Z. Wei, and X. Zhang, "Hierarchical sizing and power distribution strategy for hybrid energy storage system," *Automotive Innovation*, vol. 4, no. 4, pp. 440–447, 2021.

[76] M.-K. Baek, J.-H. Roh, J.-B. Park, and W.-C. Jeong, "Optimal sizing of battery/supercapacitor hybrid energy storage systems for frequency regulation," *Journal of Electrical Engineering & Technology*, vol. 17, no. 1, pp. 111–120, 2022.

[77] L. Wang, M. Li, Y. Wang, and Z. Chen, "Energy management strategy and optimal sizing

for hybrid energy storage systems using an evolutionary algorithm," *IEEE Transactions on Intelligent Transportation Systems*, vol. 23, no. 9, pp. 14 283–14 293, 2021.

[78] G. M. Masters, *Renewable and Efficient Electric Power Systems*. John Wiley & Sons, Hoboken, NJ, 2013.

[79] M. Brooks, S. du Clou, J. van Niekerk, P. Gauche, C. Leonard, M. Mouzouris, A. Meyer, N. van der Westhuizen, E. van Dyk, and F. Vorster, "Sauran: A new resource for solar radiometric data in southern africa," *Journal of Energy in Southern Africa*, vol. 26, pp. 2–10, 2015.

[80] Southern African Universities Radiometric Network, "University of Pretoria - Hatfield Campus metering station [Online]," Available: http://sauran.net/ShowStation.aspx?station=5, Accessed: Feb. 06, 2017.

[81] Current Automation, "Sealed and vented lead-acid batteries [Online]," Available: http://www.rectifier.co.za/Catalogue/hoppecke.pdf, Accessed: Apr. 01, 2017.

[82] Maxwell ® Technologies, "All Ultracapacitor Documents [Online]," Available: http://www.maxwell.com/products/ultracapacitors/downloads, Accessed: Jan. 15, 2020.

[83] M. Morari and J. H. Lee, "Model predictive control: past, present and future," *Computers & Chemical Engineering*, vol. 23, no. 4-5, pp. 667–682, 1999.

[84] T. J. Ross, *Fuzzy Logic with Engineering Applications*, 4th ed. John Wiley & Sons, Ltd, Southern Gate, Chichester, West Sussex, United Kingdom, 2017.

[85] O. Cordón, F. Herrera, F. Hoffmann, and L. Magdalena, *Genetic Fuzzy Systems*. World Scientific Publishing Co. Pte. Ltd, London, United Kingdom, 2001.

[86] MathWorks ®, *Fuzzy logic toolbox™: User's guide*, 2019.

[87] P. Sanchis, A. Ursæa, E. Gubía, and L. Marroyo, "Boost dc-ac inverter: a new control strategy," *IEEE Transactions on Power Electronics*, vol. 20, no. 2, pp. 343–353, 2005.

[88] MathWorks ®, *Global Optimization Toolbox: User's guide*, 2019.

[89] A. Majumdar, *Soft Computing in Textile Engineering*. Elsevier, Philadelphia, PA, 2010.

[90] A. Meyer-Baese and V. J. Schmid, *Pattern Recognition and Signal Analysis in Medical Imaging*. Elsevier, San Diego, CA, 2014.

[91] A. Lahyani, A. Sari, I. Lahbib, and P. Venet, "Optimal hybridization and amortized cost study of battery/supercapacitors system under pulsed loads," *Journal of Energy Storage*, vol. 6, pp. 222–231, 2016.

[92] Lygte-info, "Battery test for small batteries, comparator [Online]," Available: https://lygte-info.dk/review/batteries2012/CommonSmallcomparator.php, Accessed: Feb. 04, 2021.

[93] Maxwell ® Technologies, "Supercapacitor datasheet [Online]," Available: https://www.maxwell.com/products/ultracapacitors/downloads, Accessed: Feb. 04, 2021.

[94] D. A. Schoenwald, S. R. Ferreira, D. M. Rosewater, D. R. Conover, A. Crawford, J. Fuller, S. Gourisetti, and V. Viswanathan, "Protocol for uniformly measuring and expressing tyhe performance of energy storage systems." Sandia National Lab.(SNL-NM), Albuquerque, NM, Tech. Rep., 2016.

[95] J. Wang, P. Liu, J. Hicks-Garner, E. Sherman, S. Soukiazian, M. Verbrugge, H. Tataria, J. Musser, and P. Finamore, "Cycle-life model for graphite-lifepo4 cells," *Journal of Power Sources*, vol. 196, no. 8, pp. 3942–3948, 2011.

[96] E. Redondo-Iglesias, P. Venet, and S. Pelissier, "Eyring acceleration model for predicting calendar ageing of lithium-ion batteries," *Journal of Energy Storage*, vol. 13, pp. 176–183, 2017.

[97] C.-J. Chiang, J.-L. Yang, and W.-C. Cheng, "Temperature and state-of-charge estimation in ultracapacitors based on extended kalman filter," *Journal of Power Sources*, vol. 234, pp. 234–243, 2013.

[98] C. Zhang, K. Li, J. Deng, and S. Song, "Improved realtime state-of-charge estimation of $LiFePO_4$ battery based on a novel thermoelectric model," *IEEE Transactions on Industrial Electronics*, vol. 64, no. 1, pp. 654–663, 2016.

[99] L. Zhang, Z. Wang, X. Hu, F. Sun, and D. G. Dorrell, "A comparative study of equivalent circuit models of ultracapacitors for electric vehicles," *Journal of Power Sources*, vol. 274, pp. 899–906, 2015.

[100] D. Shin, S. W. Chung, E.-Y. Chung, and N. Chang, "Energy-optimal dynamic thermal management: Computation and cooling power co-optimization," *IEEE Transactions on Industrial Informatics*, vol. 6, no. 3, pp. 340–351, 2010.

[101] K. Wang, L. Li, H. Yin, T. Zhang, and W. Wan, "Thermal modelling analysis of spiral wound supercapacitor under constant-current cycling," *PloS one*, vol. 10, no. 10, p. e0138672, 2015.

[102] N. Tian, H. Fang, J. Chen, and Y. Wang, "Nonlinear double-capacitor model for rechargeable batteries: Modeling, identification, and validation," *IEEE Transactions on Control Systems Technology*, vol. 29, no. 1, pp. 370–384, 2020.

[103] E. Stuve, "Electrochemical reactor design and configurations," in *Encyclopedia of Applied Electrochemistry*. Springer, NY, 2014, pp. 568–578.

[104] D. Andre, M. Meiler, K. Steiner, C. Wimmer, T. Soczka-Guth, and D. Sauer, "Characterization of high-power lithium-ion batteries by electrochemical impedance spectroscopy. i. experimental investigation," *Journal of Power Sources*, vol. 196, no. 12, pp. 5334–5341, 2011.

[105] X. Zhang, W. Zhang, and G. Lei, "A review of li-ion battery equivalent circuit models," *Transactions on Electrical and Electronic Materials*, vol. 17, no. 6, pp. 311–316, 2016.

[106] M. Nikdel *et al.*, "Various battery models for various simulation studies and applications," *Renewable and Sustainable Energy Reviews*, vol. 32, pp. 477–485, 2014.

[107] J. Miller, P. J. McCleer, and M. Cohen, "Energy buffers," *White Paper Maxwell Technologies, San Diego, CA*, 2004.

[108] D. New, J. G. Kassakian, and J. Schindall, "Automotive applications of ultracapacitors," MIT Industry Consortium on Advanced Automotive Electrical Electronic Components and Systems, Consortium Project Report Winter, 2003.

[109] H. Wang, J. Li, X. Liu, J. Rao, Y. Fan, and X. Tan, "Online state of health estimation for lithium-ion batteries based on a dual self-attention multivariate time series prediction network," *Energy Reports*, vol. 8, pp. 8953–8964, 2022.

[110] M. Petit, E. Prada, and V. Sauvant-Moynot, "Development of an empirical aging model for li-ion batteries and application to assess the impact of vehicle-to-grid strategies on battery lifetime," *Applied Energy*, vol. 172, pp. 398–407, 2016.

[111] C. Guenther, B. Schott, W. Hennings, P. Waldowski, and M. A. Danzer, "Model-based investigation of electric vehicle battery aging by means of vehicle-to-grid scenario simulations," *Journal of Power Sources*, vol. 239, pp. 604–610, 2013.

[112] A. Lahyani, P. Venet, A. Guermazi, and A. Troudi, "Battery/supercapacitors combination in uninterruptible power supply (UPS)," *IEEE Transactions on Power Electronics*, vol. 28, no. 4, pp. 1509–1522, 2012.

[113] H. Wang and F. Blaabjerg, "Reliability of capacitors for DC-link applications in power electronic converters – An overview," *IEEE Transactions on Industry Applications*, vol. 50, no. 5, pp. 3569–3578, 2014.

[114] P. I. Prodanov and D. D. Dankov, "Applying aging models for reliability assessment of supercapacitors," in *2020 XI National Conference with International Participation (ELECTRONICA)*. IEEE, Sofia, Bulgaria, May 14–15, 2020, pp. 1–4.

[115] W. J. Fabrycky and B. S. Blanchard, *Life-cycle cost and economic analysis*. Prentice Hall Englewood Cliffs, NJ, 1991, vol. 135383234.

[116] F. Torabi and P. Ahmadi, *Simulation of Battery Systems: Fundamentals and Applications*. Academic Press, Cambridge, MA, 2019.

[117] Trading Economics, "South africa inflation rate [online]," Available: https://tradingeconomics.com/south-africa/inflation-cpi, Accessed: Aug. 17, 2022.

[118] ——, "Deposit interest rate in south africa [online]," Available: https://tradingeconomics.com/south-africa/deposit-interest-rate, Accessed: Aug. 17, 2022.

[119] Takealot Online (Pty) Ltd, "BV - Samsung 29E 18650 2850mAh 2.75A Battery (For Battery Packs & Torches) [Online]," Available: https://www.takealot.com/, Accessed: Aug. 17, 2022.

[120] Digi-Key Electronics, "BMOD0002 P005 B02 [Online]," Available: https://www.digikey.co.za/, Accessed: Aug. 17, 2022.

[121] K. Kim, J. An, K. Park, G. Roh, and K. Chun, "Analysis of a supercapacitor/battery hybrid power system for a bulk carrier," *Applied Sciences*, vol. 9, no. 8, p. 1547, 2019.

[122] Eskom Holdings SOC Ltd, "Tariffs & Charges Booklet 2022/2023 [Online]," Available: https://www.eskom.co.za/distribution/wp-content/uploads/2022/05/4756-ESKOM-Tariff-Booklet-2022-Final-Rev.pdf, Accessed: Aug. 17, 2022.

[123] ——, "Tariff history [Online]," Available: https://www.eskom.co.za/distribution/tariffs-and-charges/tariff-history/, Accessed: Aug. 17, 2022.

[124] J. Engels, B. Claessens, and G. Deconinck, "Techno-economic analysis and optimal control of battery storage for frequency control services, applied to the german market," *Applied Energy*, vol. 242, pp. 1036–1049, 2019.

ADDENDUM A BLOCK DIAGRAM SIMULATION MODEL OF THE BATTERY-SUPERCAPACITOR HESS

The power and control layers of the model implemented Matlab/Simulink block are shown in Figure A.1 and Figure A.2 respectively.

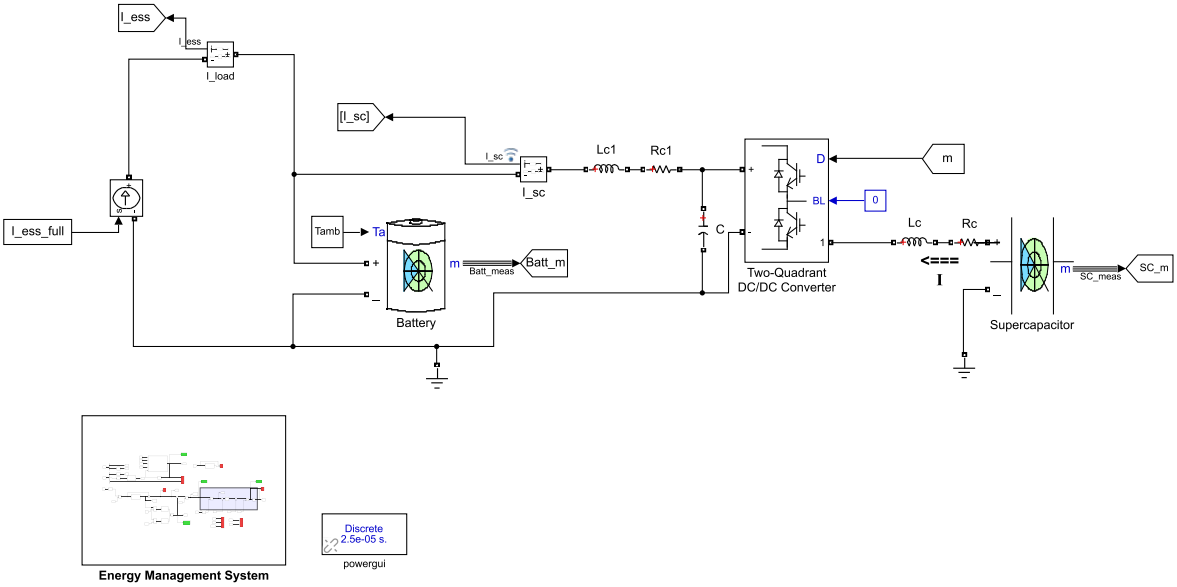

Figure A.1. Power layer of the block diagram in Simulink

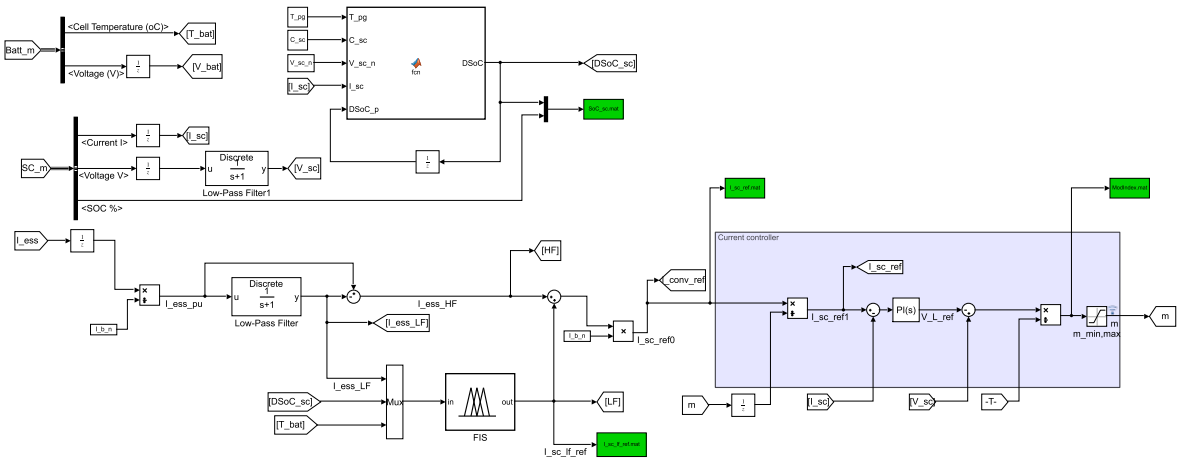

Figure A.2. Energy Management System (control layer) in Simulink